

# Multifault Detection, Diagnosis, and Prognosis for Rotating Machinery

Lead Guest Editor: Zhixiong Li

Guest Editors: Chao Hu, Adam Glowacz, Tonghai Wu, and Grzegorz M. Królczyk





---

# **Multifault Detection, Diagnosis, and Prognosis for Rotating Machinery**

International Journal of Rotating Machinery

---

## **Multifault Detection, Diagnosis, and Prognosis for Rotating Machinery**

Lead Guest Editor: Zhixiong Li

Guest Editors: Chao Hu, Adam Glowacz, Tonghai Wu,  
and Grzegorz M. Królczyk



---

Copyright © 2018 Hindawi. All rights reserved.

This is a special issue published in “International Journal of Rotating Machinery.” All articles are open access articles distributed under the Creative Commons Attribution License, which permits unrestricted use, distribution, and reproduction in any medium, provided the original work is properly cited.

---

## Editorial Board

H. Joon Ahn, Republic of Korea  
Ryoichi Samuel Amano, USA  
Sourabh V. Apte, USA  
Farid Bakir, France  
Hans Joerg Bauer, Germany  
Gerard Bois, France  
Christopher Earls Brennen, USA  
Alessandro Corsini, Italy  
Luis Gato, Portugal

Awatef Hamed, USA  
Jechin Han, USA  
Hooshang Heshmat, USA  
Dimitrios T. Hountalas, Greece  
Norihiko Iki, Japan  
Mohammad Tariq Iqbal, Canada  
Funazaki Ken-ichi, Japan  
Akira Murata, Japan  
M. Razi Nalim, USA

Eddie Ng Yin Kwee, Singapore  
Yutaka Ohta, Japan  
Ion Paraschivoiu, Canada  
Paolo Pennacchi, Italy  
Sergio Preidikman, USA  
Meinhard T. Schobeiri, USA  
Terrence W. Simon, USA  
Seung Jin Song, Republic of Korea

# Contents

---

## **Multifault Detection, Diagnosis, and Prognosis for Rotating Machinery**

Zhixiong Li  and Grzegorz M. Królczyk 

Editorial (1 page), Article ID 5238595, Volume 2018 (2018)

## **Rolling Element Bearing Performance Degradation Assessment Using Variational Mode Decomposition and Gath-Geva Clustering Time Series Segmentation**

Yaolong Li, Hongru Li, Bing Wang, and Hongqiang Gu

Research Article (12 pages), Article ID 2598169, Volume 2017 (2018)

## **Study on Frequency Characteristics of Rotor Systems for Fault Detection Using Variational Mode Decomposition**

Kai Chen, Xin-Cong Zhou, Jun-Qiang Fang, and Li Qin

Research Article (11 pages), Article ID 7218646, Volume 2017 (2018)

## **Fault Feature Extraction and Diagnosis of Gearbox Based on EEMD and Deep Briefs Network**

Kai Chen, Xin-Cong Zhou, Jun-Qiang Fang, Peng-fei Zheng, and Jun Wang

Research Article (10 pages), Article ID 9602650, Volume 2017 (2018)

## **Stator and Rotor Faults Diagnosis of Squirrel Cage Motor Based on Fundamental Component Extraction Method**

Guoqing An and Hongru Li

Research Article (8 pages), Article ID 1576381, Volume 2017 (2018)

## **Fault Identification of Rotor System Based on Classifying Time-Frequency Image Feature Tensor**

Hui Li, Xiaofeng Liu, and Lin Bo

Research Article (12 pages), Article ID 6542348, Volume 2017 (2018)

## Editorial

# Multifault Detection, Diagnosis, and Prognosis for Rotating Machinery

Zhixiong Li <sup>1</sup> and Grzegorz M. Królczyk <sup>2</sup>

<sup>1</sup>University of Wollongong, Wollongong, NSW, Australia

<sup>2</sup>Politechnika Opolska, Opole, Poland

Correspondence should be addressed to Zhixiong Li; zhixiong.li@ieee.org

Received 21 March 2018; Accepted 21 March 2018; Published 1 August 2018

Copyright © 2018 Zhixiong Li and Grzegorz M. Królczyk. This is an open access article distributed under the Creative Commons Attribution License, which permits unrestricted use, distribution, and reproduction in any medium, provided the original work is properly cited.

As professionals working in the field of condition monitoring and fault diagnosis, we know that reliable recognition of fault type and assessment of fault severity are essential for decision making in condition-based maintenance of rotating machinery. In engineering practice, the mechanical systems of rotating machinery are often subject to concurrent faults on the same component or different components, which make the examination of both the fault types and severities more challenging. Popular intelligent algorithms such as artificial neural networks (ANNs) are proven effective in identifying different fault patterns while “physical meanings” of the identification process are often missed due to *black-box* of intelligent algorithms. Alternatives such as multimodal decomposition approaches enable decoupling the hybrid faults into submodes. Each submode describes a single fault in the hybrid faults. As a result, the “physical meanings” of the identification process can be revealed using the multimodal decomposition approaches. This special issue looks at latest multimodal decomposition approaches for multifault detection, diagnosis, and prognosis on rotating machinery.

The article by K. Chen et al. (Wuhan University of Technology, China) is a good place to begin this special issue as the authors introduced the variational mode decomposition (VMD) as the multimodal decomposition approach to detect multiple faults in rotor systems. The decomposed vibration signals using VMD can be used to extract effective features for multifault detection. The authors evaluated the performance of the proposed method using experimental data.

In another article, G. An and H. Li from Mechanical Engineering College in China developed a multimodal

decomposition approach based on fundamental component extraction (FCE) algorithm for multifault detection of rotor systems. The failures in stator and rotor can be effectively identified by the proposed FCE method.

In another two articles, H. Li et al. (State Key Laboratory of Mechanical Transmission, China) presented an image tensor extraction method for rotor fault diagnosis and K. Chen et al. (Wuhan University of Technology, China) introduced an integrated approach of ensemble empirical mode decomposition and deep briefs network to diagnose gear multiple faults. The authors conducted experimental testing to evaluate the performance of the proposed approaches.

Y. Li et al. is a good place to conclude this special issue as the authors proposed a new method based on variational mode decomposition and Gath-Geva clustering time series segmentation to extract the degradative feature of rolling element bearings and predict the bearing failures. The effectiveness of the proposed bearing degradation prediction method was verified by two case studies.

## Acknowledgments

I would like to thank the authors for submitting their work to this special issue. I would also like to express my gratitude to the reviewers and the guest editors for their help and support with producing this issue.

Zhixiong Li  
Grzegorz M. Królczyk

## Research Article

# Rolling Element Bearing Performance Degradation Assessment Using Variational Mode Decomposition and Gath-Geva Clustering Time Series Segmentation

Yaolong Li,<sup>1</sup> Hongru Li,<sup>1</sup> Bing Wang,<sup>2</sup> and Hongqiang Gu<sup>1</sup>

<sup>1</sup>Shijiazhuang Mechanical Engineering College, Shijiazhuang 050003, China

<sup>2</sup>Shanghai Maritime University, Shanghai 200135, China

Correspondence should be addressed to Hongru Li; [lihr168@sohu.com](mailto:lihr168@sohu.com)

Received 28 April 2017; Revised 23 May 2017; Accepted 5 September 2017; Published 12 October 2017

Academic Editor: Grzegorz M. Krolczyk

Copyright © 2017 Yaolong Li et al. This is an open access article distributed under the Creative Commons Attribution License, which permits unrestricted use, distribution, and reproduction in any medium, provided the original work is properly cited.

By focusing on the issue of rolling element bearing (REB) performance degradation assessment (PDA), a solution based on variational mode decomposition (VMD) and Gath-Geva clustering time series segmentation (GGCTSS) has been proposed. VMD is a new decomposition method. Since it is different from the recursive decomposition method, for example, empirical mode decomposition (EMD), local mean decomposition (LMD), and local characteristic-scale decomposition (LCD), VMD needs a priori parameters. In this paper, we will propose a method to optimize the parameters in VMD, namely, the number of decomposition modes and moderate bandwidth constraint, based on genetic algorithm. Executing VMD with the acquired parameters, the BLIMFs are obtained. By taking the envelope of the BLIMFs, the sensitive BLIMFs are selected. And then we take the amplitude of the defect frequency (ADF) as a degradative feature. To get the performance degradation assessment, we are going to use the method called Gath-Geva clustering time series segmentation. Afterwards, the method is carried out by two pieces of run-to-failure data. The results indicate that the extracted feature could depict the process of degradation precisely.

## 1. Introduction

Rolling element bearings (REBs) are critical components of “rotor-bearing” system in rotating machinery. Since the cruel working condition, the REBs are vulnerable. So it is important to monitor their condition to avoid catastrophic accident in modern industry. There are many ways to monitor bearings, such as vibration [1], acoustic emission [2], oil-debris [3], and ultrasound [4]. Among them, the method based on vibration signal analysis is extensively used for a bearing.

Recently, the prediction of the residual (or remaining) useful life (RUL) is a hotspot issue. To get a better bearing fault prediction result, the so-called performance degradation assessment (PDA) is a premise. The PDA contains two important aspects. One is to extract proper features that can reflect the process of degradation. The other one is to use a method to assess the REB's performance. Feature

extraction is the fundamental of PDA. The feature must reveal the real performance of the REB and be sensitive to the degradation. The types of features are usually classified into three categories, time domain features, frequency domain features, and time-frequency domain features. The time-frequency domain features are always based on time-frequency analysis, combined with the concept of spectrum, entropy, and complexity, for example, the Rényi entropy [5], the permutation entropy [6], and the general mathematical morphology particle [7]. In general, mechanical equipment undergoes a complete degradation from normal stage to failure. With the increasing of the running time and deepening of degradation, the amplitude of defect frequency (ADF) is raising therewith. So the ADF can reflect the degradation of REB directly.

To get the ADF, the first thing is to locate the defect frequency. In extraction of ADF, the common method is

to use EMD and select appropriate intrinsic mode function (IMF) components, taking the envelope spectrum, and finally get the ADF [8]. However, EMD remains an exclusively empirical algorithm, and it lacks a solid mathematical foundation. Despite numerous attempts to improve its performance, EMD is still of low efficiency and has endpoint effect and mode mixing problems. In 2014, Dragomiretskiy and Zosso [9] proposed a method called variational mode decomposition (VMD) as an alternative to EMD, which can adaptively decompose a multicomponent signal into a number of quasiorthogonal IMFs. It has been verified that VMD outperforms EMD with regard to tone detection and separation as well as noise robustness [10]. It has a good performance and high operation efficiency. Particularly, it has solid foundation for a mathematical theory. Now the method has been applied to the abnormal ECG signal detection [11], the stock market forecasting [12], wind power prediction [13], power quality classification [14], and so on.

However, the parameters of VMD are selected by experience. Jun Zhu presented a method to optimize the parameters based on the kurtosis index through artificial fish swarm algorithm [15]. Tang and Wang used Shannon entropy as an index to optimize parameters by panicle swarm algorithm [16]. In this paper, we proposed a method to optimize the parameters based on BLIMFs themselves using genetic algorithm. As to PDA, Pan et al. [17] proposed a bearing degradation assessment method based on lifting wavelet packet decomposition and fuzzy C-means clustering. Wang et al. [18] proposed a method for PDA based on mathematical morphology fractal dimension and fuzzy C-means clustering. However, when using clustering, they only considered the distance factor, and no time parameter was recommended. The clusters should be contiguous in time. From this point of view, after extraction of ADF from the raw signals, the assessment of bearing performance is carried out by GGCTSS.

The remainder of this paper is organized as follows. In Section 1, the theory of VMD is briefly introduced. The optimization of the parameters is proposed in Section 2. In Section 3, by carrying out two run-to-failure data, we have extracted the ADF and used GGCTSS for PDA. Our conclusions are presented in Section 4.

## 2. VMD and Its Parameters

**2.1. Variational Mode Decomposition.** VMD can nonrecursively decompose a real-valued multicomponent signal into a discrete number of quasiorthogonal band-limited subsignals  $u_k$  with specific sparsity properties in the spectral domain. Each mode is compacted around a center pulsation  $\omega_k$ . For convenience, let us call these modes obtained by VMD as band-limited IMFs (BLIMFs). The VMD technique is essentially written as a constrained variational problem in [9]

$$\begin{aligned} \min \quad & \left\{ \sum_{k=1}^K \left\| \partial_t \left[ \left( \sigma(t) + \frac{j}{\pi t} \right) * u_k(t) \right] e^{-j\omega_k t} \right\|_2^2 \right\} \\ \text{Subject to} \quad & \sum_{k=1}^K u_k = f, \end{aligned} \quad (1)$$

where  $\{u_k\} = \{u_1, \dots, u_k\}$  and  $\{\omega_k\} = \{\omega_1, \dots, \omega_k\}$  are the decomposed BLIMFs for the set of all  $K$  modes and their estimated center frequencies, respectively. The VMD process can be briefly described as follows; for further details, refer to [9].

**2.2. Parameters Involved in VMD.** There are six parameters for VMD, where  $K$  represents the numbers of decomposition modes and  $\alpha$  represents moderate bandwidth constraint; they are two parameters that significant influence on the decomposition results. In general, the parameter  $\tau$  is set up to zero, which means that the Lagrangian multiplier is effectively shut off. The parameter *init* is set to be one, which suggests that center frequencies of all the modes are initialized in the uniform distribution. The parameter *DC* is set to zero, for no DC part imposed. And the parameter *tol* for tolerance is set as default value  $1e - 6$ .

**2.3. The Optimization of VMD Parameters.** Figure 1 shows the impact of the parameter  $\alpha$ . It can be seen that the parameter  $\alpha$  seems to have an inverse ratio of the decomposition modes' bandwidth. In Figure 1(a), there is no high frequency mode. It seems to be a better one with  $\alpha = 200$  in Figure 1(b). Because the parameter *init* is set to be one, the bandwidth of each mode is almost the same. To optimize the parameter  $K$  and  $\alpha$ , A criterion must be raised. We have proposed a criterion  $\eta$  in formula (2).

$$\eta = \frac{\sum_i^K |l - l_0|}{f_{\max}}, \quad (2)$$

where  $l_0$  is the supposed frequency band of each mode and  $l$  is the actual frequency band of each mode. For example, in Figure 1(a),  $l_0$  is 0–2000 Hz, 2000–4000 Hz, 4000–6000 Hz, 6000–8000 Hz, and 8000–10000 Hz, and the actual frequency bands of BLIMFs are 0–1396 Hz, 1426–2549 Hz, 2900–4014 Hz, 3686–4620 Hz, and 3926–5376 Hz with the  $y$ -axis threshold 0.001.  $\eta$  is calculated to 0.4021, since  $K$  must be set as integer, but not for parameter  $\alpha$ . We can find the optimized  $\alpha$  using genetic algorithm of each mode. The settings of genetic algorithm are using default in MATLAB and finally get the best  $K$  and  $\alpha$ . The minimum of  $K$  is 2. EMD can be used to find the maximum value of  $K$ . There are 10 IMFs of the signal decomposed by EMD, so the maximum of  $K$  is set up to 10.

## 3. The Experimental Verification

**3.1. Experiment Illustration.** The run-to-failure REB' test data are derived from IMS center [19]. The bearing test rig hosted four test bearings on a shaft. The shaft was driven by an AC motor. The rotation speed was kept constant at 2000 rpm. A radial load of 6000 lbs was added to the shaft and bearing by a spring mechanism. All the bearings are force oil-lubricated. Four Rexnord ZA-2115 double row bearings were installed on the shaft as shown in Figure 2. The bearings had 16 rollers in each row, a pitch diameter of 2.815 inch, roller diameter of 0.331 inch, and a tapered contact angle of 15.17°. A high sensitivity accelerometer was installed on each bearing's

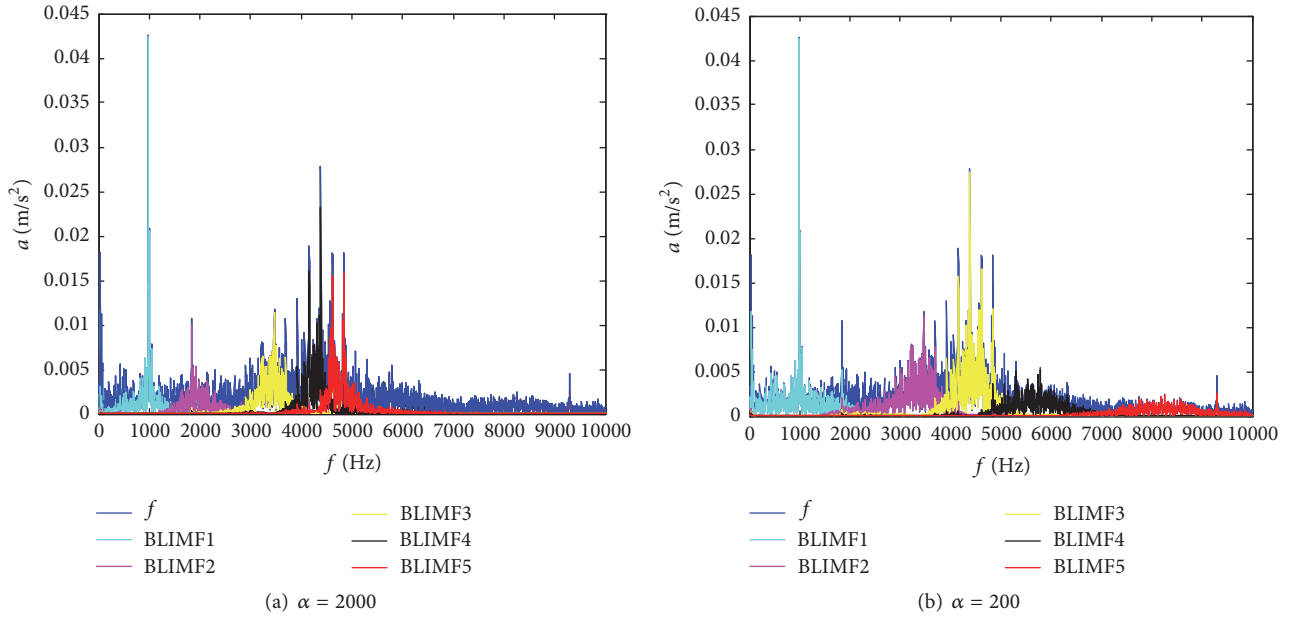


FIGURE 1: The impact of the parameter  $\alpha$ .

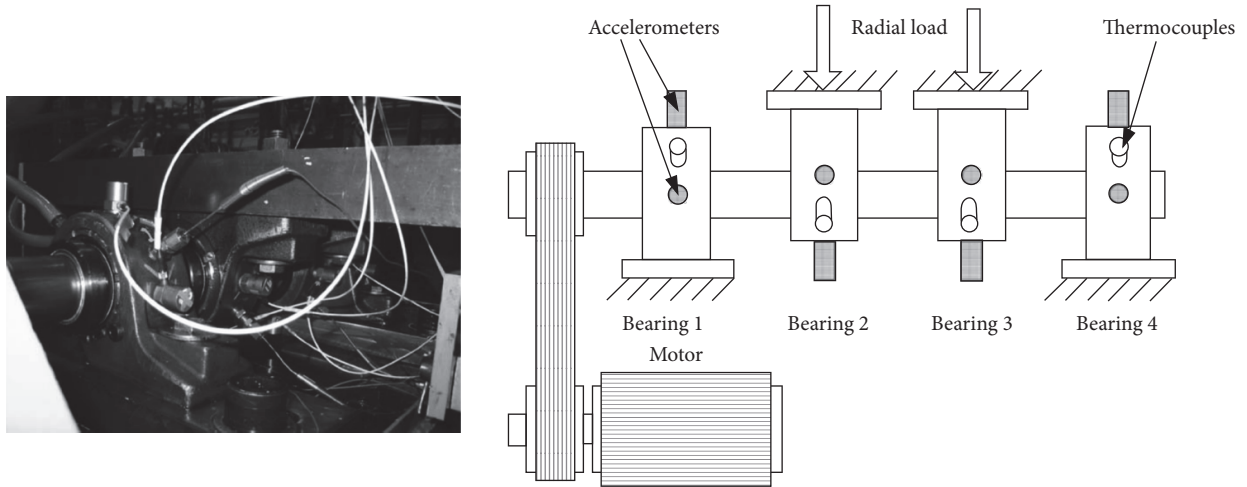


FIGURE 2: Bearing test rig.

housing. The data sampling rate was 20 kHz and the data length was 20480 points. The sampling interval was ten minutes. We use the Bearing1.1's data of set number 2 which exhibits outer race defect as shown in Figure 3. The number of the data files is 982 (the original files number is 984, for the last 2 files it is vague and distinctive).

For the theoretical value of outer race defect frequency, we can use the formula as follows and then have the theoretical frequency of 236.4 Hz:

$$f_{op} = \frac{Z}{2} \left( 1 - \frac{d}{D} \cos \theta \right) f_r. \quad (3)$$

From Figure 4, we could not find the defect frequency of #600 (where # means the number of files). The range of  $\alpha$  is set from 1000 to 10000. Now, by using genetic algorithm,

the optimized parameter  $\alpha$  of  $K$  mode decomposition is presented in Table 1.

From Table 1, the optimized parameter  $K$  is for 4 and  $\alpha$  for 9534. The decomposition result by optimized parameters is shown in Figure 5.

As shown in the figure, the signal is decomposed into 4 BLIMFs. The spectrum is in accordance with the order from low to high; that is, VMD has the role of band pass filtering. The BLIMFs do not show the phenomenon of mode mixing. The contrast group EMD, as shown in Figure 6, is decomposed for 11 IMFs. As we can see, EMD has a characteristic that, with the order from low to high, IMF is narrowed approximate dichotomy, and each IMF has low frequency components, and LCD and LMD have similar characteristics. At the same time, the computing time of



FIGURE 3: Outer race defect of set number 2.

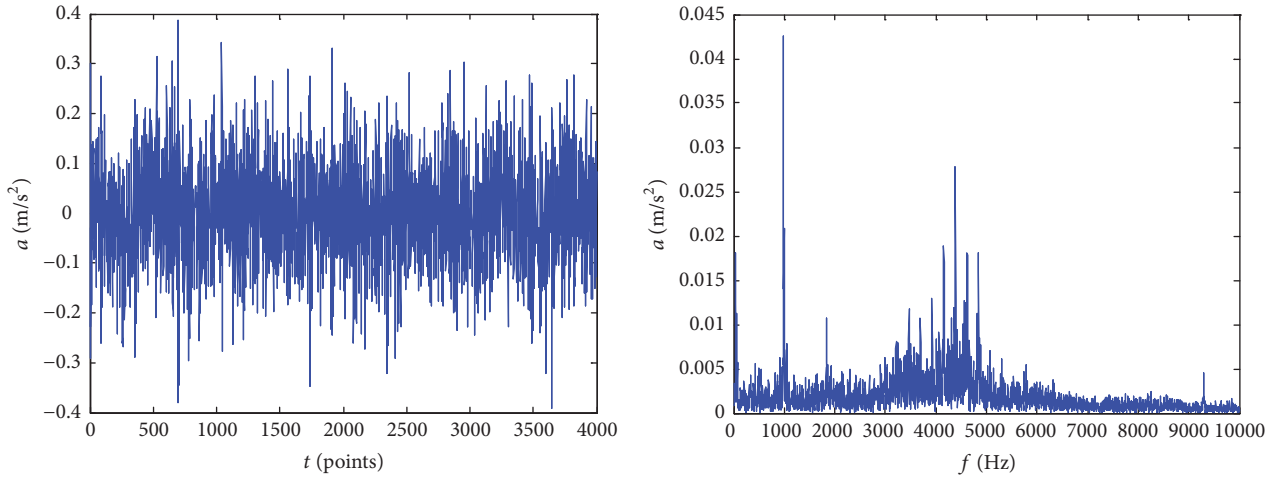


FIGURE 4: The vibration wave and frequency spectrum of #600.

TABLE 1: The optimized parameter  $\alpha$  of each  $K$  mode decomposition.

$K$	The optimized parameter $\alpha$	Criterion $\eta$
2	1382	0.9502
3	1044	1.1704
4	9534	0.9302
5	9651	1.2129
6	9736	1.5024
7	1423	1.5122
8	2321	1.6714
9	1537	2.2026
10	9286	1.5204

VMD is far less than EMD, because there is no recursive iteration process of VMD.

The signal of #600 is decomposed into 4 BLIMFs by optimized VMD and the envelope spectrum is shown in Figure 7.

It can be seen that the BLIMF2 and BLIMF3 have the peak of 230.7 Hz, which is close to the theoretical value 236.4 Hz. So the BLIMF2 and BLIMF3 are the right mode which have the defect frequency. By extracting the amplitude

of all BLIMF2 and BLIMF3's defect frequency, an ADF of all REB's data is shown in Figure 8.

It can be seen from Figure 8 that, before #520, the amplitude is close to zero. That indicates that there is no obvious defect before #520. From #520 to #700, the ADF increases in a linear way. Guess that spalling is formed and become larger, and the REB is in the slight fault stage. About #700, there is a sudden change, and we speculate that it is caused by a bulge or a crack. From #700 to #850, the amplitude decreases and rises again. The fluctuating trend can be explained by the nature of the propagating process of the damage, when the spalling formed and later smoothed by the continuous rolling contact. As the damage spread over a broader area, the vibration level raises again. This is called "healing" phenomenon and has been stated in [1, 20, 21]. From #850 to the end #982, the condition of REB is becoming fierce. The "healing" phenomenon expands, and the variances enlarge. Overall, the ADF is increasing. If the ADF is segmented in 4 parts, it is rational for #1 to #520 for normal stage, #521 to #699 for slight fault stage, #700 to #850 for serious stage, and #851 to end for fault stage.

3.2. The PDA Using GGCTSS. As mentioned before, fuzzy C-means clustering has its drawback for PDA. As shown in

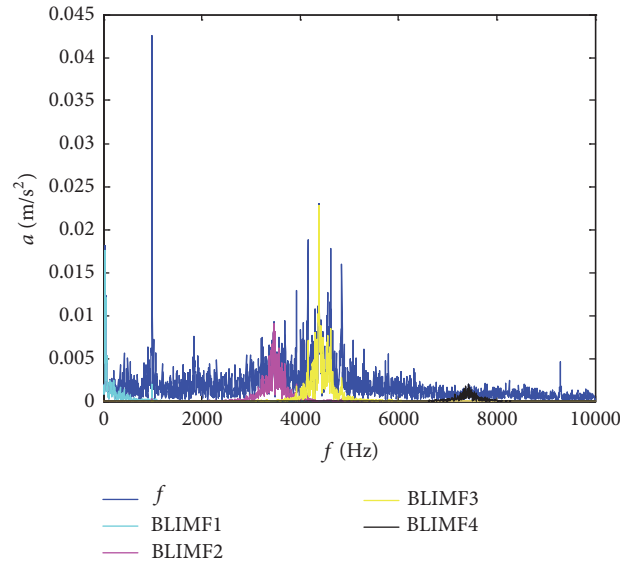


FIGURE 5: The BLIMFs and frequency spectrum of #600.

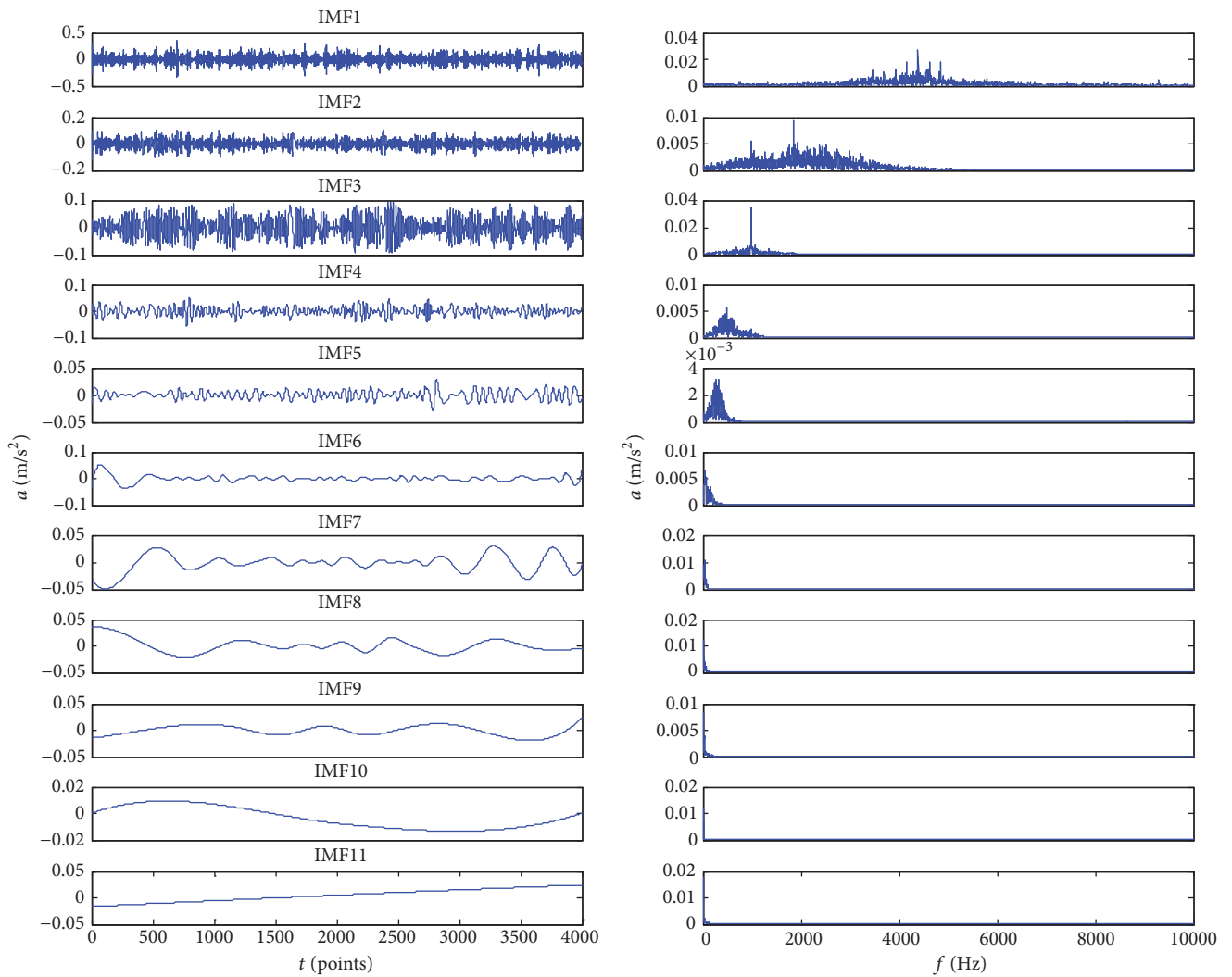


FIGURE 6: The IMFs and frequency spectrum of #600.

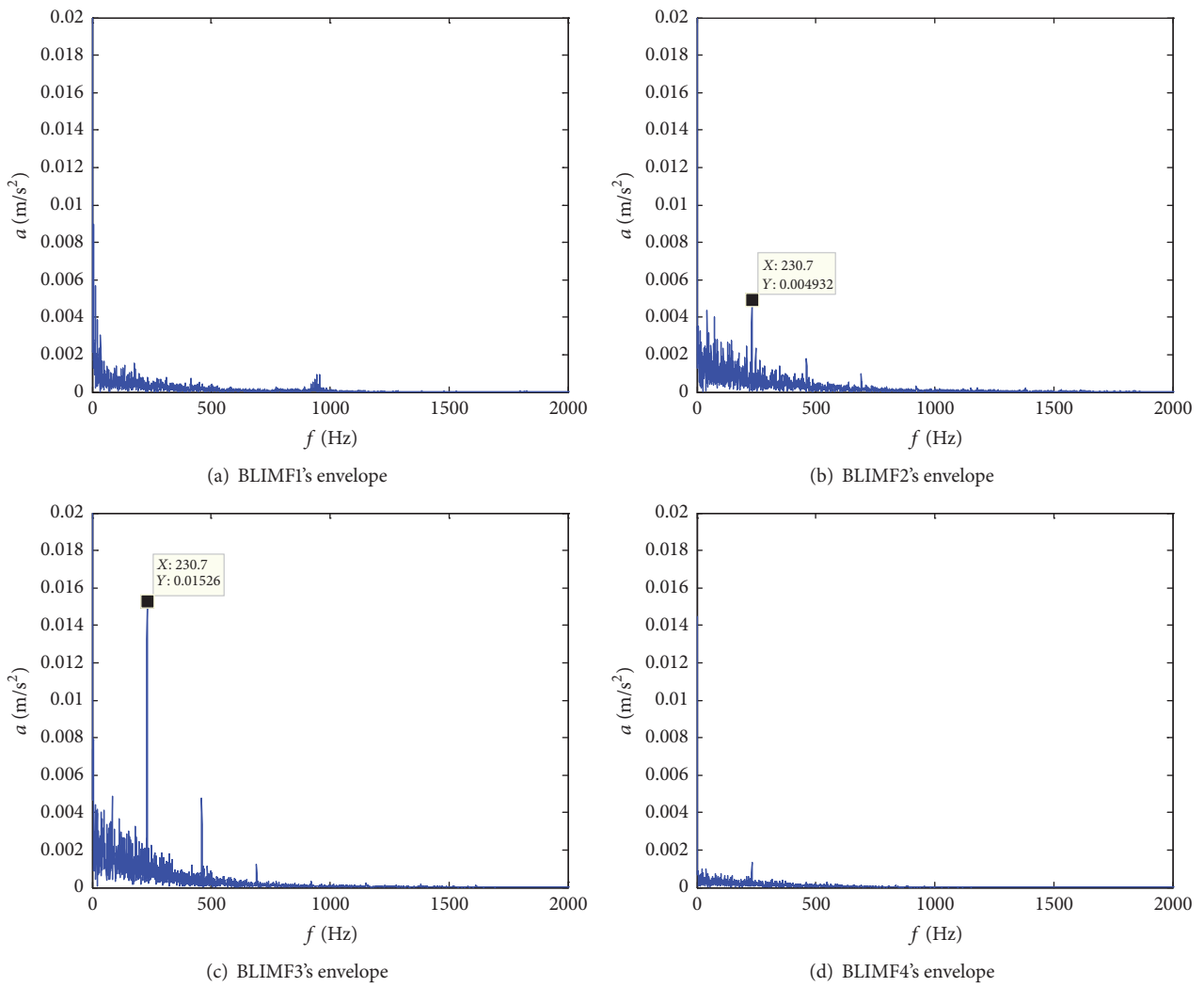


FIGURE 7: The envelope spectrum of BLIMF1 to BLIMF4 of #600.

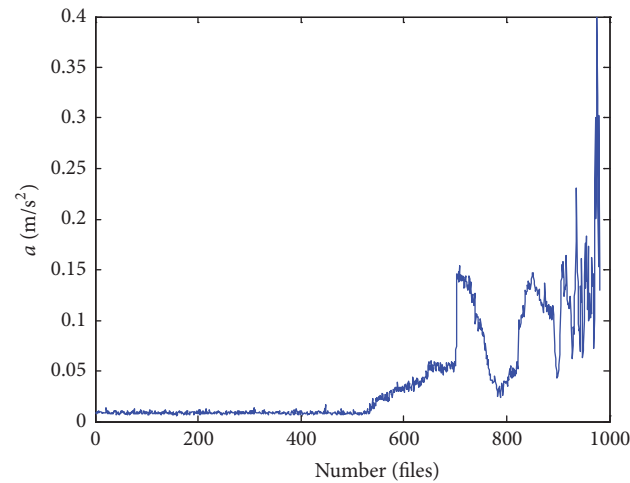


FIGURE 8: The ADF of the data.

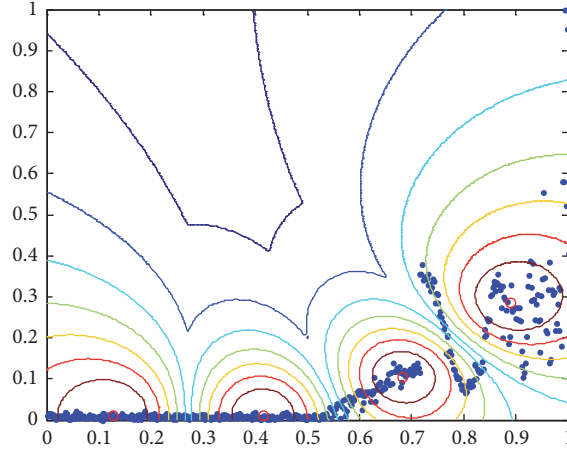


FIGURE 9: The clustering result of the ADF proposed by fuzzy C-means.

Figure 9. The four clustering results of the ADF are conducted by fuzzy C-means (the data have been normalized).

According to the clustering order from left to right, the first two clustering centers are in the normal state of the REB. The third center is in the slight fault state. The fourth one is almost close to the boundary of severely fault and failure. The result is unacceptable. References [17, 18] both used fuzzy C-means to realize PDA, Where owing to the degradation features which they have proposed is roughly monotonic, the cluster results of fuzzy C-means are basically distributed in time growth order. If the degradation features are inconspicuous or existing oscillation, we could not get a good clustering result. Therefore, it is necessary to import the concept of time series segmentation.

A sequence of  $N$  times observed data,  $T = \{x_1, x_2, \dots, x_N\}$ , is called time series. Time series segmentation is to find a partitioning of  $T$  into  $c$  segments that are internally homogeneous. After a segmentation,  $T = \{x_1, x_2, \dots, x_N\}$  can be partitioned into  $\{S_N^1, S_N^2, \dots, S_N^c\}$ , where  $S_N^1 = S(1, t_1)$ ,  $S_N^n = S(t_{n-1} + 1, t_n)$ , and  $0 < t_1 < \dots < t_{n-1} < \dots < t_c = N$ . The times  $t_1, \dots, t_{n-1}, \dots, t_c$  are called segment boundaries or breaks, and the number  $c$  is called the order of the segmentation. This segmentation is a crisp one. A time series segmentation problem can convert into an optimization. Himberg et al. [22] have defined the cost function. Under the definition, Kehagias et al. [23] proposed a dynamic programming (DP) segmentation procedure and Gedikli et al. [24] improved it with modified dynamic programming (mDP). Both methods are based on minimization of the summation of cost functions followed by distances between actual values and constant or linear fittings.

Expanding and improving the crisp bounds of the segmentation, Abonyi et al. [25] developed an algorithm for dividing time series into fuzzy segments, which considered time series segmentation as Gath-Geva clustering with time parameter as an additional variable. The GGCTSS used local probabilistic principal component analysis (PPCA) models to measure the homogeneity of the segments and fuzzy sets to

represent segments in time. The function to be optimized can be written as

$$J = \sum_{i=1}^c \sum_{k=1}^N (\mu_{i,k})^m D^2(z_k, \eta_i), \quad (4)$$

where the data point  $z_k = [t_k, x_k^T]^T$  can be effectively modeled as a mixture of multivariate Gaussian distribution and  $\mu_{i,k}$  stands for the  $i$ th segment membership of  $z_k$ . The term  $m$  is weighing exponent of fuzzy degree,  $m \in [1, \infty]$ . For general,  $m = 2$ . The procedure of the GGCTSS can be written as follows:

(1) Initial the order segmentation  $c$ , iteration number  $sl$ , and the threshold for compatible cluster merging (0.75 as default).

(2) Input the number of principal components  $q$  and make sure that the sum of the anterior  $q$  eigenvalues account for more than 98% accuracy of the sum of all eigenvalues.

(3) Finish the iteration and give the results of segmentation.

The results include the fuzzy segmentation of a time series,  $\beta_k(t_i)$ , which is defined as

$$\beta_k(t_i) = \frac{A_k(t_i)}{\sum_{k=1}^K A_k(t_i)} \in [0, 1], \quad (5)$$

where  $A_k(t_i)$  is Gaussian membership function given by

$$A_k(t_i) = \exp\left(-\frac{1}{2} \frac{(t_i - \mu_k)^2}{\sigma_k^2}\right). \quad (6)$$

See [22] for more details of the method.

The mDP algorithm is used to treat the ADF for the fourth-order segmentations, and the results are shown in Figure 10.

It can be seen that the segmentations by mDP algorithm are not good. So, we use GGCTSS for PDA. The process of life was divided into 4 segments. Set the iteration to be 100 times.

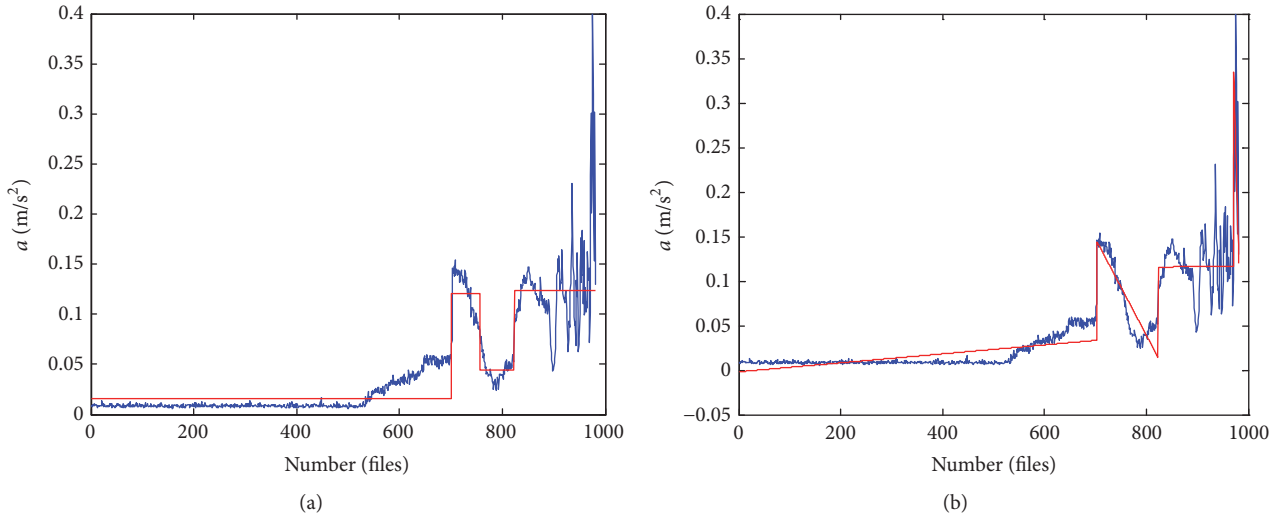


FIGURE 10: The optimal fourth-order segmentations of ADF by mDP algorithm. (a) Constant fitting and (b) linear fitting.

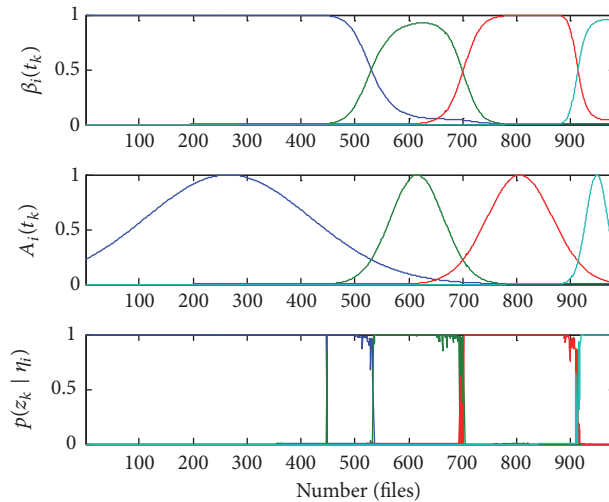


FIGURE 11: The result of the ADF based on GGCTSS.

It is about 70 iterations that the result is basically unchanged. Figure 11 shows the result.

It can be seen that the four segmentations are partitioned according to the order of time. The normal stage is from #0 to #522, the slight stage is from #522 to #700, the severe stage is from #700 to #900, and the failure stage is from #900 to #982. It is possible to show that GGCTSS can be a good one for PDA.

**3.3. Another Experiment Verification.** IEEE PHM 2012 Prognostic Challenge data is another REBs' data. Figure 12 shows the experiment rig, the PRONOSTIA platform, where the data included three different loads for 1800 rpm and 4000 N, 1650 rpm and 4200 N, and 1500 rpm and 5000 N. The sampling frequency was 25.6 kHz, and 2560 samples were recorded each 10 seconds. There were 6 pieces of run-to-failure data which were the learning sets, and 11 test bearings were truncated so that participants were supposed to

predict the remaining life (see Table 2) and thereby preformed RUL estimating. The learning set was quite small while the spread of the life duration of all bearings was very wide. Performing good estimates was thereby difficult and this made the challenge more exciting. More details can be seen in [26].

The data is difficult to analysis because we know nothing about the nature and the origin of the degradation: inner or outer races. We are going to use Bearing1.1's data and the characteristics of the tested bearing are shown in Table 3. And the characteristics' frequency of REB is 168.3 Hz for outer race, 221.7 Hz for inner race, 107.7 Hz for ball race, and 12.9 Hz for cage.

The numbers of Bearing1.1 are 2803, thus taking #2600 for analysis, since the REB is almost run to failure. Figure 13 shows the signal.

Now, by using genetic algorithm, we have the optimized  $K$  and  $\alpha$ , and  $K$  is for 3 and  $\alpha$  for 4032. The signal is

TABLE 2: Datasets of PHM 2012 Prognostic Challenge.

Datasets	Operating conditions		
	Conditions 1 (1800 rpm and 4000 N)	Conditions 1 (1650 rpm and 4200 N)	Conditions 1 (1500 rpm and 5000 N)
Learning set	Bearing1_1	Bearing2_1	Bearing3_1
	Bearing1_2	Bearing2_2	Bearing3_2
Test set	Bearing1_3	Bearing2_3	
	Bearing1_4	Bearing2_4	
	Bearing1_5	Bearing2_5	Bearing3_3
	Bearing1_6	Bearing2_6	
	Bearing1_7	Bearing2_7	

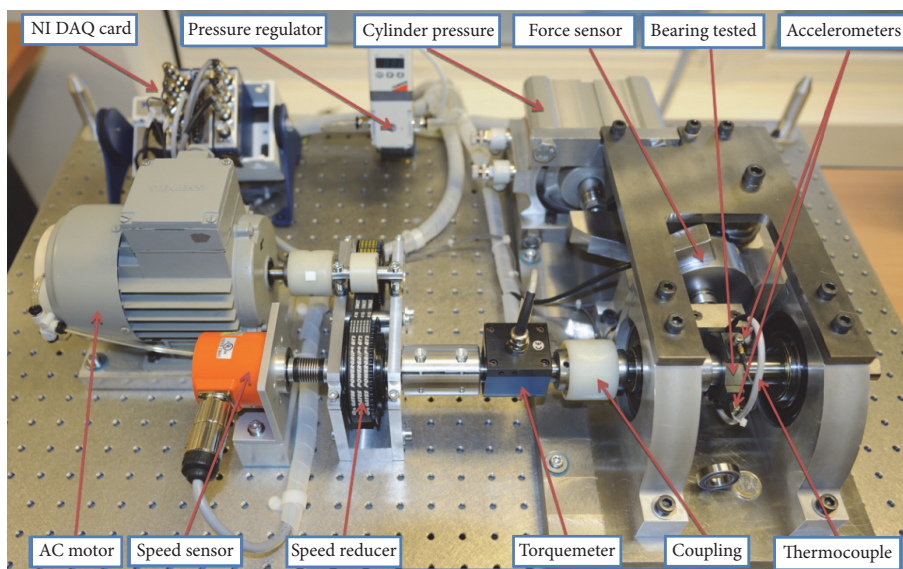


FIGURE 12: Overview of PRONOSTIA.

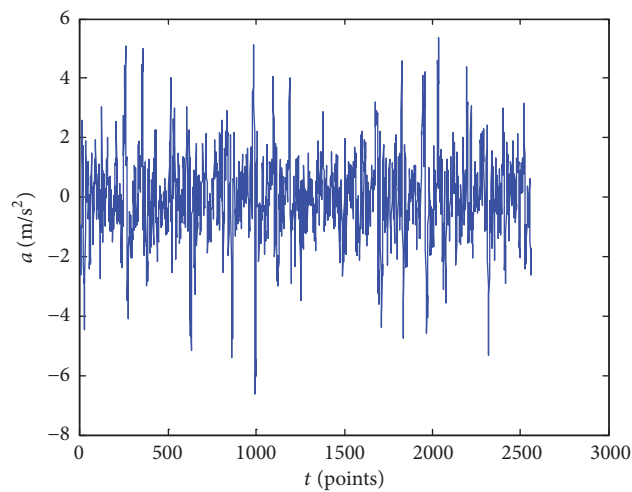


FIGURE 13: The signal of #2600.

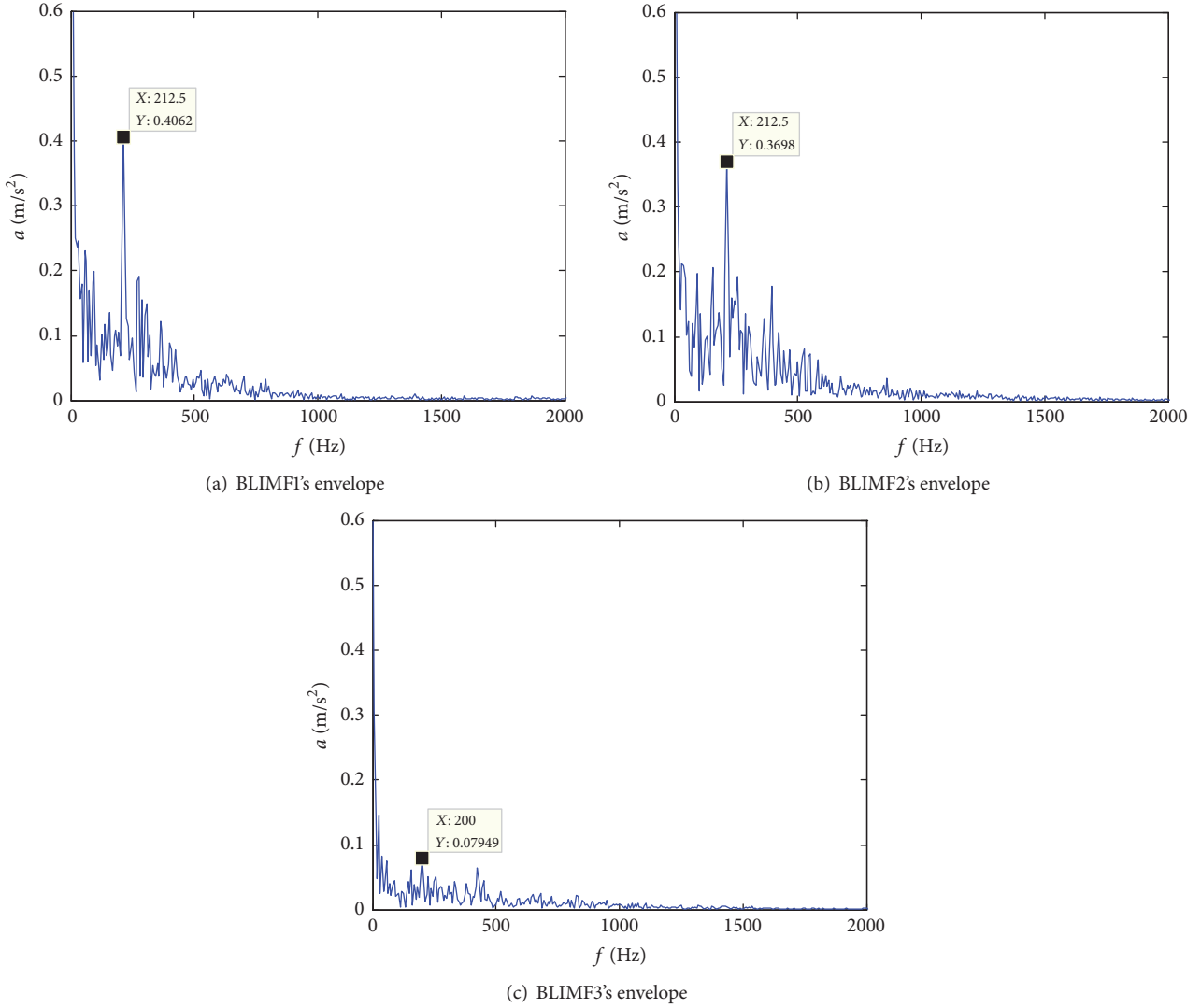


FIGURE 14: The envelope spectrum of BLIMF1 to BLIMF3 of #2600.

TABLE 3: Characteristics of tested bearings.

Z (ball numbers of the REB)	13
d (diameter of the REB)	3.5 mm
Dm (bearing mean diameter)	25.6 mm
r (rotation rate)	1800 r/min

decomposed into 3 BLIMFs and the envelope spectrum is shown in Figure 14. It is obvious that BLIMF1 and BLIMF2 have the frequency of inner defect. So Bearing1.1 gets inner defect finally.

By extracting the amplitude of all BLIMF1 and BLIMF2' defect frequency, an ADF of all Bearing1.1's data is shown in Figure 15.

From Figure 15, there are no evident boundaries of each degradation stage. At the end of the bearing's life, there is a sudden increase. If we set the segment number as 3, the result is shown in Figure 16. The normal stage is from #0 to #1432,

slight stage is from #1433 to #2264, and severe stage is from #2265 to #2803.

#### 4. Conclusions

This paper has proposed a method to assess the performance degradation of REB using VMD and GGCTSS. We have given a novel method to optimize the VMD parameter. By using GGCTSS, we can effectively segment the degradation process. From the above analysis, we can conclude that

- (1) the ADF extracted by VMD can commendably reflect the degradation development of REBs;
- (2) compared with crisp time series segmentation, the GGCTSS is more suitable for PDA of REBs.

However, there are also some problems that should be focused on in the future study, for example, to optimize the selection of GGCTSS segment number.

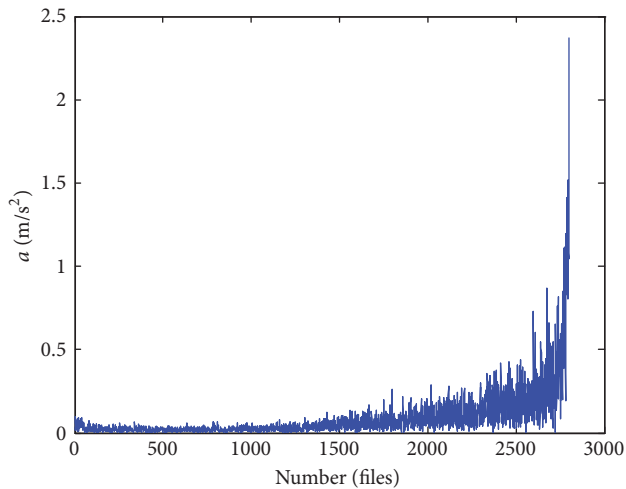


FIGURE 15: The ADF of the Bearing1\_L.

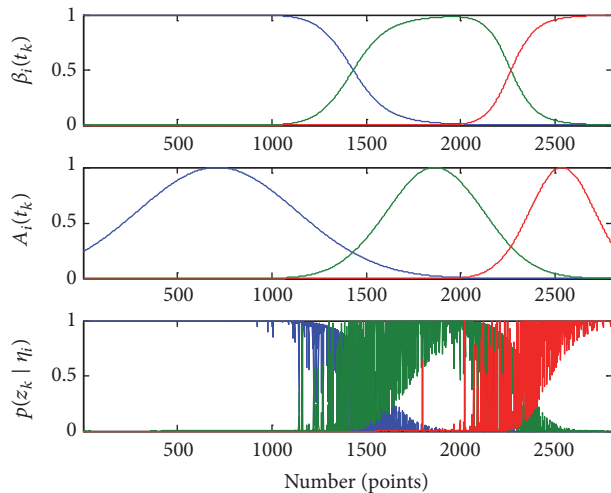


FIGURE 16: The result of Bearing1\_L's ADF based on GGCTSS.

## Conflicts of Interest

The authors declare that they have no conflicts of interest.

## Acknowledgments

This project is supported by National Natural Science Foundation of China (Grant no. 51541506). The authors also appreciate the Centre for Intelligent Maintenance System and FEMTO-ST Institute for providing the experimental data.

## References

- [1] I. El-Thalji and E. Jantunen, "A summary of fault modelling and predictive health monitoring of rolling element bearings," *Mechanical Systems and Signal Processing*, vol. 60-61, pp. 252–272, 2015.
- [2] W. Caesarendra, B. Kosasih, A. K. Tieu, H. Zhu, C. A. S. Moodie, and Q. Zhu, "Acoustic emission-based condition monitoring methods: review and application for low speed slew bearing," *Mechanical Systems and Signal Processing*, vol. 72-73, pp. 134–159, 2016.
- [3] Y. Iwai, T. Honda, T. Miyajima, S. Yoshinaga, M. Higashi, and Y. Fuwa, "Quantitative estimation of wear amounts by real time measurement of wear debris in lubricating oil," *Tribology International*, vol. 43, no. 1-2, pp. 388–394, 2010.
- [4] S. Taylor and K. Wiggins, "Diagnosis of bearing defects using a heterodyning ultrasound detector," *Journal of Failure Analysis and Prevention*, vol. 15, no. 4, pp. 470–473, 2015.
- [5] P. Bošković, M. Gašperin, D. Petelin, and Đ. Juričić, "Bearing fault prognostics using Rényi entropy based features and Gaussian process models," *Mechanical Systems and Signal Processing*, vol. 52-53, pp. 327–337, 2015.
- [6] R. Q. Yan, Y. B. Liu, and R. X. Gao, "Permutation entropy: a nonlinear statistical measure for status characterization of rotary machines," *Mechanical Systems and Signal Processing*, vol. 29, no. 5, pp. 474–484, 2012.
- [7] H. Li, Y. Wang, B. Wang, J. Sun, and Y. Li, "The application of a general mathematical morphological particle as a novel indicator for the performance degradation assessment of a bearing," *Mechanical Systems and Signal Processing*, vol. 82, no. 1, pp. 490–502, 2014.
- [8] M. Pan and W. Tsao, "Using appropriate IMFs for envelope analysis in multiple fault diagnosis of ball bearings," *International Journal of Mechanical Sciences*, vol. 69, pp. 114–124, 2013.
- [9] K. Dragomiretskiy and D. Zosso, "Variational mode decomposition," *IEEE Transactions on Signal Processing*, vol. 62, no. 3, pp. 531–544, 2014.
- [10] Y. Wang and R. Markert, "Filter bank property of variational mode decomposition and its applications," *Signal Processing*, vol. 120, pp. 509–521, 2016.
- [11] R. K. Tripathy, L. N. Sharma, and S. Dandapat, "Detection of shockable ventricular arrhythmia using variational mode decomposition," *Journal of Medical Systems*, vol. 40, no. 4, article no. 79, pp. 1–13, 2016.
- [12] S. Lahmiri, "Intraday stock price forecasting based on variational mode decomposition," *Journal of Computational Science*, vol. 12, pp. 23–27, 2016.
- [13] Y. Zhang, K. Liu, L. Qin, and X. An, "Deterministic and probabilistic interval prediction for short-term wind power generation based on variational mode decomposition and machine learning methods," *Energy Conversion and Management*, vol. 112, pp. 208–219, 2016.
- [14] A. A. Abdoos, P. K. Mianaei, and M. R. Ghadikolaei, "Combined VMD-SVM based feature selection method for classification of power quality events," *Applied Soft Computing*, vol. 38, pp. 637–646, 2016.
- [15] J. Zhu, C. Wang, Z. Hu, F. Kong, and X. Liu, "Adaptive variational mode decomposition based on artificial fish swarm algorithm for fault diagnosis of rolling bearings," *Proceedings of the Institution of Mechanical Engineers, Part C: Journal of Mechanical Engineering Science*, vol. 231, no. 4, pp. 635–654, 2017.
- [16] G. Tang and X. Wang, "Parameter optimized variational mode decomposition method with application to incipient fault diagnosis of rolling bearing," *Journal of Xi'an Jiaotong University*, vol. 49, no. 5, pp. 73–81, 2015.
- [17] Y. Pan, J. Chen, and X. Li, "Bearing performance degradation assessment based on lifting wavelet packet decomposition and fuzzy c-means," *Mechanical Systems and Signal Processing*, vol. 24, no. 2, pp. 559–566, 2010.

- [18] B. Wang, H.-R. Li, Q.-H. Chen, and B.-H. Xu, "Rolling bearing performance degradative state recognition based on mathematical morphological fractal dimension and fuzzy center means," *Acta Armamentarii*, vol. 36, no. 10, pp. 1982–1990, 2015.
- [19] H. Qiu, J. Lee, J. Lin, and G. Yu, "Wavelet filter-based weak signature detection method and its application on rolling element bearing prognostics," *Journal of Sound and Vibration*, vol. 289, no. 4-5, pp. 1066–1090, 2006.
- [20] T. Williams, X. Ribadeneira, S. Billington, and T. Kurfess, "Rolling element bearing diagnostics in run-to-failure lifetime testing," *Mechanical Systems and Signal Processing*, vol. 15, no. 5, pp. 979–993, 2001.
- [21] I. El-Thalji and E. Jantunen, "A descriptive model of wear evolution in rolling bearings," *Engineering Failure Analysis*, vol. 45, pp. 204–224, 2014.
- [22] J. Himberg, K. Korpiaho, H. Mannila, J. Tikanmäki, and H. T. T. Toivonen, "Time series segmentation for context recognition in mobile devices," in *Proceedings of the 1st IEEE International Conference on Data Mining (ICDM '01)*, pp. 203–210, December 2001.
- [23] A. Kehagias, E. Nidelkou, and V. Petridis, "A dynamic programming segmentation procedure for hydrological and environmental time series," *Stochastic Environmental Research and Risk Assessment (SERRA)*, vol. 20, no. 1-2, pp. 77–94, 2006.
- [24] A. Gedikli, H. Aksoy, N. E. Unal, and A. Kehagias, "Modified dynamic programming approach for offline segmentation of long hydrometeorological time series," *Stochastic Environmental Research and Risk Assessment*, vol. 24, no. 5, pp. 547–557, 2010.
- [25] J. Abonyi, B. Feil, S. Nemeth, and P. Arva, "Modified Gath-GEVa clustering for fuzzy segmentation of multivariate time-series," *Fuzzy Sets and Systems. An International Journal in Information Science and Engineering*, vol. 149, no. 1, pp. 39–56, 2005.
- [26] P. Nectoux, R. Gouriveau, and K. Medjaher, "An experimental platform for bearings accelerated life test," in *Proceedings of the IEEE International Conference on Prognostics and Health Management*, Denver, CO, USA, 2012.

## Research Article

# Study on Frequency Characteristics of Rotor Systems for Fault Detection Using Variational Mode Decomposition

Kai Chen,<sup>1,2</sup> Xin-Cong Zhou,<sup>1,2</sup> Jun-Qiang Fang,<sup>1,2</sup> and Li Qin<sup>3</sup>

<sup>1</sup>Key Laboratory of High Performance Ship Technology (Wuhan University of Technology), Ministry of Education, Wuhan 430063, China

<sup>2</sup>Reliability Engineering Institute, School of Energy and Power Engineering, Wuhan University of Technology, Wuhan 430063, China

<sup>3</sup>School of Machinery and Automation, Wuhan University of Science and Technology, Wuhan 430081, China

Correspondence should be addressed to Kai Chen; kaichen@whut.edu.cn

Received 28 April 2017; Revised 10 July 2017; Accepted 16 July 2017; Published 14 August 2017

Academic Editor: Adam Glowacz

Copyright © 2017 Kai Chen et al. This is an open access article distributed under the Creative Commons Attribution License, which permits unrestricted use, distribution, and reproduction in any medium, provided the original work is properly cited.

Due to the complicated structure, vibration signal of rotating machinery is multicomponent with nonstationary and nonlinear features, so it is difficult to diagnose faults effectively. Therefore, effective extraction of vibration signal characteristics is the key to diagnose the faults of rotating machinery. Mode mixing and illusive components existed in some conventional methods, such as EMD and EEMD, which leads to misdiagnosis in extracting signals. Given these reasons, a new fault diagnosis method, namely, variation mode decomposition (VMD), was proposed in this paper. VMD is a newly developed technique for adaptive signal decomposition, which can decompose a multicomponent signal into a series of quasi-orthogonal intrinsic mode functions (IMFs) simultaneously, corresponding to the components of signal clearly. To further research on VMD method, the advantages and characteristics of VMD are investigated via numerical simulations. VMD is then applied to detect oil whirl and oil whip for rotor systems fault diagnosis via practical vibration signal. The experimental results demonstrate the effectiveness of VMD method.

## 1. Introduction

For a long time, faults of rotating machinery were mainly diagnosed by spectrum analysis method of vibration signal, which determine the failure by analyzing the frequency spectrum or frequency characteristics of vibration signals [1]. Practically, the vibration signal is generally nonstationary and nonperiodic when the fault occurs, so the traditional FFT cannot meet the needs of the time-varying and nonstationary signals detection and time-frequency analysis [2].

Like many fault signals, the vibration signal of rotor system is a typical nonlinear and nonstationary time-varying signal whose frequency components change over time [3]. The feature extracting of fault signal not only affects the accuracy of fault diagnosis, but also may lead to misdiagnosis. Therefore, effective extraction of vibration signal characteristics is the key to diagnose the faults of rotating machinery [4].

Analysis, processing, and feature extraction of nonlinear and nonstationary signal always are one of the hot topics concerning engineers and researchers [5–7]. EMD is an effective signal analysis method which is suitable for dealing with nonlinear and nonstationary signals [8]. It consists in a local and fully data-driven separation of a signal with fast and slow oscillations. However, EMD experiences some problems, such as end effect and mode mixing [9]. To overcome shortcomings, the ensemble empirical mode decomposition (EEMD) was proposed [10], which can suppress the appearance of modal mixing. But both of them lack theoretical support. Besides being recursive decomposition, error of envelope line will be spread; thus they cannot eliminate the problem of modal mixing completely.

Dragomiretskiy and Zosso [11] have proposed a new adaptive decomposition method called variational mode decomposition (VMD) in 2014, which can nonrecursively

decompose a signal into a number of intrinsic mode functions (IMFs). In the process of decomposition, by using alternate direction multipliers method (ADMM), the center frequency and bandwidth of each modal were updated, to search the optimal solution of the signal decomposition. The updating process of each mode is carried out synchronously and makes the component of each modal in the corresponding baseband, finally, to achieve the effective decomposition of the signal. Compared with EMD and EEMD, VMD does not strip the signal step by step, but decomposes the signal synchronously. It is nonrecursive and reduces the spread of error. This method also has a good theoretical basis which is easy to understand. Besides, it has stronger robustness to noise [12, 13]. With its advantages, VMD is a wide application in the research field of signal denoising [14, 15], feature extraction [16, 17], image processing [18], energy and economics price forecasting [19, 20], speech signals detection [21], and especially in fault diagnosis [22–25]. However, these literatures mainly focus on the advantages of VMD comparing with the EMD and EEMD, rather than investigating the own capabilities of the VMD in signal analysis. The research of VMD needs to be conducted in depth. For this reason, a further investigation of the VMD is conducted in this paper via both numerical simulation and experimental approaches.

In this paper, the characteristics of VMD are investigated based on the theoretical of VMD, as well as the advantages of VMD. And then, VMD is applied to detect the fault of oil whirl and oil whip in rotor systems. This provides an effective solution for fault diagnosis of rotor system.

## 2. Variational Mode Decomposition

**2.1. EMD and EEMD Method.** EMD is a time-frequency signal analysis method for nonlinear signals, which can decompose the data adaptively and obtain a series of IMFs [9]. These IMFs reflect the characteristics of the signal itself. EMD algorithm is very suitable for analyzing the nonstationary signal.

Each signal could be decomposed into a number of intrinsic mode functions (IMFs), each of which must satisfy the following definition [9]:

(1) In the whole data set, the number of extrema and the number of zero-crossings must either be equal or differ at most by one.

(2) At any point, the mean value of the envelope defined by local maxima and the envelope defined by the local minima is zero.

With the definition, any signal  $x(t)$  can be decomposed as follows [9]:

(1) Identify all local maxima and all local minima in the signal  $x(t)$ .

(2) Connect all local maxima and all local minima by using a cubic spline line as the upper envelope  $e_u(t)$  and the lower envelope  $e_l(t)$ , respectively. The mean  $m_1(t)$  of upper and low envelope is calculated by using the equation

$$m_1(t) = \frac{(e_u(t) + e_l(t))}{2}. \quad (1)$$

(3) Calculate the equation

$$h_1(t) = x(t) - m_1(t) \quad (2)$$

and examine whether the resultant  $h_1(t)$  is an IMF satisfying the two aforementioned conditions. If  $h_1(t)$  is not an IMF, regard  $h_1(t)$  as original signal and repeat steps (1)–(3) until  $h_1(t)$  is an IMF.

(4) Separate the first IMF from  $x(t)$  and then get the residual component  $r_1(t)$ :

$$r_1(t) = x(t) - h_1(t). \quad (3)$$

Treat  $r_1(t)$  as original data and repeat the above processes; therefore the second IMF  $h_2(t)$  is obtained. Iterate the previous calculations  $n$  times and  $n$  IMFs of the signal could be got. Then

$$r_n(t) = r_{n-1}(t) - h_n(t). \quad (4)$$

The decomposition process can be stopped when the final residual component  $r_1(t)$  is a monotonic function or a constant from which no more IMF can be extracted.

(5) The original signal  $x(t)$  finally can be expressed as

$$x(t) = \sum_{i=1}^n h_i(t) + r_n(t). \quad (5)$$

Thus, one can achieve a decomposition of the signal into  $n$ -empirical modes, and a residue  $r_n(t)$ , which is the mean trend of  $x(t)$ . The IMFs  $h_1(t), h_2(t), \dots, h_n(t)$  include different frequency bands ranging from high to low.

EMD is a self-adaptive signal decomposition method, and the obtained IMFs have the advantages of mutual orthogonality. However, practice has disclosed that the EMD also shows the following defects in signal processing and feature extraction.

(1) *No Mathematical Foundation.* Without strict mathematical proof and mathematical model, EMD lacks theoretical support. And there is no valid way to stop the decomposition process in the sifting process of EMD.

(2) *End Effect.* In the decomposition process, endpoint will be used as an extreme point for fitting the upper and lower envelopes. But if the endpoint is not an extreme point, the fitted curve using cubic spline line will have some error. This error will impact on each subsequent decomposition step; the error will accumulate gradually and then is likely to pollute the internal decomposed results from both ends.

(3) *Mode Mixing.* Mode mixing occurs in EMD; when steps change, pulse interference and outside noise will show in the signal. There are two forms of mode mixing; one form is a single IMF including oscillations of dramatically disparate scales and the other is a component of a similar scale residing in different IMFs. Once the mode mixing is generated, subsequent decomposition step will be influenced, even making IMFs meaningless in physical interpretation.

To alleviate the mode mixing problem occurring in EMD, an ensemble empirical mode decomposition (EEMD)

is presented [26]. The essential essence of EEMD algorithm is decomposing the original signal added Gaussian noise repeatedly by EMD method, and the original vibration data is decomposed into a series of IMFs with different scales and continuous characteristics because of the characteristic of frequency uniform distribution of Gaussian white noise, which can suppress the appearance of modal mixing.

**2.2. VMD Method.** VMD is a new signal analysis method for nonlinear and nonstationary signal, which aims to decompose the signal into different discrete modes [11]. The VMD has a solid mathematical foundation, which is able to decompose a signal into an ensemble of band-limited intrinsic mode functions (IMFs) simultaneously. IMFs are redefined as amplitude modulated frequency modulated (AM-FM) signals, written as

$$u_k(t) = A_k(t) \cos(\varphi_k(t)), \quad (6)$$

where  $u_k(t)$  is IMF,  $A_k(t)$  is nonnegative envelope, and  $\varphi_k(t)$  is the phase and a nondecreasing function.

The core of VMD is to construct and solve the variational problem, the decomposition process of VMD algorithm is the solution of the variational problem. There are three important concepts in the signal processing, Wiener Filtering, Hilbert transform, and frequency mixing, which constitute the building blocks of VMD model.

Assume each mode  $u_k$  is band-limited and compactly distributed around with a center frequency  $w_k$ , so the solution of variational problem turns to seeking for  $k$  modes  $u_k$  to make the sum of the bandwidth minimized, while the constraint condition is the sum of modes equal to the input signal  $f$ . The principle of the VMD algorithm is the following:

(1) The analytic signal of mode  $u_k$  was computed by means of Hilbert transform, so obtain the unilateral spectrum of the analytic signal.

$$\delta(t) + \frac{j}{\pi(t)} * u_k(t). \quad (7)$$

(2) Shift the frequency spectrum of each mode to the respective estimated central frequency.

$$\left[ \delta(t) + \frac{j}{\pi(t)} * u_k(t) \right] \cdot e^{-jw_k t}. \quad (8)$$

(3) The bandwidth is estimated through the Gaussian smoothness of the demodulated signal, that is, the squared  $L^2$ -norm of the gradient. The resulting constrained variational problem is given by the following:

$$\begin{aligned} \min_{\{u_k, w_k\}} & \left\{ \sum_k \left\| \partial_t \left[ \delta(t) + \frac{j}{\pi(t)} * u_k(t) \right] \cdot e^{-jw_k t} \right\|_2^2 \right\} \\ \text{s.t.} & \sum_k u_k = f, \end{aligned} \quad (9)$$

where  $\{u_k\} := \{u_1, \dots, u_k\}$  and  $\{w_k\} := \{w_1, \dots, w_k\}$  are the identified set of modes and their central frequencies.

(4) A quadratic penalty term  $\alpha$  and a Lagrangian multiplier factor  $\lambda(t)$  are introduced in order to render the problem unconstrained. The quadratic penalty is a classic way to encourage reconstruction fidelity, and the Lagrangian multipliers are a common way of enforcing constraints strictly. The augmented Lagrangian is shown as follows:

$$\begin{aligned} L(\{u_k\}, \{w_k\}, \lambda) &= \alpha \sum_k \left\| \left[ \delta(t) + \frac{j}{\pi(t)} * u_k(t) \right] \cdot e^{-jw_k t} \right\|_2^2 \\ &+ \left\| f(t) - \sum_k u_k(t) \right\|_2^2 \\ &+ \left\langle \lambda(t), f(t) - \sum_k u_k(t) \right\rangle. \end{aligned} \quad (10)$$

(5) An alternate direction multipliers method (ADMM) is applied to solve the original minimization problem, to find the saddle point of the augmented Lagrange expression via updating  $u_k^{n+1}$ ,  $w_k^{n+1}$ , and  $\lambda_k^{n+1}$  alternately. So the signal was decomposed into different discrete modes adaptively.

The flowchart of VMD methods is shown in Figure 1, and the detailed steps are as follows.

(1) Initialize  $\{\hat{u}_k^1\}$ ,  $\{w_k^1\}$ ,  $\hat{\lambda}^1$  and  $n = 0$ .

(2)  $n = n + 1$ ; update  $\hat{u}_k$  and  $w_k$  according to (11) and (12).

$$\hat{u}_k^{n+1}(w) = \frac{\hat{f}(w) - \sum_{i \neq k} \hat{u}_i^n(w) + \hat{\lambda}^n(w)/2}{1 + 2\alpha(w - w_k^n)^2}, \quad (11)$$

$$w_k^{n+1} = \frac{\int_0^\infty w |\hat{u}_k^{n+1}(w)|^2 dw}{\int_0^\infty |\hat{u}_k^{n+1}(w)|^2 dw}, \quad (12)$$

where  $k = \{1, 2, \dots, K\}$ .

(3) Update  $\lambda$ .

$$\hat{\lambda}^{n+1}(w) = \hat{\lambda}^n(w) + \tau \left( \hat{f}(w) - \sum_k \hat{u}_k^{n+1}(w) \right). \quad (13)$$

(4) Repeat steps (2) and (3), until the following convergence condition is satisfied:

$$\frac{\sum_k \|\hat{u}_k^{n+1} - \hat{u}_k^n\|_2^2}{\|\hat{u}_k^n\|_2^2} < \varepsilon, \quad (14)$$

where  $\varepsilon \geq 0$  is the convergence tolerance.

To show the advantage of VMD, the simulated signal in (15) is decomposed by using EMD, EEMD, and VMD, respectively; the results are shown in Figure 2.

$$\begin{aligned} y_1 &= \sin(2\pi 30t), \\ y_2 &= \sin(2\pi 10t) * (t > 0.2), \\ y_3 &= \sin(2\pi 50t) * (t < 0.2), \\ y &= y_1 + y_2 + y_3. \end{aligned} \quad (15)$$

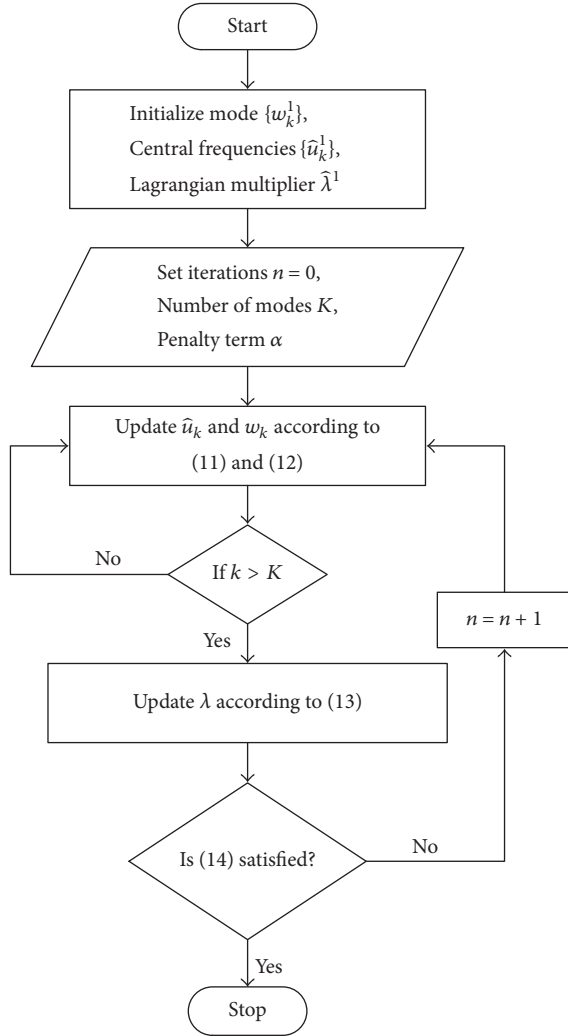


FIGURE 1: Flowchart of VMD.

It can be seen from Figure 2 that the three components of original signal were decomposed by VMD without mode mixing, while it is decomposed by VMD completely. The IMF2, IMF3, and IMF4 decomposed by EEMD are basically the same as the three components in the original signal, but mode mixing was not completely eliminated, and end effect still exists; furthermore, there is a high-frequency component IMF1. And the IMFs decomposed by EMD are hard to distinguish while the mode mixing still exists. In summary, VMD is better than EEMD and EMD in feature extraction of vibration signal.

### 3. Characteristics of VMD

Compared to EMD and EEMD, VMD has advantages in solving the problem of mode mixing and end effect. What is more, according to the principle and decomposition steps of VMD, the following characteristic of VMD can be obtained.

(1) *Adaptivity*. Unlike wavelet analysis which needs to select the best wavelet base, the signal was decomposed by VMD

without prior knowledge. Various signals can be decomposed into different IMFs according to information about the signal itself, and the IMFs correspond to the components of different frequency range and center frequency in the signal. This reflects adaptability of the VMD method.

(2) *Reconfigurability*. As mentioned before, the core of VMD is to solve the variational constraint problem, while the constraint condition is the sum of modes equal to the input signal. So the original signal can be reconstructed by the IMFs decomposed by the VMD, which was proved by formula (9) theoretically. The simulation signal of (15) was taken as an example to show that VMD is reconfigurable. The original signal, the reconstructed signal, and error curve are shown in Figure 3. It can be seen from the figure that the error is very small to explain the reconfigurability of VMD.

(3) *Smoothing Filtering*. VMD also has certain filtering characteristics. The simulation signal of (15) added a random noise which was decomposed by the VMD and reconstructed. The time and frequency domain of the original simulation signal, the simulation signal added noise, and the reconstructed signal were illustrated in Figure 4.

By comparing the original signal and the reconstructed signal, the added noise was eliminated, and the characteristic peaks of spectrum were more prominent and obvious after reconstitution. And, in the time domain, fluctuating character of the reconstructed signal is more clear than the signal added noise, which is hard to identify. VMD does have the smoothing filter characteristic.

This can also be deduced from the VMD algorithm in theory. It is observed from formula (11) that the quadratic penalty term  $\alpha$  is in the denominator. When  $\alpha$  increases, the bandwidth of each mode will be decreased, the spectrum becomes smooth, and the filtered and smoothed modal components are discarded as noise.

(4) *Orthogonality*. A series of modal components (IMFs) were decomposed by VMD; each modal component represents a feature of the original signal theoretically, so the modal components are orthogonal to each other. However, it is impossible to achieve absolute orthogonality between any two IMFs in practical applications; this is because of end effect and mode mixing. Firstly, the end effect of the VMD may result in IMF data diverge at both ends, thus creating a false component. The endpoint effect is more serious in the shorter length signal. In addition, there is no mode mixing in and between the IMFs theoretically, but there still exists mode mixing practically.

### 4. Examples of Application

4.1. *Experiment Setup and Signal Acquisition*. To evaluate the performance of VMD method, experimental analysis of a rotor system has been carried out in a rotor test rig. As shown in Figure 5, the rotor test rig is composed of electrical motor, shaft, rotor, bearing seat, coupling, sensor support, and foundation. An electrical motor with frequency converter, whose speed is up to 10,000 r/min, is the drive. The

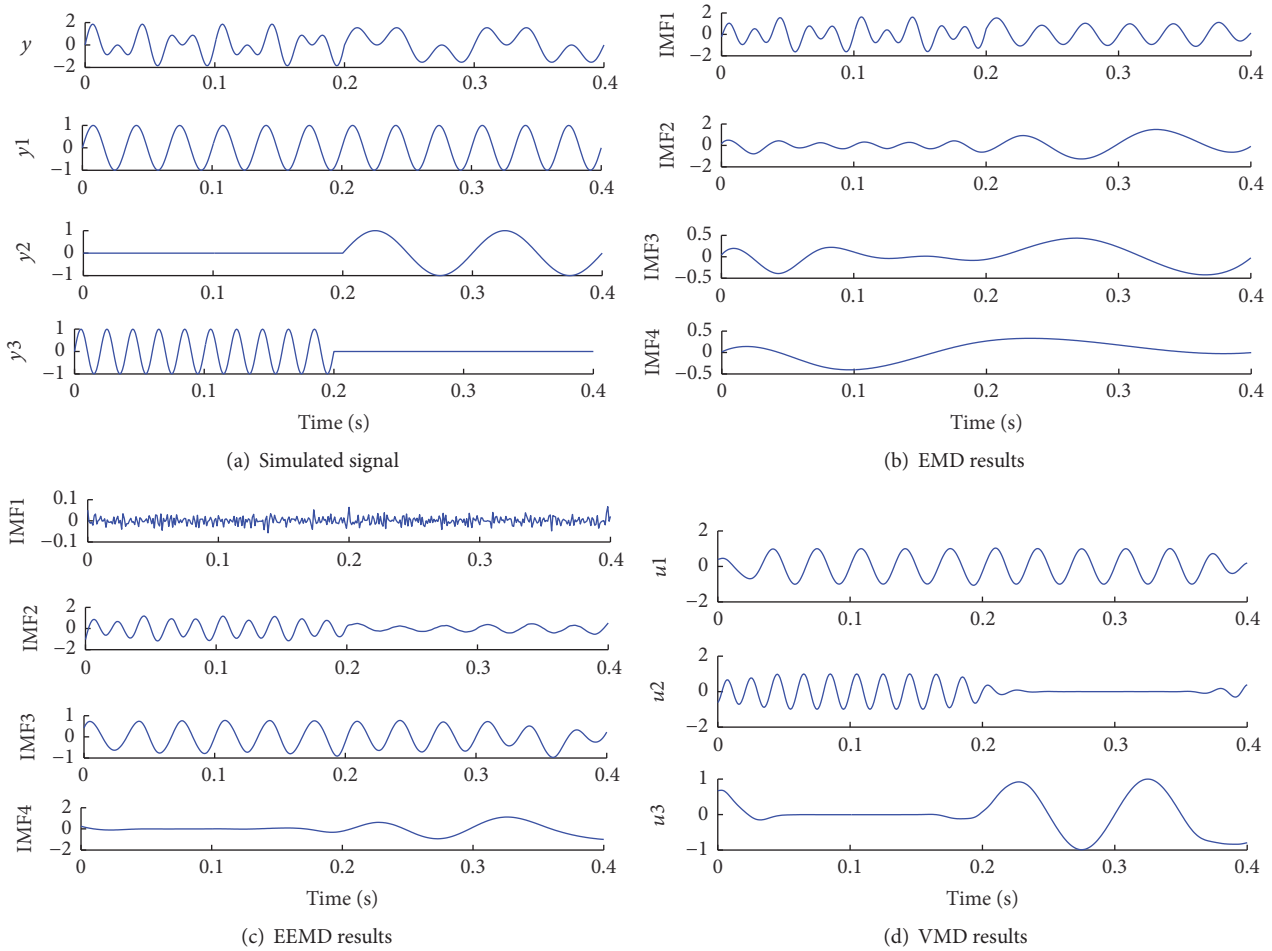


FIGURE 2: Comparison results of EMD, EEMD, and VMD.

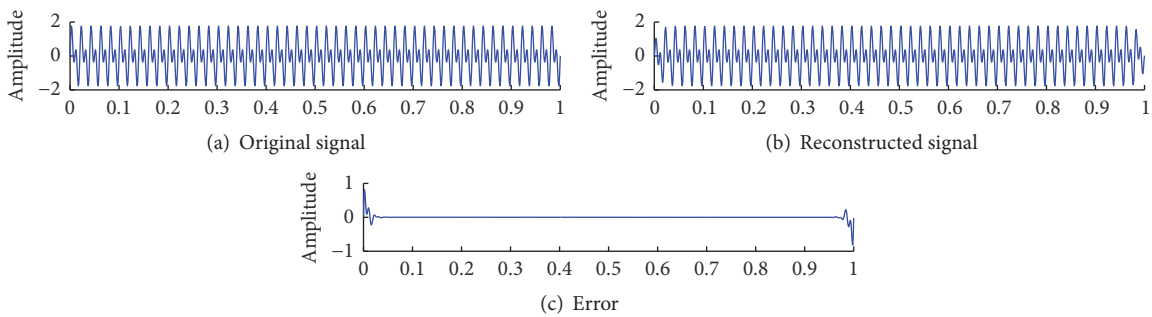


FIGURE 3: Reconfigurability of VMD.

oil film bearing and oil cup were designed to simulate the phenomenon of oil whip.

A phase sensor closed to the motor is fixed to measure the rotating speed. A velocity sensor (ZA-HV-2-5) is fixed on bearing seat in the middle of test rig to measure the vibration of bearing seat. Two eddy current sensors, fixed on sensor support closed to oil film bearing, are used to pick up horizontal and vertical directions displacement of rotor.

**4.2. Results and Discussion.** The oil film instability of the rotor system usually consists of two stages, oil whirl and oil whip. The whirl is a form of motion in which the rotor rotates around its own axis, while the axis rotates around the center of the bearing. When the rotational speed of the rotor reaches a certain speed, the oil whirl is generated, and the whirling frequency is about half of that speed. When the rotational speed is up to 2 times of the first-order critical speed of rotor system, the oil whirl turns into the oil whip, the amplitude

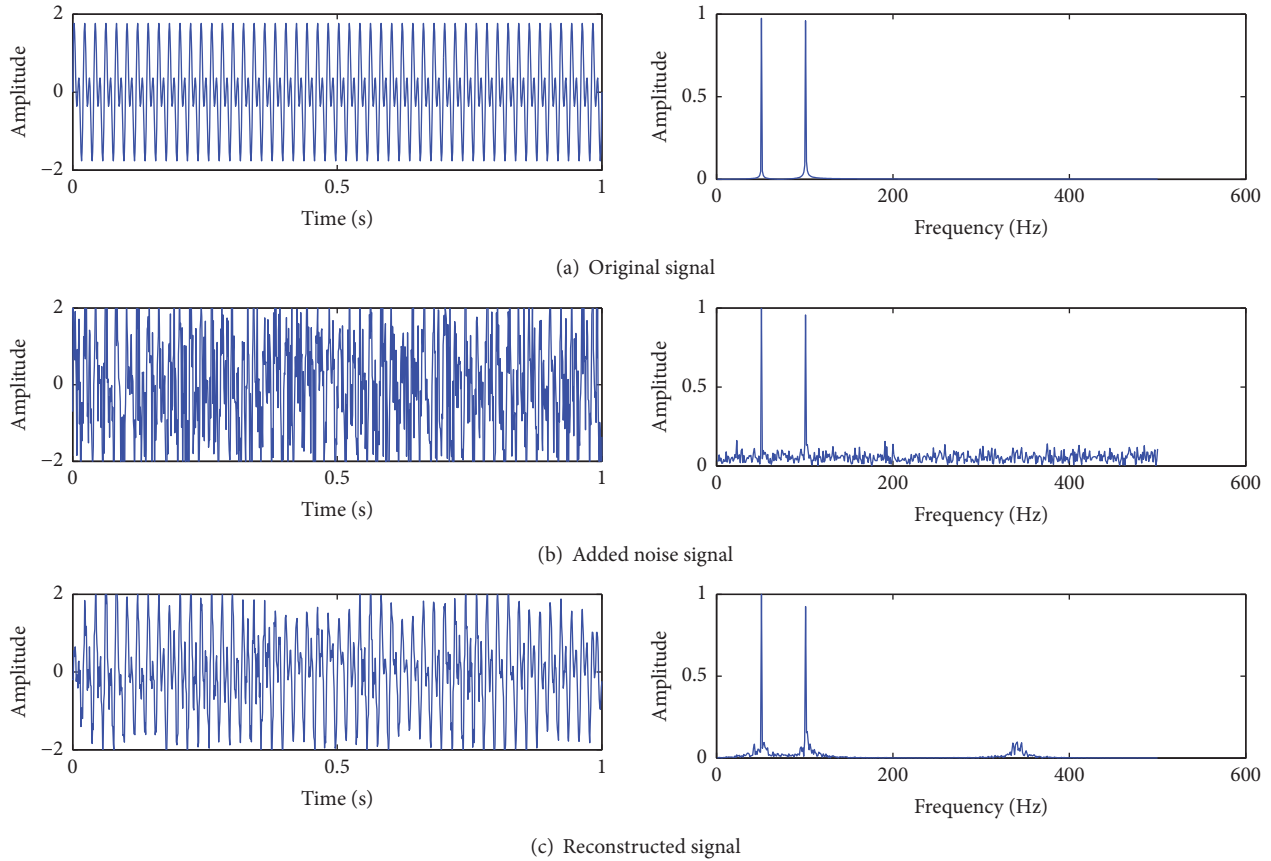


FIGURE 4: The filtering characteristics of VMD.

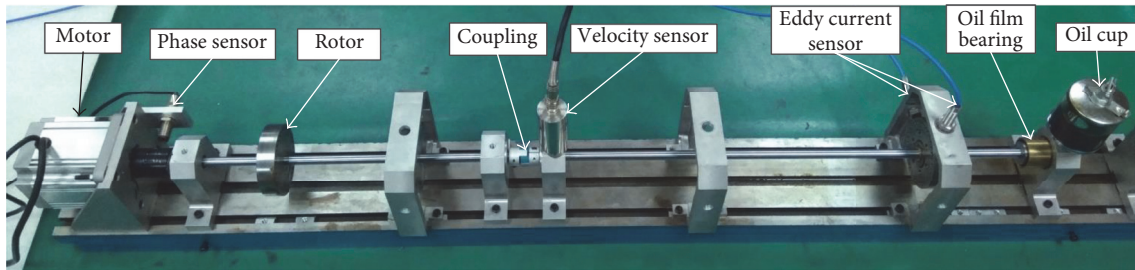


FIGURE 5: Experimental setup and sensor arranged.

of the rotor increases, and the whip frequency stabilizes in a certain value (first-order critical speed of rotor system). The fault feature extraction of oil whirl and oil whip is the main basis to diagnose these type faults.

In the process of oil film instability, the oil whirl occurs near the speed of 3100 r/min. When the rotational speed is up to 4500 r/min, the rotor system test rig shows bigger vibration because of the oil whip.

(1) *Oil Whirl*. The vibration signal and its spectrum of the oil whirl are shown in Figure 6. In the spectrum, the oil whirl frequency  $1/2x$  ( $\approx 26$  Hz) and rotating frequency  $1x$  ( $\approx 52$  Hz)

can be seen. The value of the oil whirl frequency is about half value of rotating frequency and the amplitude is higher than rotating frequency.

Five IMFs decomposed by VMD for oil whirl signal are shown in Figure 7(a), and it is decomposed completely. IMF1 is corresponding to the oil whirl frequency  $1/2x$  and IMF2 is corresponding to rotating frequency  $1x$ . IMF3 is corresponding to  $2x$ . IMF5 is corresponding to  $4x$ . The VMD results not only show the fault feature of oil whirl, but also present more periodicity components.

For comparison, IMFs analyzed by EEMD and EMD are shown in Figures 7(b) and 7(c). Although IMF2 and

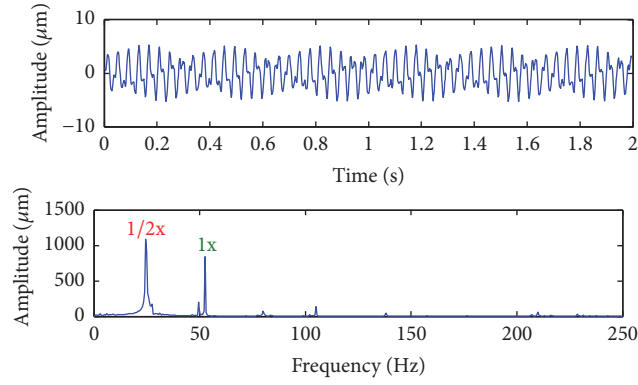
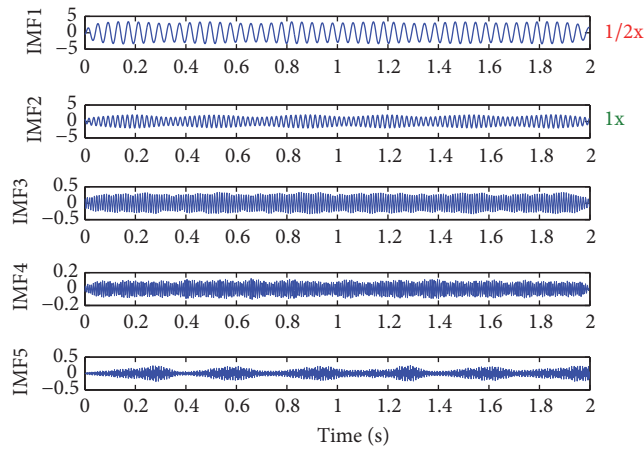
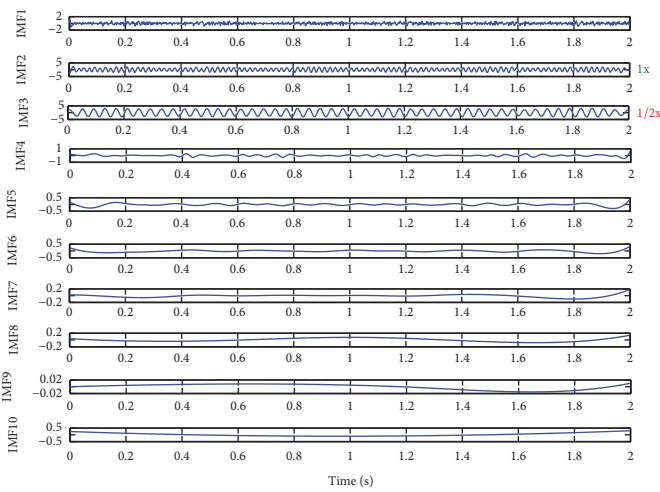


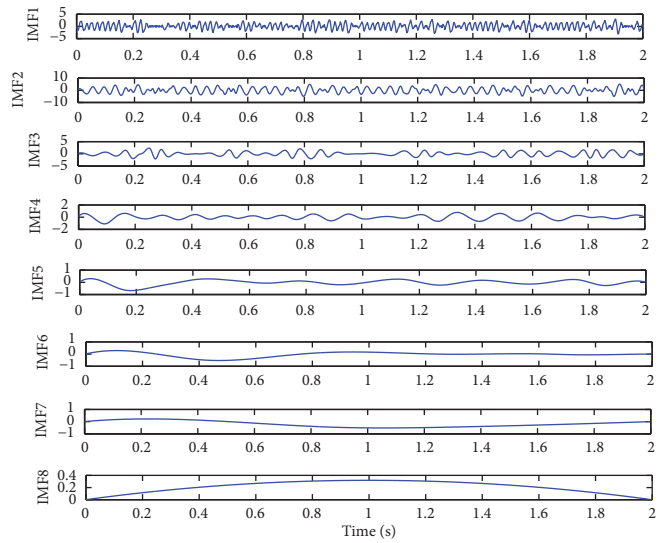
FIGURE 6: Time Domain waveform and spectrum of oil whirl signal.



(a) VMD decomposed results



(b) EEMD decomposed results



(c) EMD decomposed results

FIGURE 7: VMD, EEMD, and EMD decomposed results of oil whirl signal.

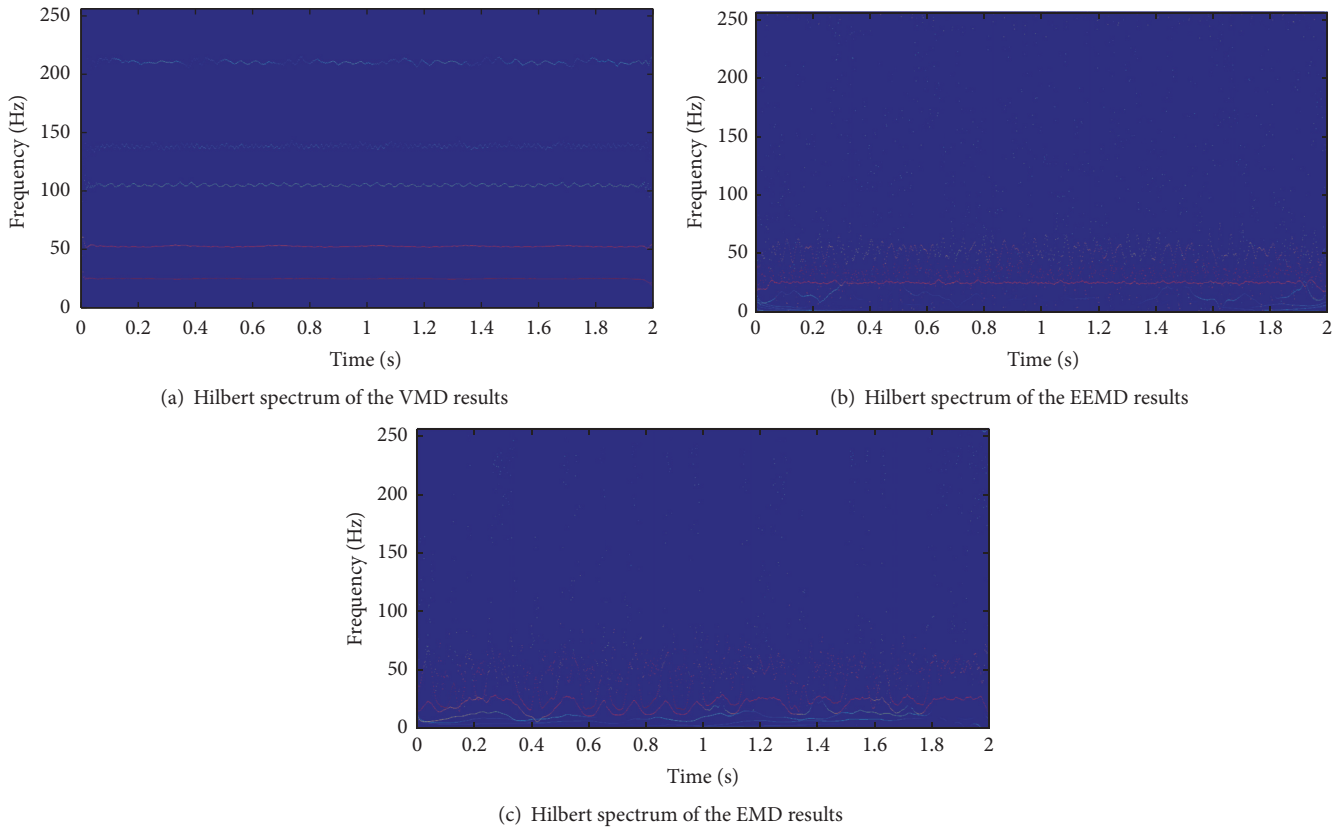


FIGURE 8: Hilbert spectrum of the VMD, EEMD, and EMD results of oil whirl signal.

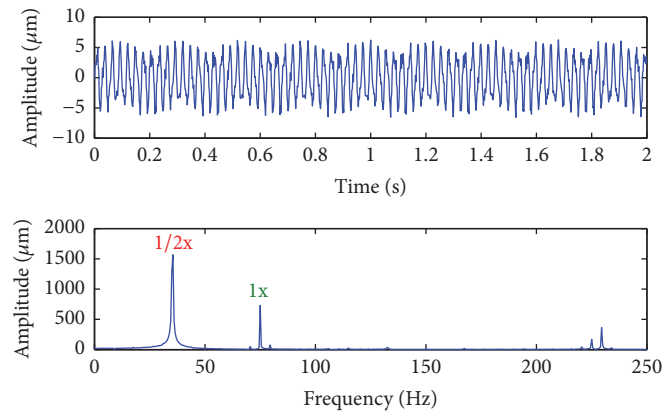


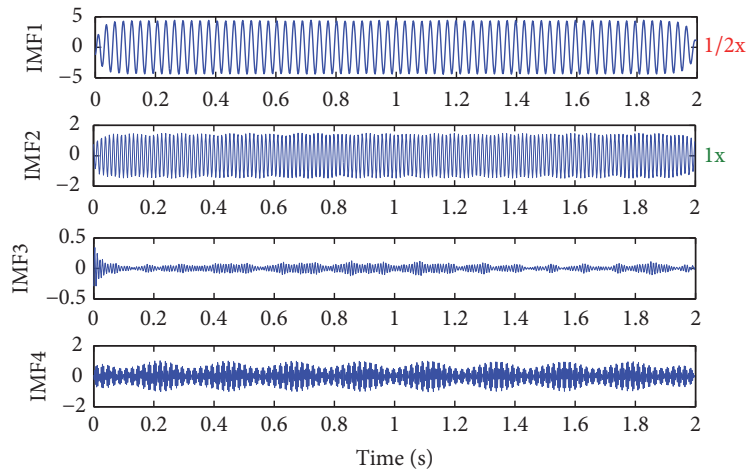
FIGURE 9: Time domain waveform and spectrum of oil whip signal.

IMF3 decomposed by EEMD are basically the same as the  $1x$  and  $1/2x$  components in the signal, there still exist mode mixing and additional frequency component in other IMFs. The mixing phenomenon is obvious in EMD results, which cannot show the feature of the oil whirl signal clearly.

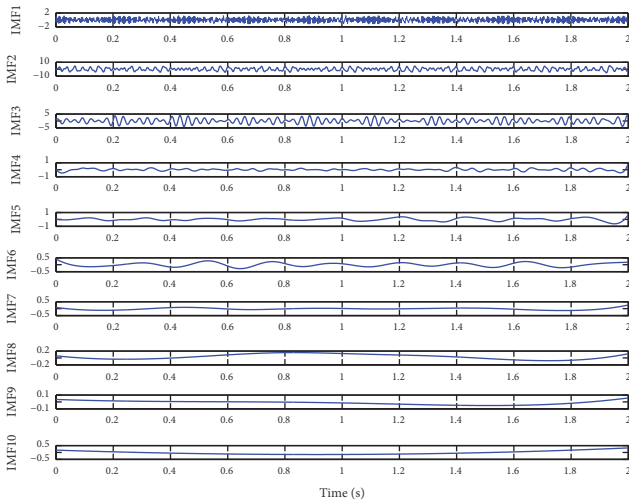
Furthermore, the time-frequency spectrum of the VMD, EEMD, and EMD results was analyzed. The Hilbert spectrum of each IMF decomposed by the VMD, EEMD, and EMD is shown in Figure 8. It can be seen from Figure 8 that the  $1/2x$ ,

$1x$ ,  $2x$ ,  $4x$  frequency components of IMFs, decomposed by VMD, are easy to be distinguished. And only  $1/2x$  component can be seen in the EEMD results, while the component of EMD results is very difficult to be resolved.

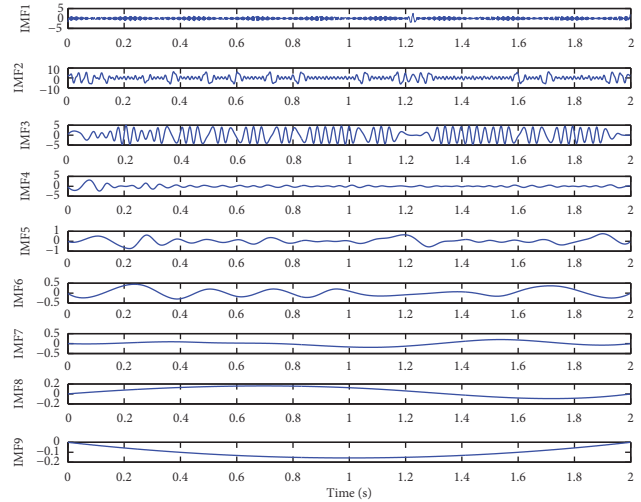
(2) *Oil Whip*. The waveform and spectrum of the oil whip signal are shown in Figure 9. In the spectrum, the oil whirl frequency  $1/2x$  ( $\approx 37$  Hz) and rotating frequency  $1x$  ( $\approx 75$  Hz) can be seen. The value of the oil whirl frequency is about half



(a) VMD decomposed results



(b) EEMD decomposed results



(c) EMD decomposed results

FIGURE 10: VMD, EEMD, and EMD decomposed results of oil whip signal.

value of rotating frequency and the amplitude is higher than rotating frequency.

Four IMFs obtained by VMD for oil whip signal are illustrated in Figure 10(a), and it is decomposed clearly. IMF1 and IMF2 are corresponding to  $1/2x$  and  $1x$ , respectively, and the  $3x$  frequency components are also extracted. Figures 10(b) and 10(c) separately show the IMFs using EEMD and EMD, in which signatures are difficult to be identified.

The Hilbert spectrum of each IMF decomposed by VMD, EEMD, and EMD is shown in Figure 11. As can be seen from Figure 11, all time-frequency representations of each component decomposed by VMD are clearly segregated, while the component of EEMD and EMD results is very difficult to be resolved.

The analysis results in Figures 7, 8, 10, and 11 show better effectiveness of VMD than EEMD and EMD, demonstrating the validity of VMD in detecting rotor faults.

## 5. Conclusion

VMD is a newly developed technique for adaptive signal decomposition, which can decompose a multicomponent signal into a series of quasi-orthogonal intrinsic mode functions simultaneously. Unlike EMD and EEMD, VMD has theoretical support and can solve the problem of mode mixing and end effect more effectively. It also has the characteristic of adaptivity, reconfigurability, smoothing filtering, and orthogonality.

VMD is proposed to determine the fault of rotor systems, and an experimental analysis has been carried out. Comparative analysis results show that VMD method is more effective than EEMD and EMD in fault feature extraction of oil whirl and oil whip, so VMD method has important practical application value for rotor fault diagnosis and should be further considered in the future.

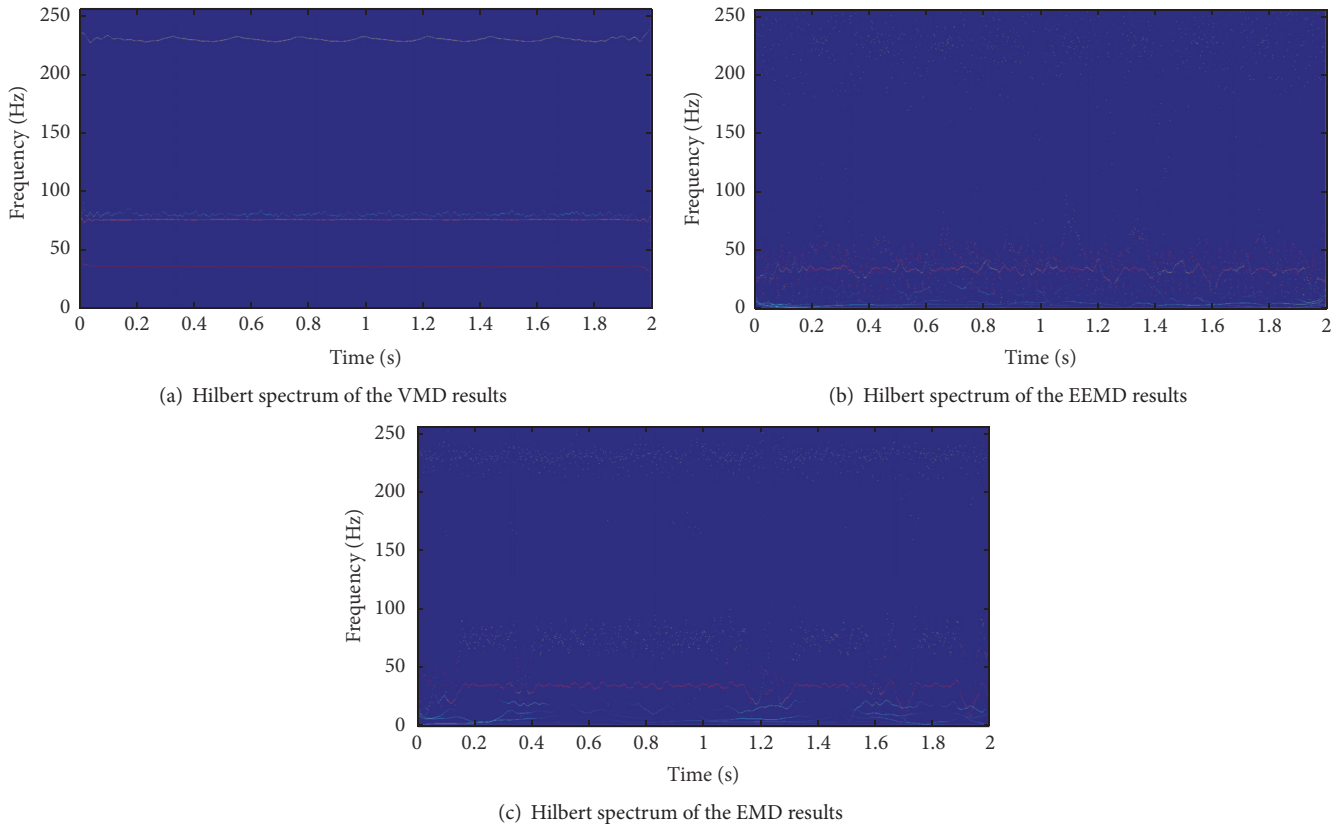


FIGURE 11: Hilbert spectrum of the VMD, EEMD, and EMD results of oil whip signal.

## Conflicts of Interest

The authors declare that there are no conflicts of interest regarding the publication of this paper.

## Acknowledgments

This project is sponsored by the grants from the Ministry of Transport Applied Basic Research Project (no. 2013329811360), the National Natural Sciences Foundation of China (no. 51139005, no. 51509194), and the Fundamental Research Funds for the Central Universities (no. 2014-yb-018).

## References

- [1] D. Yongzuo and Q. Zhiying, "Holo-spectrum analysis of rotating machinery dynamic signals," *Journal of Vibration, Measurement & Diagnosis*, vol. 22, no. 2, pp. 81–88, 2002.
- [2] Z. Li, Y. Jiang, C. Hu, and Z. Peng, "Recent progress on decoupling diagnosis of hybrid failures in gear transmission systems using vibration sensor signal: a review," *Measurement*, vol. 90, pp. 4–19, 2016.
- [3] D. H. Gonsalves, R. D. Neilson, and A. D. S. Barr, "A study of the response of a discontinuously nonlinear rotor system," *Nonlinear Dynamics*, vol. 7, no. 4, pp. 451–470, 1995.
- [4] N. Bachschmid, P. Pennacchi, and A. Vania, "Identification of multiple faults in rotor systems," *Journal of Sound and Vibration*, vol. 254, no. 2, pp. 327–366, 2003.
- [5] T.-A. Ensslin, M. Frommert, and F.-S. Kitaura, "Information field theory for cosmological perturbation reconstruction and non-linear signal analysis," *Physical Review D Particles & Fields*, vol. 80, no. 10, pp. 281–287, 2009.
- [6] G. Fele-Žorž, G. Kavšek, Ž. Novak-Antolič, and F. Jager, "A comparison of various linear and non-linear signal processing techniques to separate uterine EMG records of term and pre-term delivery groups," *Medical and Biological Engineering and Computing*, vol. 46, no. 9, pp. 911–922, 2008.
- [7] Z. Li, X. Yan, Z. Tian, C. Yuan, Z. Peng, and L. Li, "Blind vibration component separation and nonlinear feature extraction applied to the nonstationary vibration signals for the gearbox multi-fault diagnosis," *Measurement: Journal of the International Measurement Confederation*, vol. 46, no. 1, pp. 259–271, 2013.
- [8] J. Cheng, D. Yu, J. Tang, and Y. Yang, "Local rub-impact fault diagnosis of the rotor systems based on EMD," *Mechanism and Machine Theory*, vol. 44, no. 4, pp. 784–791, 2009.
- [9] N. E. Huang, Z. Shen, S. R. Long et al., "The empirical mode decomposition and the Hilbert spectrum for nonlinear and non-stationary time series analysis," *The Royal Society of London. Proceedings. Series A. Mathematical, Physical and Engineering Sciences*, vol. 454, no. 1971, pp. 903–995, 1998.
- [10] N. E. Huang, M. C. Wu, S. R. Long et al., "A confidence limit for the empirical mode decomposition and Hilbert spectral analysis," *Proceedings of the Royal Society A*, vol. 459, no. 2037, pp. 2317–2345, 2003.
- [11] K. Dragomiretskiy and D. Zosso, "Variational mode decomposition," *IEEE Transactions on Signal Processing*, vol. 62, no. 3, pp. 531–544, 2014.

- [12] Y. Wang and R. Markert, "Filter bank property of variational mode decomposition and its applications," *Signal Processing*, vol. 120, pp. 509–521, 2016.
- [13] W. Yang, Z. Peng, K. Wei, P. Shi, and W. Tian, "Superiorities of variational mode decomposition over empirical mode decomposition particularly in time–frequency feature extraction and wind turbine condition monitoring," *IET Renewable Power Generation*, vol. 11, no. 4, pp. 443–452, 2017.
- [14] S. Lahmiri, "Comparative study of ECG signal denoising by wavelet thresholding in empirical and variational mode decomposition domains," *Healthcare Technology Letters*, vol. 1, no. 3, pp. 104–109, 2014.
- [15] N. Mohan, S. Sachin Kumar, P. Poornachandran, and K. P. Soman, "Modified variational mode decomposition for power line interference removal in ECG signals," *International Journal of Electrical and Computer Engineering*, vol. 6, no. 1, pp. 151–159, 2016.
- [16] A. Mert, "ECG feature extraction based on the bandwidth properties of variational mode decomposition," *Physiological Measurement*, vol. 37, no. 4, pp. 530–543, 2016.
- [17] P. Shi and W. Yang, "Precise feature extraction from wind turbine condition monitoring signals by using optimised variational mode decomposition," *IET Renewable Power Generation*, vol. 11, no. 3, pp. 245–252, 2017.
- [18] V. Vishnu Pradeep, V. Sowmya, and K. P. Soman, "Variational mode decomposition based multispectral and panchromatic image fusion," *International Journal of Control Theory and Applications*, vol. 9, no. 16, pp. 8051–8059, 2016.
- [19] G. Sun, T. Chen, Z. Wei, Y. Sun, H. Zang, and S. Chen, "A carbon price forecasting model based on variational mode decomposition and spiking neural networks," *Energies*, vol. 9, no. 1, article 54, 2016.
- [20] S. Lahmiri, "Comparing variational and empirical mode decomposition in forecasting day-ahead energy prices," *IEEE Systems Journal*, no. 99, pp. 1–4, 2015.
- [21] A. Upadhyay and R. B. Pachori, "Instantaneous voiced/non-voiced detection in speech signals based on variational mode decomposition," *Journal of the Franklin Institute*, vol. 352, no. 7, pp. 2679–2707, 2015.
- [22] C. Yi, Y. Lv, and Z. Dang, "A fault diagnosis scheme for rolling bearing based on particle swarm optimization in variational mode decomposition," *Shock and Vibration*, vol. 2016, Article ID 9372691, 10 pages, 2016.
- [23] Z. Lv, B. Tang, Y. Zhou, and C. Zhou, "A novel method for mechanical fault diagnosis based on variational mode decomposition and multikernel support vector machine," *Shock and Vibration*, vol. 2016, Article ID 3196465, 11 pages, 2016.
- [24] Z. Li, Y. Jiang, Q. Guo, C. Hu, and Z. Peng, "Multi-dimensional variational mode decomposition for bearing-crack detection in wind turbines with large driving-speed variations," *Renewable Energy*, 2016.
- [25] N. Huang, H. Chen, G. Cai, L. Fang, and Y. Wang, "Mechanical fault diagnosis of high voltage circuit breakers based on variational mode decomposition and multi-layer classifier," *Sensors*, vol. 16, no. 11, article 1887, 2016.
- [26] Z. H. Wu and N. E. Huang, "Ensemble empirical mode decomposition: a noise-assisted data analysis method," *Advances in Adaptive Data Analysis*, vol. 1, no. 1, pp. 1–41, 2009.

## Research Article

# Fault Feature Extraction and Diagnosis of Gearbox Based on EEMD and Deep Briefs Network

**Kai Chen,<sup>1,2</sup> Xin-Cong Zhou,<sup>1,2</sup> Jun-Qiang Fang,<sup>1,2</sup> Peng-fei Zheng,<sup>1,2</sup> and Jun Wang<sup>1,2</sup>**

<sup>1</sup>Key Laboratory of High Performance Ship Technology (Wuhan University of Technology), Ministry of Education, Wuhan 430063, China

<sup>2</sup>Reliability Engineering Institute, School of Energy and Power Engineering, Wuhan University of Technology, Wuhan 430063, China

Correspondence should be addressed to Kai Chen; [kaichen@whut.edu.cn](mailto:kaichen@whut.edu.cn)

Received 30 December 2016; Revised 14 March 2017; Accepted 29 March 2017; Published 11 June 2017

Academic Editor: Tonghai Wu

Copyright © 2017 Kai Chen et al. This is an open access article distributed under the Creative Commons Attribution License, which permits unrestricted use, distribution, and reproduction in any medium, provided the original work is properly cited.

A gear transmission system is a complex nonstationary and nonlinear time-varying coupling system. When faults occur on gear system, it is difficult to extract the fault feature. In this paper, a novel fault diagnosis method based on ensemble empirical mode decomposition (EEMD) and Deep Briefs Network (DBN) is proposed to treat the vibration signals measured from gearbox. The original data is decomposed into a set of intrinsic mode functions (IMFs) using EEMD, and then main IMFs were chosen for reconstructed signal to suppress abnormal interference from noise. The reconstructed signals were regarded as input of DBN to identify gearbox working states and fault types. To verify the effectiveness of the EEMD-DBN in detecting the faults, a series of gear fault simulate experiments at different states were carried out. Results showed that the proposed method which coupled EEMD and DBN can improve the accuracy of gear fault identification and it is capable of applying to fault diagnosis in practical application.

## 1. Introduction

Gearbox is an indispensable part in the modern industry, especially for lots of large equipment [1]. As a device of transmission power, it is often prone to failure because of its complex structure and the poor working conditions. Failure of the gearbox not only leads to shutting down or threatening personal safety but also causes considerable economic losses. Therefore, it is very important for engineers and researchers to monitor the gear conditions to prevent this kind of malfunction of the plants.

The internal structure of the gearbox system is interrelated and coupled inside [2]. During the operation process, a lot of factors need to be considered when evaluating the performance status of the equipment, such as vibration, noise temperature, the debris contaminants in the oil and grease, torque of the power input and output, and stress distribution on the tooth surface. There are many methods for gearbox fault diagnosis, including vibration analysis [3], noise analysis [4], and oil analysis. Being online, real-time, and nondamage,

vibration signal analysis shows many advantages which make it widely used for gearbox fault diagnosis.

The most common signal processing methods include time-domain analysis and time-frequency analysis [5] such as amplitude spectrum analysis, order analysis [6], cepstrum analysis [7, 8], envelope spectrum analysis [6], Hilbert transform demodulation analysis [9], wavelet analysis, autocorrelation analysis [10], and empirical mode decomposition (EMD) [11]. Among the available vibration analysis methods, EMD is an effective signal analysis method which is suited for dealing with nonlinear and nonstationary signals [12]. It consists in local and fully data-driven separation of a signal in fast and slow oscillations. However, EMD experiences some problems, such as the presence of oscillations of very disparate amplitude in a mode or the presence of very similar oscillations in different modes, named as “mode mixing.” To overcome shortcomings, the ensemble empirical mode decomposition (EEMD) was proposed [13]. EEMD performs the EMD over an ensemble of the signal plus Gaussian white noise. Considering that vibration signals of the gearbox are

nonlinear and nonstationary, the EEMD algorithm is suitable for analyzing and judging the gearbox signals [14].

There are several failure modes in gear breakdown; some researchers utilized intelligent pattern recognition techniques in fault detection and diagnosis. SVM was used in machine condition monitoring and fault diagnosis [15]. RBF neural network is applied to improve the fault recognition rate in the fault diagnosis of gearbox [16]. Artificial neural network expert system was proposed to detect and localize defects in rolling element bearings [17]. However, the conventional neural network is of slow convergence speed and the possibilities of finding optimal solution are small, which have limited the neural network's application in the practical projects. But since the Deep Learning was introduced by Hinton et al. in 2006 [18], a new method in machine learning techniques started to be applied in visual data classification [19], decoding analysis [20], language information retrieval [21], and classifying the faults [22]. Especially in 2016, AlphaGo, an outstanding product of the depth learning algorithm, defeated a famous chess player with the score of 4 : 1 [23]. Its excellent performance in the game revealed the power of the learning algorithm. Therefore, it is necessary to introduce such an advanced algorithm into the fault diagnosis of gearbox. In this paper, a new method coupled with EEMD and DBN will be presented to diagnose the gear fault.

## 2. Description of Fault Diagnosis Method

**2.1. EEMD Algorithm.** EMD is a time-frequency signal analysis method of nonlinear signals, which can decompose the data adaptively and obtain a series of IMFs [24]. These IMFs reflect the characteristics of the signal itself and are distributed from high frequency to low frequency. EMD algorithm is very suitable for analyzing the vibration signal of gearbox, because the vibration signal of gearbox is nonstationary.

However, in practical application, it is found that there is a problem of mode mixing in the EMD decomposition process [13]; that is, a single IMF contains different frequency components or the same frequency components are decomposed into different IMFs.

To alleviate the mode mixing problem occurring in EMD, an ensemble empirical mode decomposition (EEMD) is presented [25]. The essential of EEMD algorithm is to decompose the original signal which adds Gaussian noise by using the EMD method repeatedly, and the original vibration data is decomposed into a series of IMFs with different scales and continuous characteristics because of the characteristic of frequency uniform distribution of Gaussian white noise, which can suppress the appearance of modal mixing.

The EEMD algorithm can be summarized as follows:

(1) Adding a white noise  $N(t)$  to the original signal  $x(t)$  can get a new signal  $X(t)$ :

$$X(t) = x(t) + N(t). \quad (1)$$

(2) The signal  $X(t)$  is decomposed by EMD to obtain a set of IMFs:

$$X(t) = \sum_{j=1}^n c_j(t) + r_n(t). \quad (2)$$

(3) Repeat steps (1) and (2)  $m$  times; get  $m$  groups of IMF by adding different amplitude of white noise  $N_i(t)$ ,  $i = 1 \sim m$ :

$$X_i(t) = x(t) + N_i(t)$$

$$X_i(t) = \sum_{j=1}^n c_{ij}(t) + r_{in}(t). \quad (3)$$

(4) Preserve the mean  $c_j(t)$  ( $i = 1, 2, \dots, m$ ) of each of the  $m$  IMFs as the final IMFs:

$$c_j(t) = \frac{1}{m} \sum_{i=1}^m c_{ij}(t). \quad (4)$$

To verify the validity of EEMD, a simulated signal as shown in formula (5) is decomposed by using EMD and EEMD, respectively; the simulated signal and decomposition results are shown in Figure 1.

$$y_1 = \sin(2\pi 30t)$$

$$y_2 = \sin(2\pi 10t) \quad (t > 0.2)$$

$$y_3 = \sin(2\pi 50t) \quad (t < 0.2)$$

$$y = y_1 + y_2 + y_3. \quad (5)$$

It can be seen from Figure 1 that EEMD can solve the mode mixing phenomenon which is better than EMD. Moreover, IMF2, IMF3, and IMF4 decomposed by EEMD are basically the same as the three components in the original simulated signal.

### 2.2. Deep Belief Networks

**2.2.1. Architecture of Restricted Boltzmann Machine.** Restricted Boltzmann machine (RBM), a generated random neural network, was proposed by Hinton and Sejnowski in 1986 [26]. There are two components in RBM: the visible layer ( $v$ ) (input layer) in the bottom and the hidden layer ( $h$ ) above. All visible units are connected to all hidden units, but there are no visible-visible or hidden-hidden connections. The weight between the visible layer and the hidden layer is denoted by  $W$ . The random variables of unit ( $v, h$ ) take values  $\in (0, 1)$ , and the joint probability distribution  $P(v, h)$  under the model follows Boltzmann distribution [27]. The architecture of RBM is shown in Figure 2.

The learning process is as follows: when inputting the visible layer  $v$ , the hidden layer  $h$  is obtained by  $p(h | v)$ , and vice versa. In other words, the visible layer is determined by  $p(h | v)$  and the hidden layer. Then the parameter is adjusted until difference between the visible layer and derived visible layer is minimized. It means that the hidden layer obtained in the middle process is an alternative representation of the visible layer.

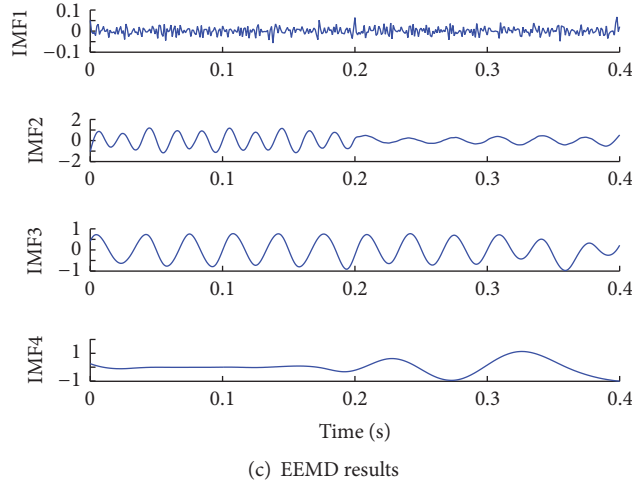
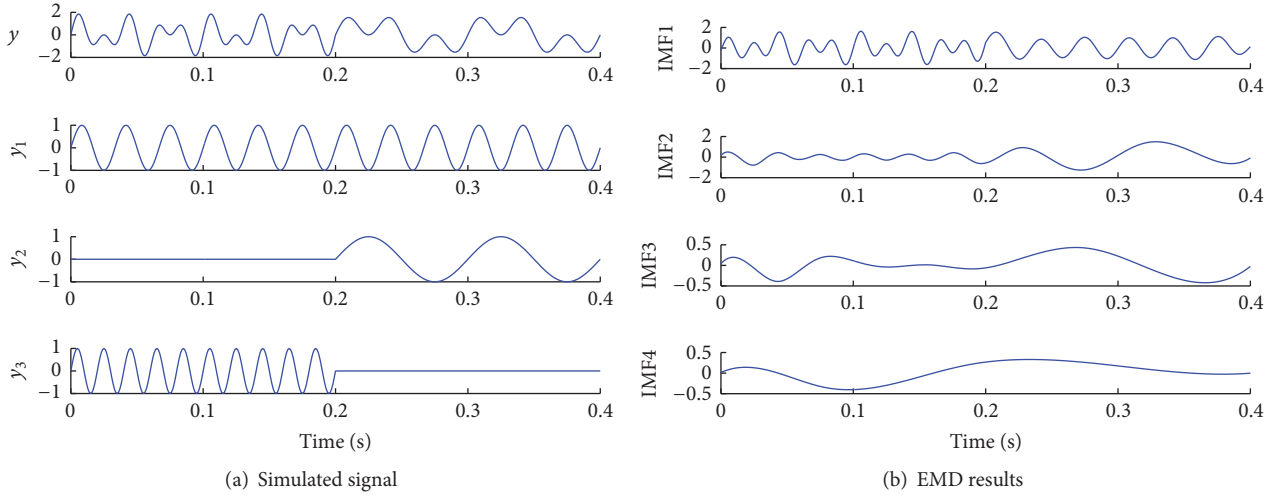


FIGURE 1: Comparison results of EMD and EEMD.

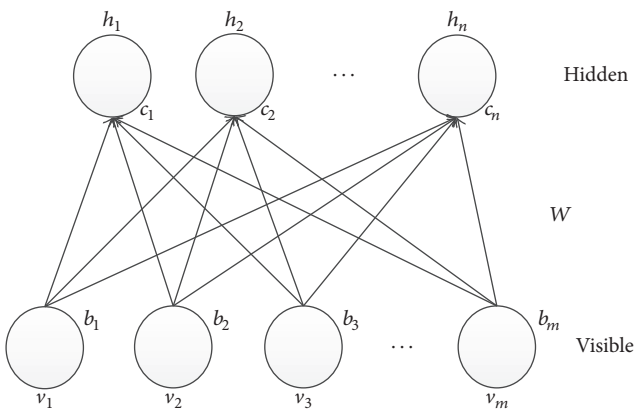


FIGURE 2: Architecture of restricted Boltzmann machine.

The derivation process of the RBM weight using contrastive divergence (CD) is described as follows [28]:

- (1) Randomly choose a set of data in training sample as input  $v^{(1)}$  (superscript denotes train time); determine

learning rate  $L$  and node number  $m$  of the hidden layer.

- (2) Randomly initialize  $W$ ,  $b$ , and  $c$ .
- (3) Update state of hidden variable according to formula (4):

$$P(h_j^{(k)} = 1 | v^{(k)}) = \frac{1}{1 + \exp(-\sum_i W_{ij} v_i^{(k)} - b_j)}, \quad (6)$$

where  $j = 1, 2, 3, \dots, m$  is the node number of the hidden layer.

- (4) Reconstitute  $v^{(k+1)}$  according to  $h^{(k)}$  and formula (5):

$$P(v_i^{(k+1)} = 1 | h^{(k)}) = \frac{1}{1 + \exp(-\sum_j W_{ij} h_j^{(k)} - c_i)}, \quad (7)$$

where  $i = 1, 2, 3, \dots, n$  is the node number of the input layer.

- (5) Then calculate  $h^{(k+1)}$  according to  $v^{(k+1)}$  and formula (4).

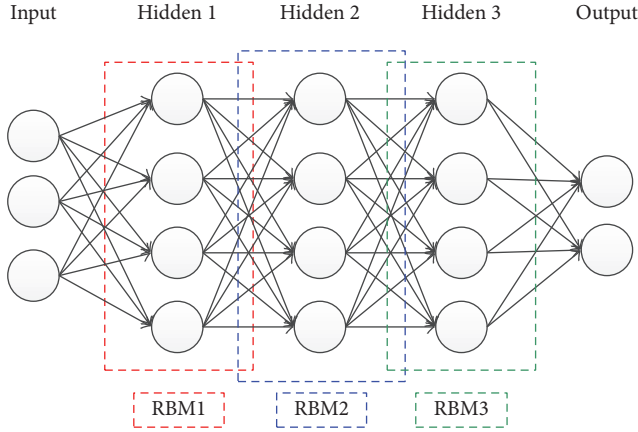


FIGURE 3: Deep belief network structure.

(6) Update weight and bias according to formula (6):

$$W = W + L \left( P(h_j^{(k)} = 1 | v^{(k)}) (v^{(k)})^T - P(h_j^{(k+1)} = 1 | v^{(k+1)}) (v^{(k+1)})^T \right) \quad (8)$$

$$c = c + L (v^{(k)} - v^{(k+1)})$$

$$b = b + L (P(h_j^{(k)} = 1 | v^{(k)}) - P(h_j^{(k+1)} = 1 | v^{(k+1)})).$$

(7) Iterate steps (4), (5), and (6)  $K$  times; fulfill parameter update of RBM.

**2.2.2. Deep Belief Networks.** A DBN is formed by stacking a number of the RBMs layer by layer as shown in Figure 3. Each layer of the RBM is independent, and the layers are interconnected by weight. Deep belief network structure is shown in Figure 3.

A usable DBN network model can be obtained via pretraining and fine-tuning. Note that this learning procedure, so-called pretraining, is unsupervised. The training procedure is described as follows [29]:

- (1) Each RBM layer is trained individually, insuring that the output of each layer contains input features as much as possible. The training process is as follows: the input data is mapped to the output data by weight; then the output data try to reconstruct the input data. The weight of the network is updated according to the difference after reconstruction. Repeat this process until the difference between input data and output data is very small; this is the RBM learning process presented in the previous section.
- (2) In the previous step, the training only optimizes the mappings between the input layer and the output layer rather than the entire DBN. Therefore, it is necessary to set the last DBN layer as softmax classifier. The output feature vector of RBM is input feature vector of softmax classifier and it is trained under

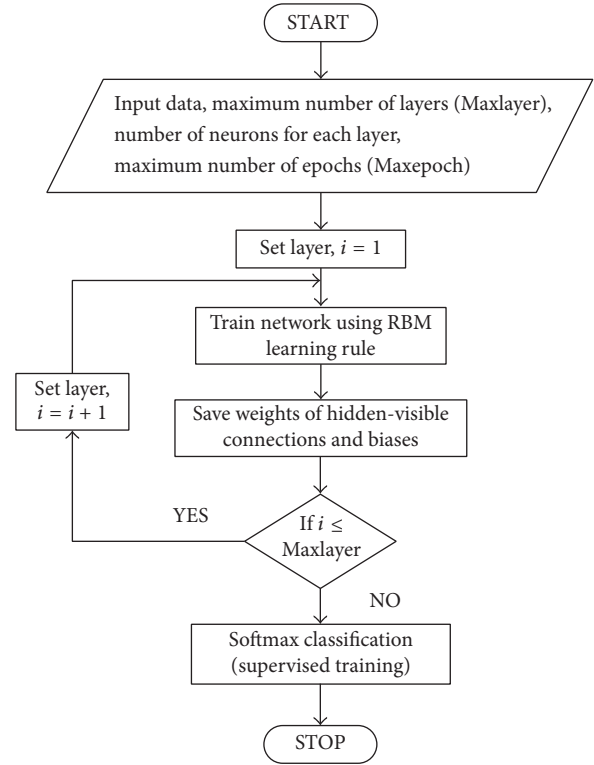


FIGURE 4: Flowchart of the DBN training process.

monitoring. All parameters of the network are fine-tuned according to the error of output and input to each RBM layer spreading from top to bottom. The process is illuminated as a flowchart in Figure 4.

### 3. Experimental Setup and Fault Data

**3.1. Experimental Setup.** To evaluate the performance of the fault diagnosis method, experimental analysis of a gear transmission has been carried out in an experimental setup. As shown in Figure 5, the experimental setup is composed of electrical motor, timing belt pulley, coupling, gearbox, and magnetic powder brake. An electrical motor with frequency converter, whose speed is up to 1,500 r/min, is the drive. The number of teeth of the input gear is 55, while that of the output gear is 75; thus the speed ratio is 55/75. A magnetic powder brake is used as the external load. The sensors are the piezoelectric accelerometers (CA-YD-186).

The amplitude of the vibration signal is attenuated during transmission, and the amplitude attenuation of the high frequency component is much faster than the low frequency component. The location near the bearing, in which attenuation and distortion of the vibration signal were minimum, is the best sensor measuring point. In the experiments, the acceleration sensor is used to measure the vibration signal of the gearbox. And the sensor was arranged in the gearbox near each bearing seat on vertical direction, which is closer to the bearing than the horizontal direction in this experimental setup. The sensor measuring point was shown in Figure 5.

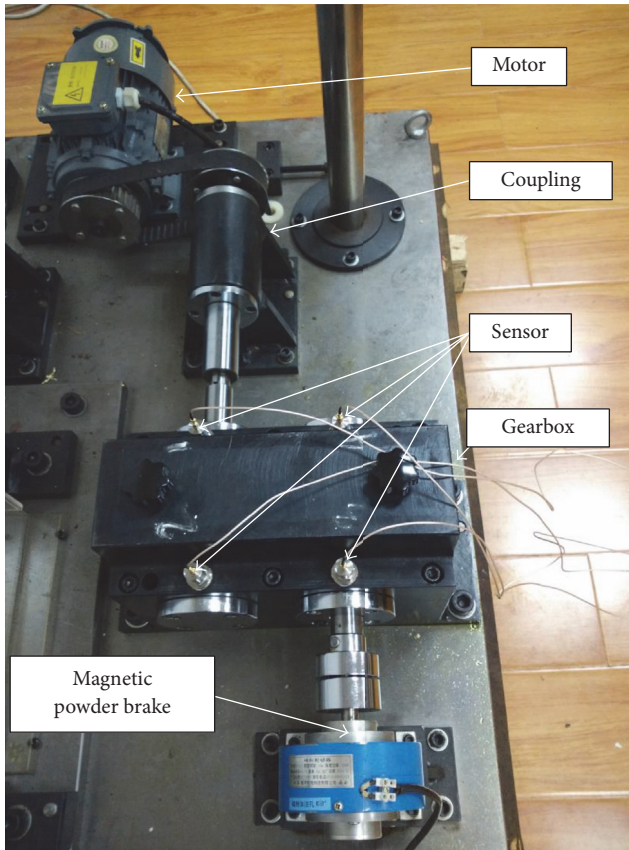


FIGURE 5: Experimental setup and sensor arranged.

**3.2. Fault Data Collection.** In order to collect fault data of gear fault type, a series of gears were processed to simulate common fault gears. As shown in Figure 6, three typical faults of gear were simulated, which are tooth breaking, root crack, and pitting corrosion.

Experiment was designed to collect the mass of data under various faults and work conditions, which involve four gear statuses (normal, break, wear, and pit), two types of motor speed (1500 r/min and 1200 r/min), and three kinds of load (0 A, 0.1 A, and 0.2 A). The sampling frequency is 10240 Hz. There are 131072 sampling points in each condition; then the data is divided into 64 parts, each of which is regarded as a sample with 2048 data points. Thus, 384 sets of data were generated in each gear status, and 64 sets of them were selected as test samples by random drawing, while the other 320 sets were chosen as training samples. In total, 1280 training samples and 256 test samples were extracted from the vibration data.

## 4. Application of Proposed Diagnosis Method

**4.1. EEMD-DBN Diagnosis Method.** The original vibration signals were decomposed into several IMFs components with EEMD method. The decomposed IMFs components represent the components of different frequencies in the original vibration signal. EEMD results in one sample of

TABLE 1: Parameters of DBN.

Network layer (including input layer)	4
Type of input data	Frequency domain
Length of the input data	1024
Node number of input layer	1024
Node number of RBM1	500
Node number of RBM2	100
Node number of output layer	4
Classifier of output layer	Softmax
Learning rate	0.1
Maximum iteration	100

the different fault signals are indicated in Figure 7. There are 11 IMFs components in each EEMD result, and each decomposed fault signal is shown from high frequency to low frequency.

In real working condition, the collected vibration signal generally contains the noise background, so the pseudocomponent influences the EEMD decomposition. The frequency components contained in these pseudocomponents have the possibility of coinciding with the IMF characteristic frequency band and they should be eliminated. The process of gearbox fault diagnosis based on EEMD noise reduction and DBN is illuminated in Figure 8.

As the natural frequency of the gear is high, the noise in the signal is decomposed into the low frequency band in EEMD. However, the information contains the gearbox working status and fault characteristics which are decomposed into high frequency. Therefore, the high frequency parts of EEMD results are what is mainly studied. Front 4th-order IMFs decomposed by original data were chosen to reconstitute signals. After EEMD noise reduction, DBN is used to classify the four states of the gearbox.

**4.2. DBN Training Results.** Theoretically, the length of the input data should be 2048 points, but the type of input data is the frequency domain of reconstituted signal, which was symmetry, so the first half was taken. This choice will not affect the classification results. Moreover, it can reduce the training time. Therefore, the size of the input data is 1024. The parameters of DBN are shown in Table 1.

A comparative analysis was carried out between coupled EEMD with DBN and DBN without EEMD to verify the availability of the coupled method.

To increase the separation among the feature clusters in order to gain more diagnostic accuracy and reduce the feature dimensionality for effective computation, the principle component analysis (PCA) is successively applied to the obtained feature sets. The distribution of the features in the new feature space can be observable through the visualization.

The first three principal components of first layer and second RBM layer are extracted, and the visual graphic is shown in Figures 9 and 10. Figure 9 is the result of DBN

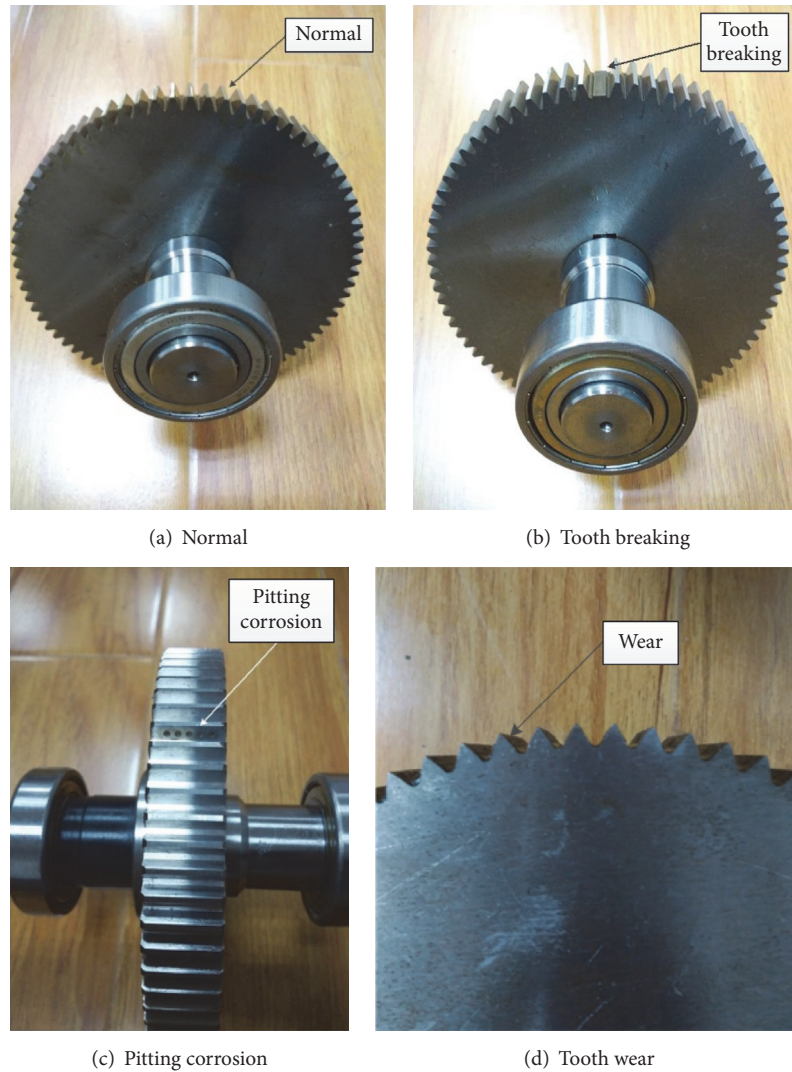


FIGURE 6: Simulation of gear fault type.

training without EEMD method, and Figure 10 is the result of DBN training with EEMD noise reduction.

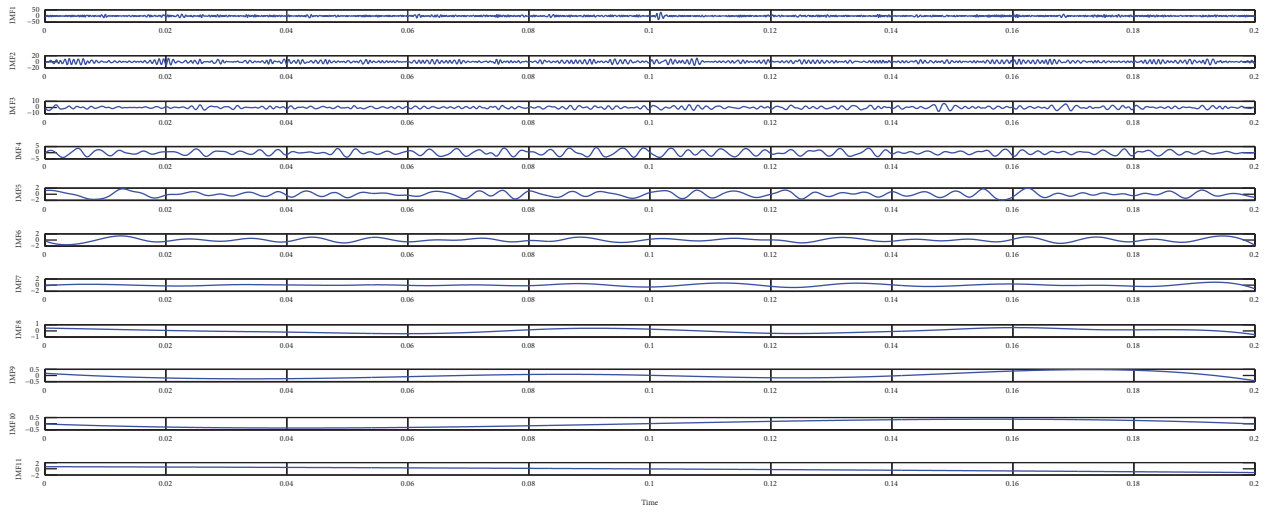
**4.3. DBN Test Results.** In order to estimate classification effect of the two training data samples on DBN, the data test was carried out. Test data was processed the same as the training data (if the training data is processed by EEMD, so is the test data; if the training data was unprocessed, so is the test data). The test of the DBN network was carried out 20 times, and the accuracy rate of each time is shown in Figure 11.

It can be observed from Figure 11 that the average recognition rate with EEMD processing is 99.25%, while the average recognition rate without processing is 96.25%. The recognition rate was enhanced almost 3% after EEMD processing. Moreover, recognition rate is more stable when the data is processed. It can be said that DBN methods effectively assist in improving the accuracy of gear fault diagnosis.

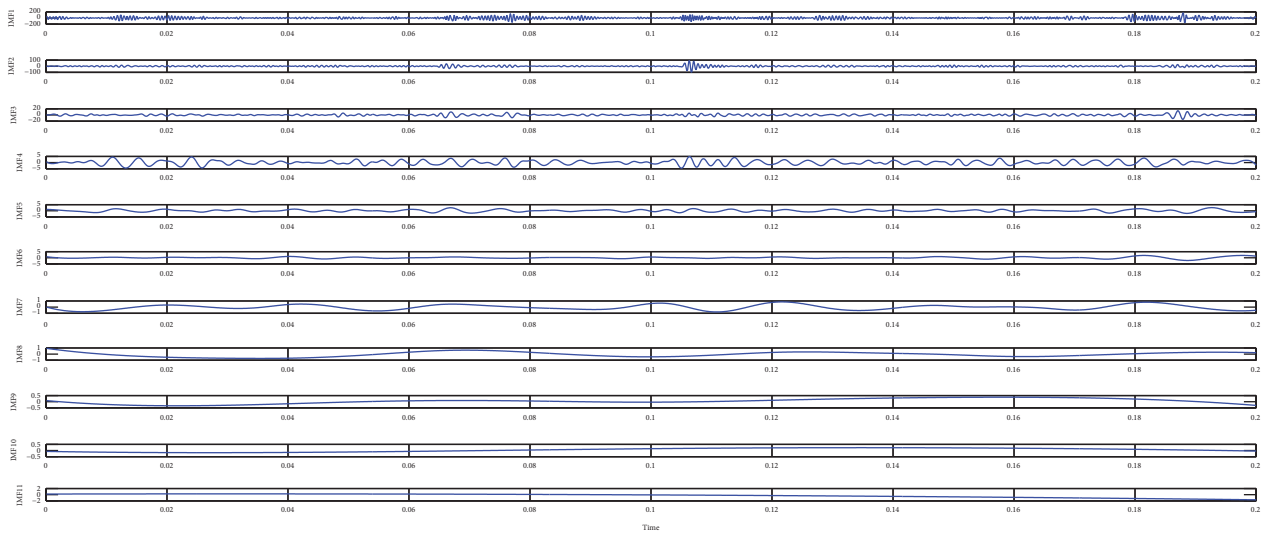
## 5. Conclusion

This paper has presented the new approach to diagnose gearbox fault using vibration signals. The original vibration signals were decomposed into several IMFs components with EEMD method. The decomposed IMFs components represent the different frequency components of the original vibration signal. To deal with the instabilities occurring in vibration signal, only main IMFs were chosen to reconstitute signals for eliminating noise effects in signal. The fault features were extracted by DBN training.

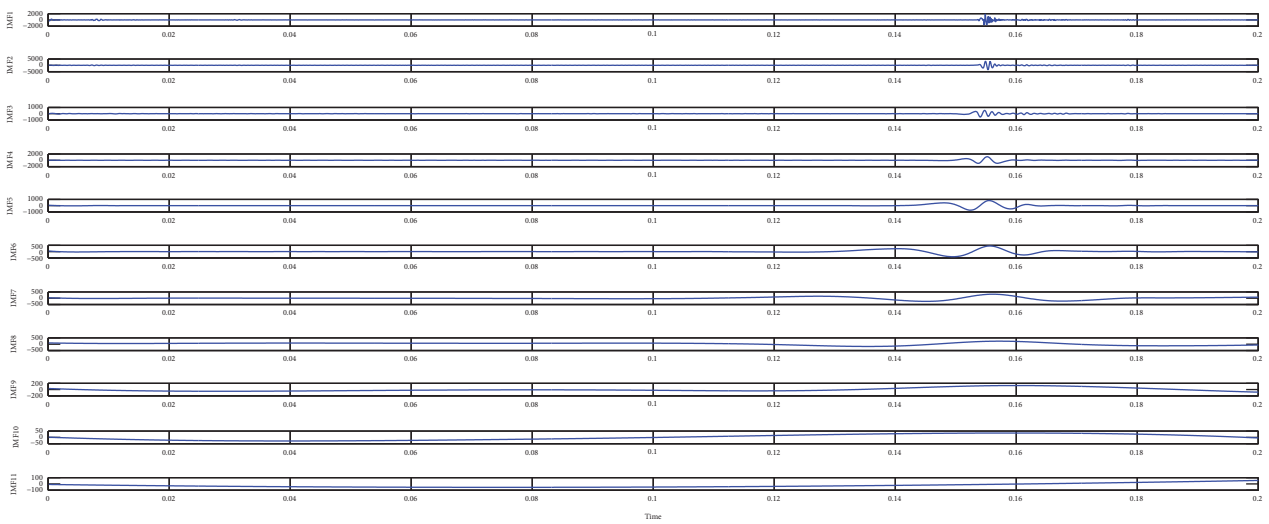
Finally, the features are inputted to DBN test, so that their performance is appraised. The results show that the proposed approach which coupled EEMD and DBN can improve the accuracy of gear fault identification and it is capable of applying to fault diagnosis in practical application.



(a) Normal

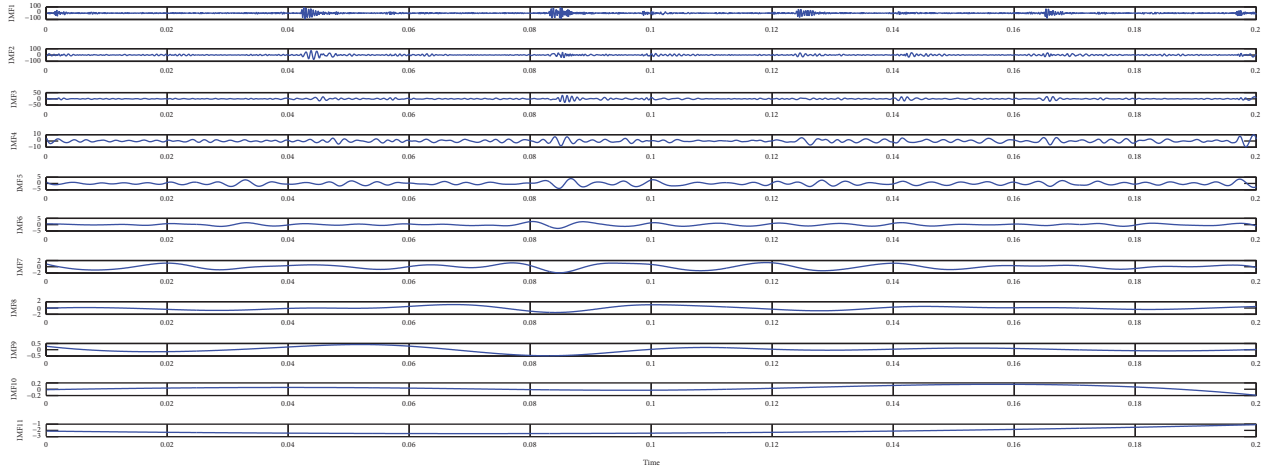


(b) Break



(c) Wear

FIGURE 7: Continued.



(d) Pit

FIGURE 7: EEMD results of fault signal.

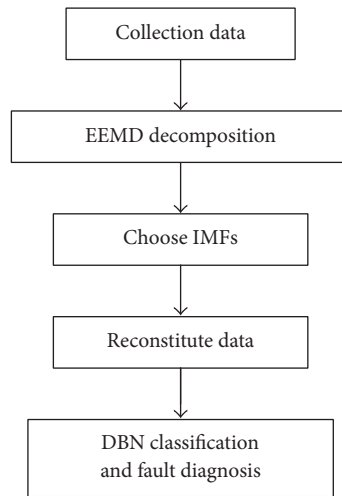


FIGURE 8: Procedure of fault diagnosis based on EEMD and DBN.

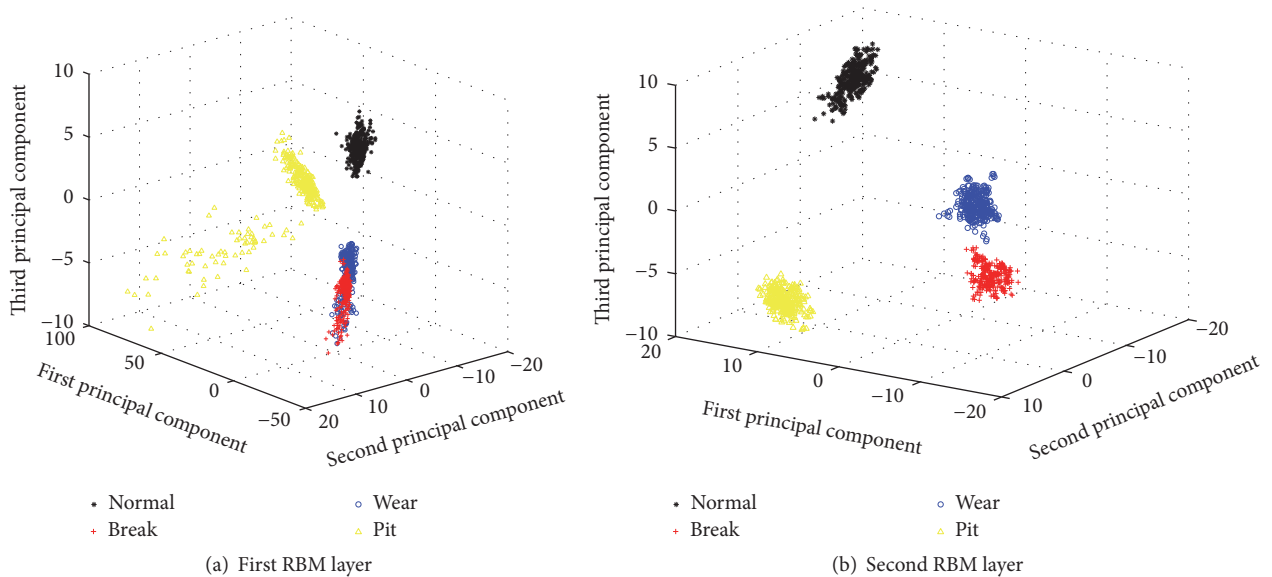


FIGURE 9: Features distribution of DBN result.

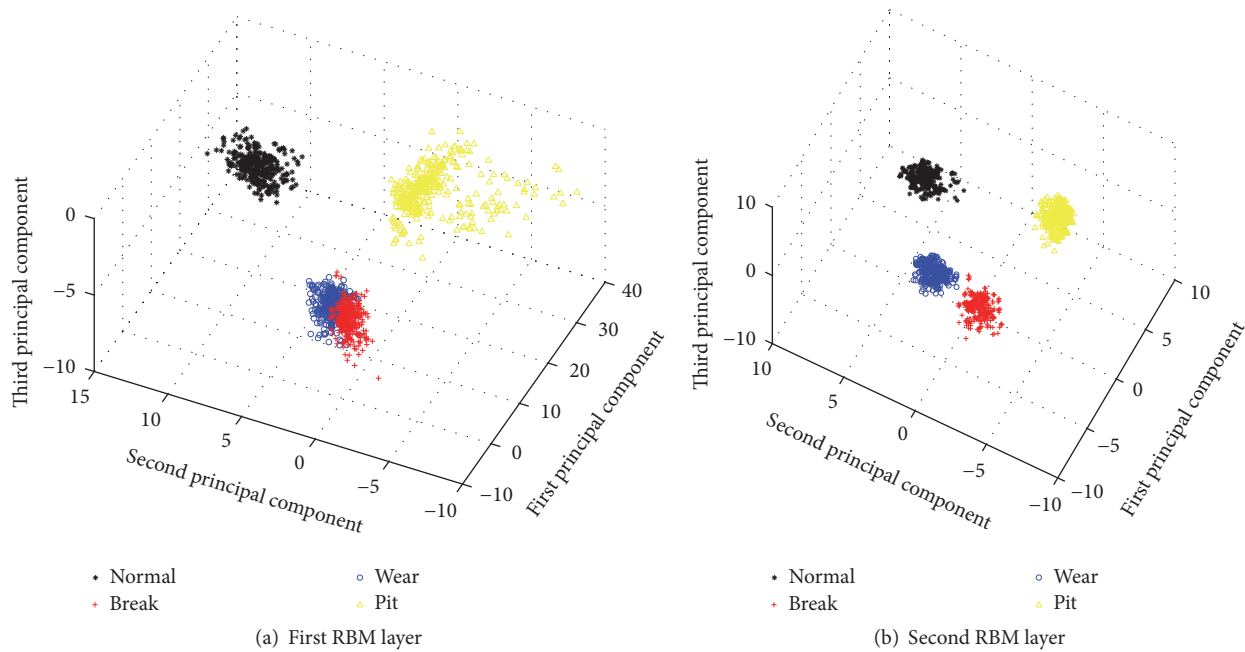


FIGURE 10: Features distribution of EEMD-DBN result.

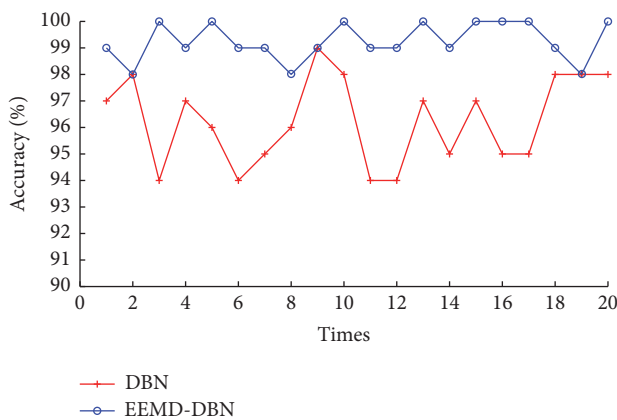


FIGURE 11: Accuracy of test result.

## Conflicts of Interest

The authors declare that there are no conflicts of interest regarding the publication of this paper.

## Acknowledgments

This project is sponsored by the grants from the Ministry of Transport Applied Basic Research Project (no. 2013329811360), the National Natural Science Foundation of China (no. 51139005 and no. 51509194), and the Fundamental Research Funds for the Central Universities (no. 2014-yb-018).

## References

- [1] Z. Li, X. Yan, C. Yuan, J. Zhao, and Z. Peng, "Fault detection and diagnosis of a gearbox in marine propulsion systems using bispectrum analysis and artificial neural networks," *Journal of Marine Science and Application*, vol. 10, no. 1, pp. 17–24, 2011.
- [2] Z. Li, X. Yan, Z. Tian, C. Yuan, Z. Peng, and L. Li, "Blind vibration component separation and nonlinear feature extraction applied to the nonstationary vibration signals for the gearbox multi-fault diagnosis," *Measurement Journal of the International Measurement Confederation*, vol. 46, no. 1, pp. 259–271, 2013.
- [3] B. Chen, Z. Zhang, C. Sun, B. Li, Y. Zi, and Z. He, "Fault feature extraction of gearbox by using overcomplete rational dilation discrete wavelet transform on signals measured from vibration sensors," *Mechanical Systems and Signal Processing*, vol. 33, pp. 275–298, 2012.
- [4] Ş. Ulus and S. Erkaya, "An experimental study on gear diagnosis by using acoustic emission technique," *International Journal of Acoustics and Vibrations*, vol. 21, no. 1, pp. 103–111, 2016.
- [5] Z. Li, Y. Jiang, C. Hu, and Z. Peng, "Recent progress on decoupling diagnosis of hybrid failures in gear transmission systems using vibration sensor signal: a review," *Measurement*, vol. 90, pp. 4–19, 2016.
- [6] J. Cheng, Y. Yang, and D. Yu, "The envelope order spectrum based on generalized demodulation time–frequency analysis and its application to gear fault diagnosis," *Mechanical Systems & Signal Processing*, vol. 24, no. 2, pp. 508–521, 2010.
- [7] H. Li and Zheng, "Gear fault diagnosis based on order cepstrum analysis," *Journal of Vibration & Shock*, vol. 25, no. 5, pp. 65–68, 2006.
- [8] L. Nacib, K.-M. Pekpe, and S. Sakhara, "Detecting gear tooth cracks using cepstral analysis in gearbox of helicopters," *International Journal of Advances in Engineering & Technology*, 2013.
- [9] A. Djebala, N. Ouelaa, C. Benchaabane, and D. F. Laefer, "Application of the Wavelet Multi-resolution Analysis and Hilbert transform for the prediction of gear tooth defects," *Meccanica*, vol. 47, no. 7, pp. 1601–1612, 2012.

- [10] M.-E. Morsy and G. Achtenova, "Value of autocorrelation analysis in vehicle gearbox fault diagnosis," *International Journal of Vehicle Noise & Vibration*, vol. 11, no. 2, pp. 181–193, 2015.
- [11] Y. Li, Z. Han, J. Gao, and S. Ning, "Application of EMD in gear fault diagnosis based on autocorrelation analysis," *Journal of Chinese Agricultural Mechanization*, 2015.
- [12] J. Cheng, D. Yu, and Y. Yang, "Fault diagnosis for rotor system based on EMD and fractal dimension," *China Mechanical Engineering*, 2005.
- [13] N. E. Huang, M. C. Wu, S. R. Long et al., "A confidence limit for the empirical mode decomposition and Hilbert spectral analysis," *The Royal Society of London. Proceedings. Series A. Mathematical, Physical and Engineering Sciences*, vol. 459, no. 2037, pp. 2317–2345, 2003.
- [14] M. E. Torres, M. A. Colominas, G. Schlotthauer, and P. Flandrin, "A complete ensemble empirical mode decomposition with adaptive noise," in *Proceedings of the 36th IEEE International Conference on Acoustics, Speech, and Signal Processing*, pp. 4144–4147, Prague, Czech Republic, May 2011.
- [15] A. Widodo and B.-S. Yang, "Support vector machine in machine condition monitoring and fault diagnosis," *Mechanical Systems & Signal Processing*, vol. 21, no. 6, pp. 2560–2574, 2007.
- [16] J. Leng, S. Jing, and Z. Wu, "Fault diagnosis for gearbox based on RBF neural network," *Journal of Mechanical Strength*, 2010.
- [17] P. Jayaswal, S.-N. Verma, and A.-K. Wadhvani, "Development of EBP-Artificial neural network expert system for rolling element bearing fault diagnosis," *Journal of Vibration & Control*, vol. 17, no. 8, pp. 1131–1148, 2011.
- [18] G. E. Hinton, S. Osindero, and Y.-W. Teh, "A fast learning algorithm for deep belief nets," *Neural Computation*, vol. 18, no. 7, pp. 1527–1554, 2006.
- [19] Y. Liu, S. Zhou, and Q. Chen, "Discriminative deep belief networks for visual data classification," *Pattern Recognition*, vol. 44, no. 10–11, pp. 2287–2296, 2011.
- [20] Y. Hatakeyama, H. Kataoka, Y. Okuhara, and S. Yoshida, "Decoding analysis for fMRI based on Deep Brief Network," in *2014 World Automation Congress, WAC 2014*, pp. 268–272, usa, August 2014.
- [21] J. Kim, J. Nam, and I. Gurevych, "Learning semantics with deep belief network for Cross-Language information retrieval," in *International Conference on Computational Linguistics*, pp. 579–588.
- [22] P. Tamilselvan and P. Wang, "Failure diagnosis using deep belief learning based health state classification," *Reliability Engineering & System Safety*, vol. 115, no. 7, pp. 124–135, 2013.
- [23] F.-Y. Wang, J. J. Zhang, X. Zheng et al., "Where does AlphaGo go: From church-turing thesis to AlphaGo thesis and beyond," *IEEE/CAA Journal of Automatica Sinica*, vol. 3, no. 2, pp. 113–120, 2016.
- [24] Y. Lei, Z. He, and Y. Zi, "Application of the EEMD method to rotor fault diagnosis of rotating machinery," *Mechanical Systems & Signal Processing*, vol. 23, no. 4, pp. 1327–1338, 2009.
- [25] X. Wang, C. Liu, F. Bi, X. Bi, and K. Shao, "Fault diagnosis of diesel engine based on adaptive wavelet packets and EEMD-fractal dimension," *Mechanical Systems & Signal Processing*, vol. 41, no. 1, pp. 581–597, 2013.
- [26] G.-E. Hinton and T.-J. Sejnowski, "Learning and relearning in Boltzmann machines," pp. 282–317, 1986.
- [27] R. Salakhutdinov, A. Mnih, and G. Hinton, "Restricted Boltzmann machines for collaborative filtering," in *Proceedings of the 24th International Conference on Machine Learning (ICML '07)*, vol. 227, pp. 791–798, Corvallis, Oregon, June 2007.
- [28] A. Fischer and C. Igel, *An Introduction to Restricted Boltzmann Machines*, Springer Berlin Heidelberg, 2012.
- [29] G. Hinton, *Deep Belief Nets*, Springer US, 2011.

## Research Article

# Stator and Rotor Faults Diagnosis of Squirrel Cage Motor Based on Fundamental Component Extraction Method

Guoqing An<sup>1,2</sup> and Hongru Li<sup>1</sup>

<sup>1</sup>Mechanical Engineering College, Shijiazhuang 050003, China

<sup>2</sup>Hebei University of Science and Technology, Shijiazhuang 050018, China

Correspondence should be addressed to Hongru Li; lihrl68@sohu.com

Received 19 February 2017; Accepted 13 April 2017; Published 8 May 2017

Academic Editor: Zhixiong Li

Copyright © 2017 Guoqing An and Hongru Li. This is an open access article distributed under the Creative Commons Attribution License, which permits unrestricted use, distribution, and reproduction in any medium, provided the original work is properly cited.

Nowadays, stator current analysis used for detecting the incipient fault in squirrel cage motor has received much attention. However, in the case of interturn short circuit in stator, the traditional symmetrical component method has lost the precondition due to the harmonics and noise; the negative sequence component (NSC) is hard to be obtained accurately. For broken rotor bars, the new added fault feature blanked by fundamental component is also difficult to be discriminated in the current spectrum. To solve the above problems, a fundamental component extraction (FCE) method is proposed in this paper. On one hand, via the antisynchronous speed coordinate (ASC) transformation, NSC of extracted signals is transformed into the DC value. The amplitude of synthetic vector of NSC is used to evaluate the severity of stator fault. On the other hand, the extracted fundamental component can be filtered out to make the rotor fault feature emerge from the stator current spectrum. Experiment results indicate that this method is feasible and effective in both interturn short circuit and broken rotor bars fault diagnosis. Furthermore, only stator currents and voltage frequency are needed to be recorded, and this method is easy to implement.

## 1. Introduction

Nowadays, squirrel cage motor has been widely used in the industrial and agricultural production because of its simple and rugged construction [1]. But it is usually subjected to the unavoidable stresses, which create failures in different parts. Statistical studies have shown that interturn short circuit fault in stator accounts for nearly 30%–40% of total failures; the broken rotor bars fault takes nearly 10% [2–4]. Traditional noninvasive techniques are usually used to diagnose these types of fault. These strategies are based on the analysis of quantities such as vibration, voltage, current, torque, and speed [5]. With the development of modern signal processing and computer technology, some advanced diagnosis methods have been proposed recently.

In the case of interturn short circuit in stator, the traditional symmetrical component method has lost the precondition because of the harmonics and noise [6–8]. The NSC as fault characteristic is hard to be obtained accurately. Reference [9] took stator negative sequence impedance

as interturn short circuit fault characteristic; this method has robustness in the case of unbalanced power supply, because negative sequence impedance is the ratios of negative sequence voltage and current. But if the power supply is balanced enough, the calculation results will include error. Reference [10] extracted the vibration feature to diagnose the winding fault; unfortunately it cannot distinguish rotor partiality with the stator fault. Reference [11] utilized neural network to detect the turns of short circuit in the winding, but it usually requires a large amount of data for training. If the data is overtrained or inadequately trained, the diagnosis result would be influenced. By analyzing the changes of higher harmonics in the residual voltage after AC dump, the location of interturn short circuit in the stator winding can be found, but it is very hard to achieve the on-line fault diagnosis [12]. Reference [13] utilized the instantaneous power decomposition technique to improve the precision of the fault recognition under different operating conditions, but there are a lot of parameters needed to be identified.

In the case of broken rotor bars, the presence of fault will provoke air-gap field perturbation in the stator current spectrum, and two sideband components appear in the vicinity of supply frequency, with frequencies given as follows [14]:

$$f_s = f(1 \pm 2s), \quad (1)$$

where  $f_s$  represents fault frequency,  $f$  represents supply frequency, and  $s$  represents slip of squirrel cage motor.

However, the spectral leakage of the fundamental component obscures the rotor fault components. It can get worse when squirrel cage motor is operated at low slip values, because the components  $f_s$  become closer. In order to solve the problem, [15, 16] proposed extended Park's vector approach, and [17] proposed Hilbert modulus spectrum analysis to extract the broken bars fault feature. But the above two methods would produce some other crossed components, which make the spectrum be more complicated. Reference [18] utilized Hilbert transform to detect the broken rotor bar fault location through envelope analysis of start-up current, but it is very hard to achieve the on-line fault diagnosis. Reference [19] presented a Park vector rotating filter; the fundamental component can be removed accurately. But the algorithm needs to filter out NSC firstly, and the complicated calculation limits the application. Reference [20] utilized higher-order spectrum to detect the rotor fault, but the problem of large amount of computation needs to be solved firstly.

FCE method based on correlation analysis of current signal is proposed in this paper. In the case of interturn short circuit in stator, the method is used to avoid the effects of the harmonics and noise in current signal firstly. Then, via ASC transformation, the NSC of extracted signals is transformed into the DC value, and the amplitude of a synthetic vector of the NSC is given to evaluate the severity of stator fault. In the case of broken rotor bars, the extracted fundamental component can be filtered out accurately according to the results of FCE method, and the rotor fault components may emerge from the stator current spectrum.

The paper is organized as follows: Section 2 presents FCE method, and the implementation of this method is introduced in both cases of interturn short circuit and broken rotor bars fault diagnosis. Section 3 presents the structure frame of fault diagnosis system. Section 4 presents a favorable discussion and analysis of the experimental results. Finally, our conclusions are provided in Section 5.

## 2. Algorithm of FCE

**2.1. FCE Method.** Correlation function describes the relationship between one instantaneous value  $x(t)$  and another one  $x(t + \tau)$ . The self-correlation and cross-correlation functions are defined as the follows:

$$\begin{aligned} R_x(\tau) &= E[x(t)x(t + \tau)] \\ &= \lim_{T \rightarrow \infty} \frac{1}{T} \int_0^T x(t)x(t + \tau) dt, \end{aligned}$$

$$\begin{aligned} R_{xy}(\tau) &= E[x(t)y(t + \tau)] \\ &= \lim_{T \rightarrow \infty} \frac{1}{T} \int_0^T x(t)y(t + \tau) dt, \end{aligned} \quad (2)$$

where  $T$  represents signal period and  $\tau$  represents time difference.

Now there are two signals expressed as

$$\begin{aligned} x(t) &= A_x \sin(\omega t + \theta), \\ y(t) &= A_y \sin(\omega t + \theta - \varphi_{xy}), \end{aligned} \quad (3)$$

where  $A_x$  and  $A_y$  represent amplitude,  $\omega$  represents radian frequency,  $\theta$  represents phase angle, and  $\varphi_{xy}$  represents phase difference.

Because  $T$  is finite, the estimate of cross-correlation between  $x(t)$  and  $y(t)$  can be described as follows:

$$\begin{aligned} \hat{R}_{xy}(\tau) &= \frac{1}{T} \\ &\cdot \int_0^T A_x \sin(\omega t + \theta) A_y \sin(\omega(t + \tau) + \theta - \varphi_{xy}) dt \\ &= \frac{1}{2} A_x A_y \cos(\omega\tau - \varphi_{xy}). \end{aligned} \quad (4)$$

In (4), it can be concluded that the frequency information and phase information are both reserved.

Now a sinusoidal signal containing noise is given as follows:

$$s(t) = A \sin(\omega t + \varphi) + n(t), \quad (5)$$

where  $A$  represents amplitude of sinusoidal component,  $\varphi$  represents phase angle, and  $n(t)$  indicates noise.

Then two reference signals which have the same frequency with  $s(t)$  can be constructed:

$$\begin{aligned} z_1(t) &= B \sin(\omega t), \\ z_2(t) &= B \cos(\omega t), \end{aligned} \quad (6)$$

where  $B$  represents amplitude of the reference signals.

There is no correlation of  $n(t)$  with  $z_1(t)$  and  $z_2(t)$ , so the estimate of cross-correlation between  $s(t)$  and  $z_1(t)$  and  $z_2(t)$  can be described as follows:

$$\begin{aligned} R_{sz1} &= \frac{1}{T} \int_0^T s(t) z_1(t) dt = \frac{1}{2} AB \cos(\varphi), \\ R_{sz2} &= \frac{1}{T} \int_0^T s(t) z_2(t) dt = \frac{1}{2} AB \sin(\varphi). \end{aligned} \quad (7)$$

By (7), the phase angle and amplitude can be expressed as follows:

$$\begin{aligned} \varphi &= \text{arctg}\left(\frac{R_{sz2}}{R_{sz1}}\right), \\ A &= \frac{2R_{sz1}}{B \cos(\varphi)}. \end{aligned} \quad (8)$$

In this way, the fundamental component can be extracted from stator current accurately.

**2.2. Application of FCE Method in Stator Short Circuit Fault Diagnosis.** Stator interturn short circuit fault would cause the imbalance of three-phase current. Due to harmonics and noise in stator current, the traditional symmetrical component method has lost the precondition; the NSC is hard to be obtained accurately. Therefore, FCE method can be applied in the stator fault diagnosis.

In the remainder of this paper, phase A will be taken as the example for discussion. It is assumed that phase current signal is recorded as  $N$  points in period  $T$ . The discrete-time array of current is named as  $i_A(t_k)$ . According to (6), the arrays corresponding to reference signals are noted as  $z_1(t_k)$  and  $z_2(t_k)$ , respectively, where  $t_k = 0, 1, 2, \dots, N-1$ . The estimate of cross-correlation  $R_{Iz1}$  and  $R_{Iz2}$  between  $i_A(t_k)$  and  $z_1(t_k)$  and  $z_2(t_k)$  can be expressed as follows:

$$\begin{aligned} R_{Iz1} &= \frac{1}{N} \sum_{t_k=0}^{N-1} i_A(t_k) z_1(t_k), \\ R_{Iz2} &= \frac{1}{N} \sum_{t_k=0}^{N-1} i_A(t_k) z_2(t_k). \end{aligned} \quad (9)$$

By (8), it is easy to obtain the amplitude and phase of fundamental component in the stator phase current. The

same method can be used to calculate the values of phases B and C. Then fundamental component of three-phase current can be expressed as follows:

$$\begin{bmatrix} i_{A1}(t_k) \\ i_{B1}(t_k) \\ i_{C1}(t_k) \end{bmatrix} = \begin{bmatrix} I_{A1M} \cos(\omega t_k + \varphi_{A1}) \\ I_{B1M} \cos(\omega t_k + \varphi_{B1}) \\ I_{C1M} \cos(\omega t_k + \varphi_{C1}) \end{bmatrix}, \quad (10)$$

where  $I_{A1M}$ ,  $I_{B1M}$ , and  $I_{C1M}$  represent the amplitudes of fundamental component and  $\varphi_{A1}$ ,  $\varphi_{B1}$ , and  $\varphi_{C1}$  represent the phase angles of fundamental component.

Since the extraction of DC component is much easier in signal processing, a method based on ASC transformation is applied for NSC calculation. In this coordinate, the positive sequence component is turned into the second harmonic, and NSC is transformed into the DC component, which can be extracted by the mean algorithm. Then the extracted DC component can be used to evaluate the severity of the interturn short circuit fault in the stator. The matrix from three-phase coordinate  $(a, b, c)$  to the ASC  $(d, q)$  is given by

$$C_{N3 \rightarrow 2} = \sqrt{\frac{2}{3}} \begin{bmatrix} \cos(\omega_1 t + \theta_0) & \cos\left(\omega_1 t + \theta_0 + \frac{2}{3}\pi\right) & \cos\left(\omega_1 t + \theta_0 - \frac{2}{3}\pi\right) \\ -\sin(\omega_1 t + \theta_0) & -\sin\left(\omega_1 t + \theta_0 + \frac{2}{3}\pi\right) & -\sin\left(\omega_1 t + \theta_0 - \frac{2}{3}\pi\right) \\ \frac{1}{\sqrt{2}} & \frac{1}{\sqrt{2}} & \frac{1}{\sqrt{2}} \end{bmatrix}, \quad (11)$$

where  $\omega_1$  represents radian frequency of stator voltage,  $\theta_0$  represents initial angle between  $a$ -axis in stationary coordinate and  $d$ -axis in rotating coordinate. In the ASC, the fundamental component can be expressed as follows:

$$\begin{aligned} & [i_d(t_k) \quad i_q(t_k) \quad i_0(t_k)]^T \\ & = C_{N3 \rightarrow 2} [i_{A1}(t_k) \quad i_{B1}(t_k) \quad i_{C1}(t_k)]^T, \end{aligned} \quad (12)$$

where the  $d$ -axis component is noted as  $i_d(t_k)$ ,  $q$ -axis component is noted as  $i_q(t_k)$ , and zero sequence component is noted as  $i_0(t_k)$ .

Adjust the sampling time to be integer multiple of the supply power period. Via the mean algorithm, the NSC which has been turned into DC one can be extracted. Meanwhile the positive sequence component which has been turned into the second harmonic can be filtered out. Zero sequence component  $i_0$  is small enough to be ignored:

$$\begin{aligned} I_{-d} &= \frac{1}{N} \sum_{t_k=0}^{N-1} i_d(t_k), \\ I_{-q} &= \frac{1}{N} \sum_{t_k=0}^{N-1} i_q(t_k), \end{aligned} \quad (13)$$

where  $I_{-d}$  represents the value of NSC projected on  $d$ -axis and  $I_{-q}$  represents the one projected on  $q$ -axis in the ASC.

The amplitude of a synthetic vector  $I_{-M}$  is given as

$$I_{-M} = \sqrt{I_{-d}^2 + I_{-q}^2}. \quad (14)$$

In order to evaluate the severity of the interturn short circuit, a sensitivity factor  $\lambda$  which takes into account the manufactured asymmetry is defined as

$$\lambda = 20 \lg \left( \frac{I_{-Mf}}{I_{-Mn}} \right), \quad (15)$$

where  $I_{-Mf}$  indicates the amplitude of synthetic vector in fault status and  $I_{-Mn}$  indicates the value in healthy status with the same load.

When the motor is healthy, the value of sensitivity factor  $\lambda$  is zero. With the greater fault severity,  $\lambda$  will increase as well. So it can be used to reflect the trend of the severity of interturn short circuit.

**2.3. Application of FCE Method in Broken Rotor Bars Fault Diagnosis.** To cope with the problem that spectral leakage coming from the fundamental component obscures rotor



FIGURE 1: The S3C2410X ARM board.



FIGURE 2: The signal conditioning board.

fault feature, FCE method can also be used to filter out the fundamental component accurately. Because the fault feature can be included in spectrum of phase current, only one-phase current signal is needed to be recorded in rotor fault diagnosis. The capacity of power grid is large enough; it can be seen that the stator voltage and the fundamental component in stator current have the same frequency. Therefore, reference signals whose frequency is equal to the one of stator voltage can be constructed. Then correlation analysis between the reference signals and stator current signal can be finished. The reference signals have no correlation with the harmonics and noise; it is easy to obtain the amplitude and phase of fundamental component via some simple data processing. The detailed realizing method is discussed below.

It is assumed that there are  $N$  points recorded in period  $T$ . The discrete-time array is noted as  $i(t_k)$ . According to (6), construct two reference signals. By (7) and (8), it is easy to obtain the amplitude  $I_{rM1}$  and phase  $\varphi_{r1}$  of fundamental component of phase current. In order to eliminate the interference of the fundamental component to the fault feature, the signal  $r(t_k)$  is given as follows:

$$r(t_k) = i(t_k) - I_{rM1} \sin(\omega t_k + \varphi_{r1}). \quad (16)$$

The signal  $r(t_k)$  can be reserved for the further analysis in the spectrum.

### 3. Fault Diagnosis System for Squirrel Cage Motor

The 32-bit microprocessor S3C2410X is taken as the core of stator current signal sampling. S3C2410X's on-chip A/D converter transforms the input signal into 10-bit binary digital codes at a maximum conversion rate of 500 ksp/s with 2.5 MHz A/D converter clock [21]. The snapshot of S3C2410X ARM board is shown in Figure 1.

The signal conditioning board includes three-phase current conditioning circuit, voltage frequency conditioning circuit, and motor speed conditioning circuit. The snapshot of circuit board is shown in Figure 2.

Via LabWindows/CVI software installed on the upper computer, the MCE method is applied to the interturn short circuit and broken rotor bars fault diagnosis, respectively. The structure frame of the system is shown in Figure 3.

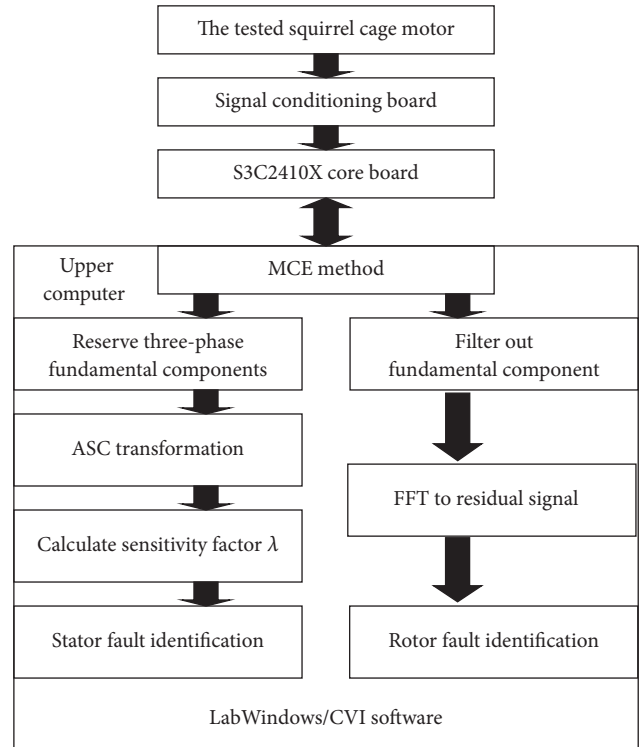


FIGURE 3: The structure frame of fault diagnosis system.

### 4. Experimental Results

**4.1. Results of Interturn Short Circuit Fault Diagnosis.** The tested motor's type is JO2-32-4. Its rated power is 3 kW, and rated speed is 1400 r/min. The load on the motor is changed by varying the exciting current of a magnetic powder brake. The motor experimental system is manifested in Figure 4.

The three-phase stator current signals, including healthy, one turn of short circuit, three turns of short circuit, and six turns of short circuit in phase A, are recorded by the experimental system. The correspondent waveform is shown in Figure 5.

The amplitude and phase information of three-phase fundamental component can be got by FCE method. According to (14), the amplitude of synthetic vector  $I_{-M}$  can be obtained. Then, by (15), the sensitivity factor  $\lambda$  which takes manufactured asymmetry into account can be calculated. The



FIGURE 4: The motor experimental system.

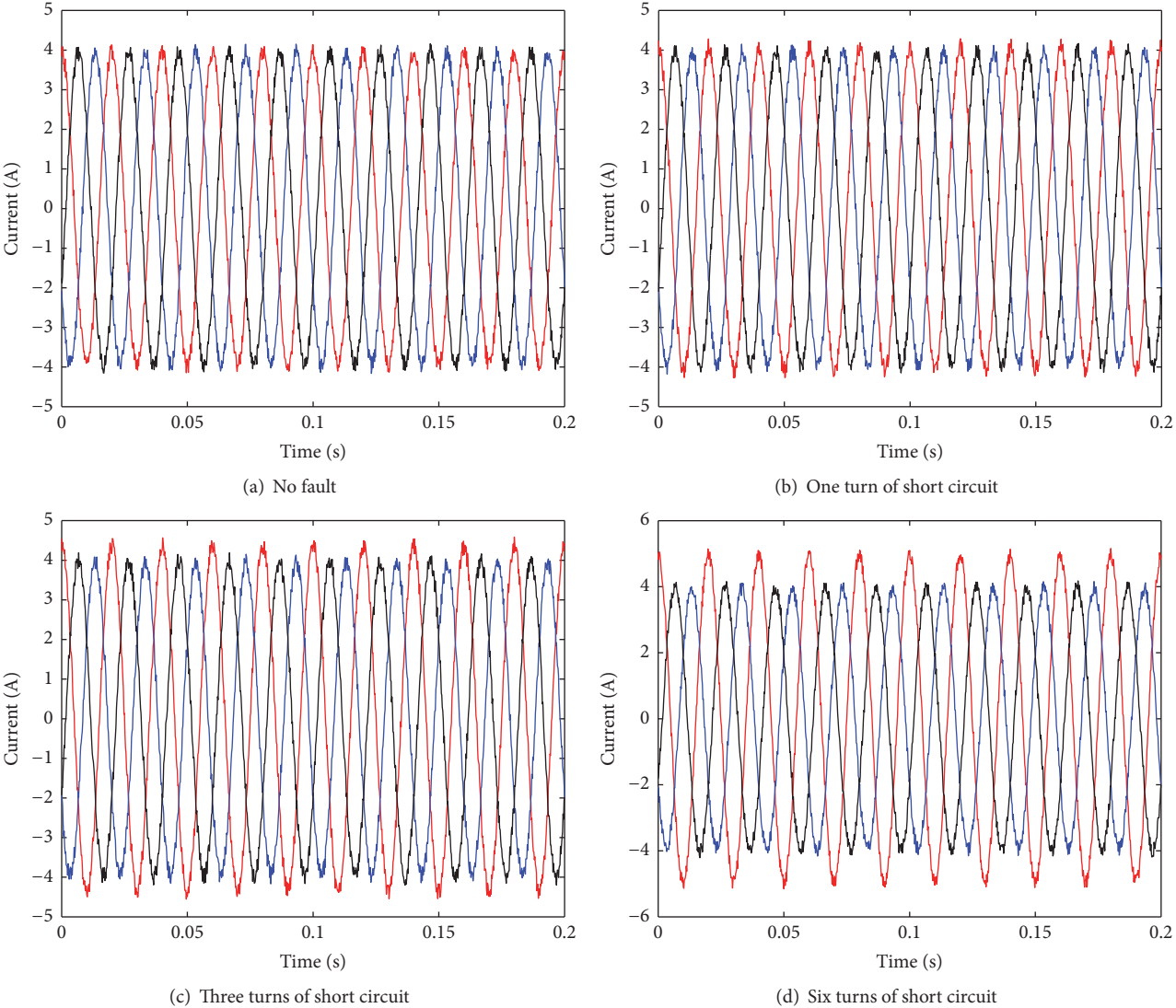


FIGURE 5: The three-phase current waveform in different turns of short circuit.

TABLE 1: The calculations in different turns of short circuit.

Turns	$I_{A1}$ (A)	$I_{B1}$ (A)	$I_{C1}$ (A)	$I_{-M}$ (mA)	$\lambda$
0	2.799	2.790	2.794	8.2	0.00
1	2.878	2.803	2.809	83.2	20.1
3	3.091	2.798	2.817	333.3	32.2
6	3.501	2.795	2.827	800.2	39.8

TABLE 2: The calculations obtained by the TSC method.

Turns	$I_A$ (A)	$I_B$ (A)	$I_C$ (A)	$I_{-M}$ (mA)	$\lambda$
0	2.886	2.877	2.881	7.7	0.00
1	2.967	2.890	2.897	70.1	19.2
3	3.187	2.885	2.905	280.1	31.2
6	3.609	2.882	2.916	699.8	39.2

calculations in different turns of short circuit are shown in Table 1.

$I_{A1}$ ,  $I_{B1}$ , and  $I_{C1}$  represent effective values of fundamental component.

In order to show the effectiveness of FCE method in the interturn short circuit fault diagnosis, the calculations obtained by the traditional symmetrical component (TSC) method are shown in Table 2 [22].

$I_A$ ,  $I_B$ , and  $I_C$  represent effective values of phase current.

According to the results in Tables 1 and 2, the contrast diagram of sensitivity factor is shown in Figure 6.

It can be concluded that, with the deterioration of the stator fault, the imbalance becomes more and more serious, and the value of the sensitivity factor is increased. Therefore, the defined sensitivity factor can correctly reflect on the severity of interturn short circuit fault, and it is feasible to set threshold value to decide whether to generate alerts.

Through the contrast diagram in Figure 6, it can be found that the calculations processed by FCE method are more sensitive to the short circuit fault than the ones of TSC. The influence of harmonics and noise in stator current can be effectively reduced by the FCE method, and it is proven to be more effective in the interturn short circuit fault diagnosis.

**4.2. Results of Broken Rotor Bars Fault Diagnosis.** The tested squirrel cage motor's type is Y90S-4. Its rated power is 1.1 kW, rated frequency is 50 Hz, and rated speed is 1400 r/min. The load on the motor can be changed by varying the exciting current of a magnetic powder brake. The sampling frequency of the current signal is 1 kHz, and the sampling time is 1 s. The broken bar can be generated by partial or full drilling [23, 24]. The tested motor has one broken bar in the rotor, which is shown in Figure 7.

When the tested motor is connected to the 50 Hz power grid with rated load, the measured speed is 1402 r/min, and the frequency values of rotor fault components based on  $(1 \pm 2s)f$  are 43.4 Hz and 56.6 Hz. When the motor is operated under 50% rated load, the measured speed is up to 1462 r/min. The frequency of rotor fault components based on  $(1 \pm 2s)f$  is 47.5 Hz and 52.5 Hz. The local magnification of stator current spectrum is shown in Figure 8.

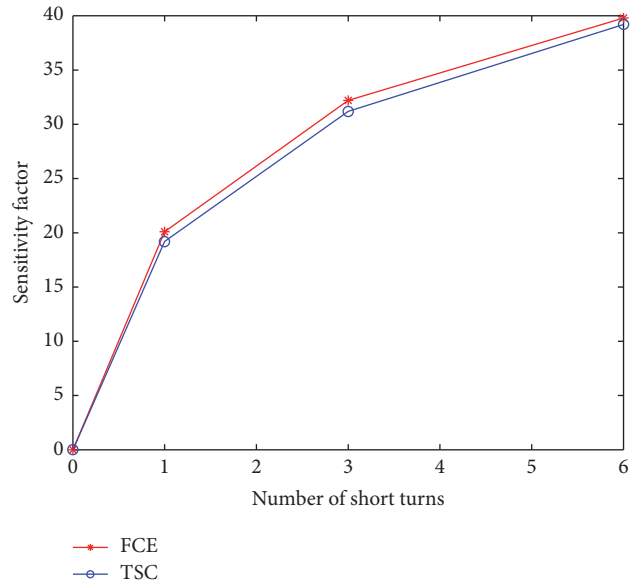


FIGURE 6: The contrast diagram of sensitivity factor.



FIGURE 7: The rotor with one broken bar.

In Figure 8, it can be found that the spectral leakage coming from the fundamental component obscures rotor fault components, and it is difficult to distinguish the rotor fault feature from the spectrum even by logarithmic ordinate. In the case of 50% rated load, the fault components get closer to the fundamental component, and there is little indication of rotor fault in the spectrum.

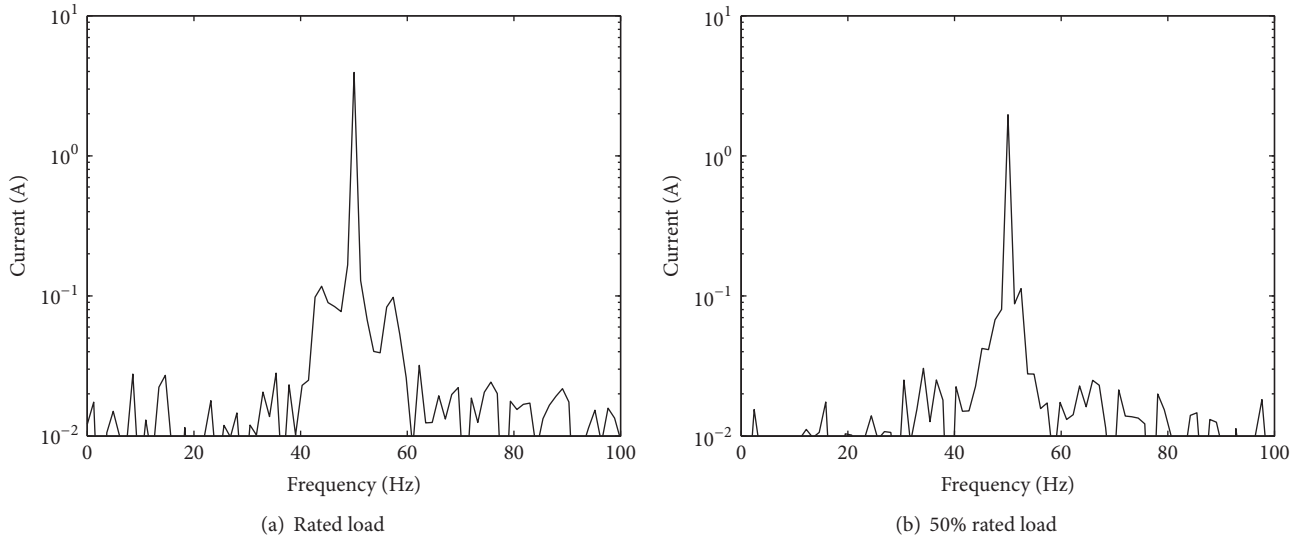


FIGURE 8: The local magnification of stator current spectrum.

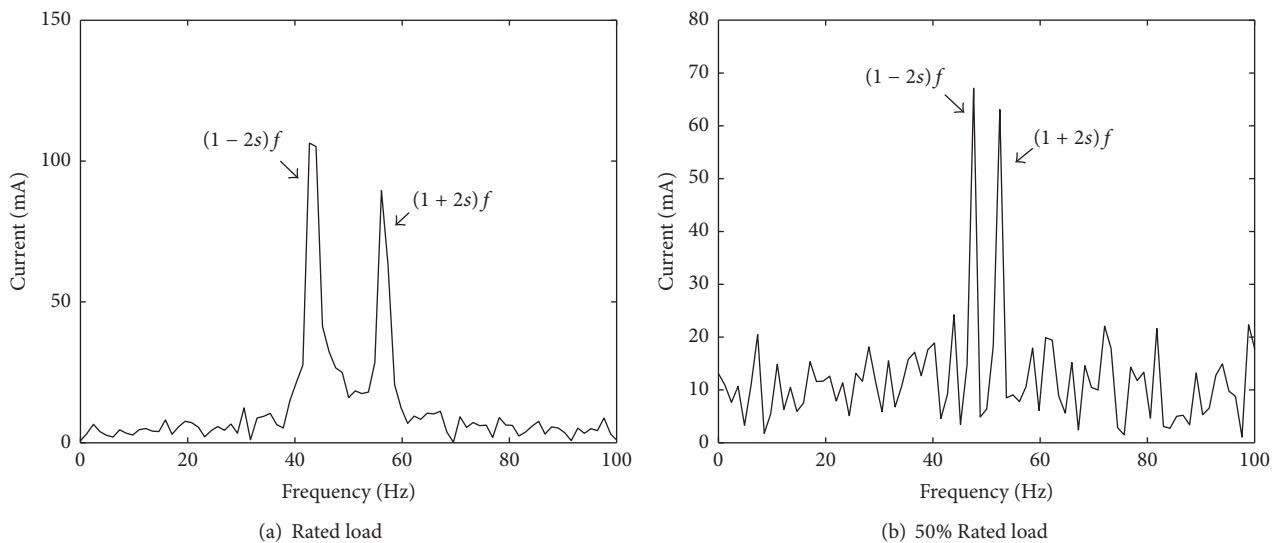


FIGURE 9: The local magnification of stator current spectrum dealing with FCE method.

The local magnifications of stator current spectrums which are dealing with FCE method under 100% and 50% rated load are shown in Figure 9.

Figure 9 shows that the rotor fault components can emerge clearly from the spectrum, even under the light load. The experimental results have shown quite good agreement with the theory, and the FCE method can be applied in broken rotor bars diagnosis.

## 5. Conclusions

In this paper, FCE method is proposed to extract the feature in stator and rotor faults diagnosis of squirrel cage motor, respectively. Through the analysis, we can get the following conclusions:

- (1) Via correlation analysis between the constructed signals and stator current signal, the amplitude and phase information of fundamental component can be obtained accurately.
- (2) In the interturn short circuit fault diagnosis, the negative effects of the harmonics and noise in stator current signal can be avoided based on FCE method. The defined sensitivity factor can reflect the trend of severity of stator interturn short circuit. In addition, only single-phase short circuit is discussed in this paper, and other short circuit faults will be reported in our future work.
- (3) In the broken rotor bars fault diagnosis, FCE method can be used to eliminate the interference of the fundamental component to the fault feature. The fault

feature identification is enhanced in the stator current spectrum dealing with this method, even in the case of light load.

## Conflicts of Interest

The authors declare that they have no conflicts of interest.

## Acknowledgments

This project is supported by National Natural Science Foundation of China (Grant no. 51541506), Natural Science Youth Foundation of Hebei (Grant no. E2017208086), Science and Technology Research Youth Foundation for Hebei College (Grant no. QN2017329), and General Aviation Foundation of Hebei University of Science and Technology (Grant no. 201525).

## References

- [1] V. N. Ghate and S. V. Dudul, "Optimal MLP neural network classifier for fault detection of three phase induction motor," *Expert Systems with Applications*, vol. 37, no. 4, pp. 3468–3481, 2010.
- [2] G. Singh, T. C. A. Kumar, and V. N. A. Naikan, "Induction motor inter turn fault detection using infrared thermographic analysis," *Infrared Physics & Technology*, vol. 77, no. 7, pp. 277–282, 2016.
- [3] R. Sharifi and M. Ebrahimi, "Detection of stator winding faults in induction motors using three-phase current monitoring," *ISA Transactions*, vol. 50, no. 1, pp. 14–20, 2011.
- [4] H. Çaliş and A. Çakir, "Rotor bar fault diagnosis in three phase induction motors by monitoring fluctuations of motor current zero crossing instants," *Electric Power Systems Research*, vol. 77, no. 5-6, pp. 385–392, 2007.
- [5] W. F. Godoy, I. N. D. Silva, A. Goedel, and R. H. C. Palácios, "Evaluation of stator winding faults severity in inverter-fed induction motors," *Applied Soft Computing*, vol. 32, pp. 420–431, 2015.
- [6] F. Fang, S.-Y. Yang, X.-G. Hou, and Z.-G. Wu, "A novel method of calculating negative sequence current," *Journal of Wuhan University of Technology*, vol. 33, no. 5, pp. 872–875, 2009.
- [7] P. Naderi, "Cage-rotor induction motor inter-turn short circuit fault detection with and without saturation effect by MEC model," *ISA Transactions*, vol. 64, no. 9, pp. 216–230, 2016.
- [8] R. Roshanfekar and A. Jalilian, "Analysis of rotor and stator winding inter-turn faults in WRIM using simulated MEC model and experimental results," *Electric Power Systems Research*, vol. 119, pp. 418–424, 2015.
- [9] Y.-G. Li, H.-M. Li, H. Zhao, and S.-T. Wan, "Fault identification method of rotor inter turn short-circuit using stator winding detection," *Proceedings of the Chinese Society for Electrical Engineering*, vol. 2, no. 2, pp. 856–860, 2004.
- [10] S.-T. Wan, H.-M. Li, and Z.-F. Xu, "Analysis of generator vibration characteristic on stator winding inter-turn short circuit fault," *Proceedings of the Chinese Society for Electrical Engineering*, vol. 4, no. 24, pp. 57–161, 2004.
- [11] C. T. Kowalski and T. Orłowska-Kowalska, "Neural networks application for induction motor faults diagnosis," *Mathematics and Computers in Simulation*, vol. 63, no. 3–5, pp. 435–448, 2003.
- [12] J.-W. Zhang, Q. Yao, N.-H. Zhu, L. Yang, and Q. Lu, "Method for diagnosing the stator winding faults in squirrel cage induction motor," *High Voltage Engineering*, vol. 6, no. 33, pp. 114–117, 2007.
- [13] X.-G. Hou, Z.-G. Wu, L. Xia, and L.-P. Bu, "Application of instantaneous power decomposition technique in induction motors stator fault diagnosis," in *Proceedings of the Chinese Society for Electrical Engineering*, vol. 25, pp. 110–115, 2005.
- [14] M. R. Mehrjou, N. Mariun, M. Hamiruce Marhaban, and N. Misron, "Rotor fault condition monitoring techniques for squirrel-cage induction machine—a review," *Mechanical Systems and Signal Processing*, vol. 25, no. 8, pp. 2827–2848, 2011.
- [15] G. G. Acosta, C. J. Verucchi, and E. R. Gelso, "A current monitoring system for diagnosing electrical failures in induction motors," *Mechanical Systems and Signal Processing*, vol. 20, no. 4, pp. 953–965, 2006.
- [16] K. N. Gyftakis, A. J. M. Cardoso, and J. A. Antonino-Daviu, "Introducing the filtered park's and filtered extended park's vector approach to detect broken rotor bars in induction motors independently from the rotor slots number," *Mechanical Systems and Signal Processing*, vol. 93, no. 1, pp. 30–50, 2017.
- [17] I. Aydin, M. Karakose, and E. Akin, "A new method for early fault detection and diagnosis of broken rotor bars," *Energy Conversion and Management*, vol. 52, no. 4, pp. 1790–1799, 2011.
- [18] M. Abd-el-Malek, A. K. Abdelsalam, and O. E. Hassan, "Induction motor broken rotor bar fault location detection through envelope analysis of start-up current using hilbert transform," *Mechanical Systems and Signal Processing*, vol. 93, no. 1, pp. 332–350, 2017.
- [19] Y. Shao, "Feature extracting method of stator and rotor faults of induction motor by Park vector rotating filter," *Electric Machines and Control*, vol. 14, no. 143, pp. 57–61, 2010.
- [20] T. Lobos, Z. Leonowicz, J. Szymanda, and P. Ruczewski, "Application of higher-order spectra for signal processing in electrical power engineering," *COMPEL—The International Journal for Computation and Mathematics in Electrical and Electronic Engineering*, vol. 17, no. 5, pp. 602–611, 1998.
- [21] Y. Liu, L. Guo, Q. Wang, G. An, M. Guo, and H. Lian, "Application to induction motor faults diagnosis of the amplitude recovery method combined with FFT," *Mechanical Systems and Signal Processing*, vol. 24, no. 8, pp. 2961–2971, 2010.
- [22] X.-F. Liu, S.-J. Cheng, and J.-Y. Wen, "An improved method of instantaneous symmetrical components and its detection for positive and negative sequence current," *Proceedings of the Chinese Society for Electrical Engineering*, vol. 28, no. 1, pp. 52–58, 2008.
- [23] F. Gu, T. Wang, A. Alwodai, X. Tian, Y. Shao, and A. D. Ball, "A new method of accurate broken rotor bar diagnosis based on modulation signal bispectrum analysis of motor current signals," *Mechanical Systems and Signal Processing*, vol. 50-51, no. 1, pp. 400–413, 2015.
- [24] M. O. Mustafa, G. Nikolakopoulos, T. Gustafsson, and D. Kominiak, "A fault detection scheme based on minimum identified uncertainty bounds violation for broken rotor bars in induction motors," *Control Engineering Practice*, vol. 48, pp. 63–77, 2016.

## Research Article

# Fault Identification of Rotor System Based on Classifying Time-Frequency Image Feature Tensor

Hui Li,<sup>1,2</sup> Xiaofeng Liu,<sup>2</sup> and Lin Bo<sup>2</sup>

<sup>1</sup>Chongqing College of Electronic Engineering, Chongqing 400444, China

<sup>2</sup>The State Key Laboratory of Mechanical Transmission, Chongqing 400044, China

Correspondence should be addressed to Xiaofeng Liu; 109742210@qq.com

Received 6 November 2016; Revised 5 January 2017; Accepted 19 January 2017; Published 14 March 2017

Academic Editor: Zhixiong Li

Copyright © 2017 Hui Li et al. This is an open access article distributed under the Creative Commons Attribution License, which permits unrestricted use, distribution, and reproduction in any medium, provided the original work is properly cited.

In the field of rotor fault pattern recognition, most of classical pattern recognition methods generally operate in feature vector spaces where different feature values are stacked into one-dimensional (1D) vector and then processed by the classifiers. In this paper, time-frequency image of rotor vibration signal is represented as a texture feature tensor for the pattern recognition of rotor fault states with the linear support higher-tensor machine (SHTM). Firstly, the adaptive optimal-kernel time-frequency spectrogram visualizes the unique characteristics of rotor fault vibration signal; thus the rotor fault identification is converted into the corresponding time-frequency image (TFI) pattern recognition. Secondly, in order to highlight and preserve the TFI local features, the TFI is divided into some TFI subzones for extracting the hierarchical texture features. Afterwards, to avoid the information loss and distortion caused by stacking multidimensional features into vector, the multidimensional features from the subzones are transformed into a feature tensor which preserves the inherent structure characteristic of TFI. Finally, the feature tensor is input into the SHTM for rotor fault pattern recognition and the corresponding recognition performance is evaluated. The experimental results showed that the method of classifying time-frequency texture feature tensor can achieve higher recognition rate and better robustness compared to the conventional vector-based classifiers, especially in the case of small sample size.

## 1. Introduction

Rotor system as an important asset exists in a wide range of industry applications and its fault identification is crucial to its design and usage. Its vibration signals are generally used to detect its healthy state to reduce the catastrophic damage and the down-time of machinery. Disk unbalance and resonance are the two main sources of rotating machinery vibration. The vibrations due to such sources will affect the system critical parts, such as bearings, gears, motor, seals, and coupling. Disk unbalance is a condition in which the center of mass of a rotating disk is not coincident with the center of rotation. Unbalance in rotor system is unavoidable and cannot be completely eliminated. Jalan and Mohanty [1] stated that, due to some reasons such as porosity in casting, nonuniform density of material, manufacturing tolerances, and gain or loss of material during operation, rotors can never be perfectly balanced in the practical applications. Oil film instability is a common nonlinear fault in a rotor-bearing

system, which may bring a serious hazard to rotary machines. Liu et al. [2] also have been devoted to study the instability behaviors of rotor-bearing systems with asymmetric inertia, which are usually caused by the coupled effects of the nonlinear oil film force, unbalanced centrifugal force, journal whirl inertia force, rotor gravity, and other external load. In the compound fault of oil film instability and unbalance, the vibration signal collected from a rotor-bearing system exhibits phase/frequency coupling features which cannot be directly used to identify rotor healthy state based on the traditional data analysis methods, such as orbit portrait, FFT spectra, cepstra and time-frequency, or time-scale analysis [3].

For the improvement of reliability, safety, and efficiency of technical processes, fault pattern recognition is used as advanced supervision tools in present industries, which not only can liberate human experience evaluation but also can achieve accurate and timely fault warning. Generally speaking, there are two main steps in the fault pattern

recognition: the first step is the feature extraction with some signal processing methods, and the second step is the fault state identification with artificial intelligence technique based on the extracted features. It is well known that time-frequency spectrogram can visualize the unique characteristics of vibration signal, based on which the fault state can be automatically identified with the time-frequency image (TFI) recognition technology. Owing to the fact that the time-frequency matrix of vibration signal has a big randomness and strong irregularity, it is not suitable to do the direct identification of fault state with the general image recognition methods such as syntactic recognition method [4], template matching method [5], and geometrical transformation method [6] in the practical fault diagnosis. Artificial intelligence technique is a good choice to realize the automatic identification of fault condition and prevents the subjective error in the operator observation. The intelligent TFI identification usually focuses on how to extract the useful features to characterize the spectrogram image. Many types of image features, such as moment invariants [7], gray statistical characteristics, textural features [8], and differential box-counting fractal dimension [9], are usually extracted for TFI autorecognition. Most of these extracted features represent the global information of TFI. But for the vibration signals of the rotor system in fault states, the characteristic signal components concentrating in some local zone of TFI would lead to nonuniform distribution of TFI characteristics. The global feature extraction of TFI would provide some unreliable identification results since the real fault characteristics are averaged out. The useful information gets lost so as to decrease the accuracy of fault identification.

In order to make up the information loss in the global feature extraction, it is necessary to segment TFI segmentation and carry out the feature extraction in different frequency bands. That is, each frequency band regions are separately processed to extract their corresponding features. In the field of fault state pattern recognition, the multidimensional features in machine learning are generally transformed to a vector representation and then processed by the classical learning algorithms operating with vectors. Although there are many ways to vectorize multidimensional data, it has been observed that such operation usually leads to significant loss of important information, since some values which were in local vicinity become differently arranged if data are arbitrarily linearized into a vector [10]. And it is necessary to reduce the dimension of time-frequency features to appropriate size with some dimensionality reduction techniques such as factor analysis, principal component analysis, independent component analysis, and singular value decomposition [11–13]. But these dimensionality reduction techniques suffer the problem of overdecomposition or incomplete decomposition which might distort the feature correlations, increase architectural complexity and malfunction of classifier, and even lead to the false classification results. In a word, despite these feasible methods in vectors operating space, they do not make a full exploitation of the TFI characteristics.

In this paper, the feature tensor is introduced to characterize the TFI of rotor vibration signal, which can keep the correlation information between different frequency bands

and the integrality of the TFI. However, due to the so-called curse of dimensionality and small size problems, SVM cannot handle the tensor objects effectively. For the feature tensors of TFIs, the linear support higher-tensor machine (SHTM) is used as a tensor classifier for the rotor fault identification. The SHTM is a multilinear construct learning model constructed by extending the support vector machine learning framework to tensor patterns [14]. The approach presents the supervised tensor learning framework by applying a combination of the convex optimization and multilinear operators [15]. The experimental results showed that the approach of classifying time-frequency image feature tensor can identify the rotor faults more accurately compared to the conventional feature vector classifiers. The rest of this paper is organized as follows. Section 2 provides the introduction of adaptive optimal-kernel distribution. Section 3 gives texture analysis carried out on gray level cooccurrence matrix (GLCM) of TFI. Section 4 provides the theory of linear Support higher-Order tensor machine for multiclassification. Section 5 explains the flowchart of proposed method. The experimental results, discussions, and analysis are presented in Section 6. The conclusions are given in Section 7.

## 2. Adaptive Optimal-Kernel Time-Frequency Distribution and TFI Segmentation

Adaptive optimal-kernel (AOK) time-frequency transform is a suitable tool to obtain the time-frequency images of vibration signals of rotary machine. The AOK time-frequency distribution can preserve simultaneously good resolutions in time and frequency with less cross-term interferences. It is expressed as

$$\begin{aligned} \text{AOK}(t, f) &= \iint_{-\infty}^{+\infty} A(\tau, \nu) \phi(\tau, \nu) \exp[-2\pi(\nu t + f\tau)] d\nu d\tau, \end{aligned} \quad (1)$$

where the analyzed signal is noted as  $x(t)$ ,  $A(\tau, \nu) = \int_{-\infty}^{+\infty} x(t + \tau/2)x^*(t - \tau/2) \exp(-j2\pi\nu t) dt$  is the ambiguity function, and  $\phi(\tau, \nu)$  is a 2D radially Gaussian kernel function performed as a low-pass filter in the ambiguity domain. The optimal-kernel function can be obtained by minimizing autoterm distortion by passing autoterm energy as much as possible for a kernel of fixed volume so as to suppress cross-terms. AOK( $t, f$ ) is used to analyze the rotor vibration signals and the analysis results are expressed in the TFI with 256 gray levels. Based on the TFIs, how to classify the vibration signals correctly corresponding to the rotor states is a typical pattern recognition problem. In the view of too many pixels in TFI, it is necessary to transform the TFI into the expected low-dimension feature space and keep the information of TFI as much as possible.

The global statistics for the whole TFI cannot describe the local details of the signal. The fault characteristic components generally concentrate in some frequency bands of TFI, not like the noises distributed in the whole plane of TFI. In order

to get more details about fault characteristic components, the TFI is divided into some frequency band regions, as shown in

$$\text{AOK}(t, f) = \sum_{i=1}^I R_i(t, f), \quad (2)$$

where  $I$  is the number of TFI segmented blocks and  $R_i(t, f)$  is the  $i$ th frequency band block. The textural descriptors are extracted in each block instead of from the whole TFI.

### 3. Texture Features Extraction

For the intelligent pattern recognition of TFIs, the key point is to extract the effective features which can accurately capture the fault information of rotor system. Texture as one of the basic feature of TFI has clear meaning representing the fault information in the rotor vibration signal and can be easily calculated. Texture feature can steadily describe the spatial changes situation of the color, the gradation or the fine structure, and shape of the image with favorable rotation invariance and anti-interference capability [16, 17]. Texture is analyzed using a statistical technique based on GLCM, which use the gray level spatial correlation, firstly to construct a cooccurrence matrix according to the direction and distance between image pixels and then to extract from cooccurrence matrix meaningful statistical data as the image texture features.

For the matrix image with gray level  $N_g$ , its horizontal and vertical direction have  $N_x$  and  $N_y$  pixels, respectively. Given  $L_x = \{1, 2, \dots, N_x\}$ ,  $L_y = \{1, 2, \dots, N_y\}$ , and  $G = \{0, 1, \dots, N_g - 1\}$  as quantitative gray level set, the image can be expressed as  $I : L_x \times L_y \rightarrow G$ . Gray level cooccurrence matrix presents a pair of pixels which is on the  $(\Delta_x, \Delta_y)$  direction, horizontal distance has  $\Delta_x$  pixels, vertical distance has  $\Delta_y$  pixels, and each has gray value probability is of  $i$  and  $j$ , respectively. It can be expressed as  $P(i, j, \Delta_x, \Delta_y)$ , which is the element of gray level cooccurrence matrix.  $P(i, j, \Delta_x, \Delta_y)$  is written as follows:

$$P(i, j, \Delta_x, \Delta_y) = \# \left\{ \begin{array}{l} ((k, l), (m, n)) \in (L_x \times L_y) \times (L_x \times L_y) \\ I(k, l) = i, I(m + \Delta_x, n + \Delta_y) = j \end{array} \right\}, \quad (3)$$

where  $\#\{X\}$  is the elements number of set  $X$ . When  $P(i, j, \Delta_x, \Delta_y)$  is normalized

$$p(i, j, \Delta_x, \Delta_y) = \frac{P(i, j, \Delta_x, \Delta_y)}{G}, \quad (4)$$

where  $G$  is normalized constant which is sum of all  $P(i, j, \Delta_x, \Delta_y)$  elements. Six typical texture features can be extracted from gray level cooccurrence matrix as follows and noted as  $m_1, m_2, m_3, m_4, m_5, m_6$ , respectively.

- (1) Angular second moment (ASM) or called energy is used to measure the uniformity of image gray level, it can be written as follows:

$$m_1 = \text{ASM}(\Delta_x, \Delta_y) = \sum_{i,j} p((i, j, \Delta_x, \Delta_y))^2. \quad (5)$$

- (2) Inverse difference moment (IDM) is

$$m_2 = \text{IDM} = \frac{\sum_{i,j} p(i, j, \Delta_x, \Delta_y)}{1 + (i - j)^2}. \quad (6)$$

- (3) Contrast (CON) reflects the clear degree of image texture; rough texture has small inertial and fine texture has large inertial; it is represented as follows:

$$m_3 = \text{CON}(\Delta_x, \Delta_y) = \sum_{i,j} (i - j)^2 p(i, j, \Delta_x, \Delta_y). \quad (7)$$

- (4) Correlation (COR) is used to describe the matrix similarity degree between the row element or the column elements. It is a measurement for gray linear.

$$m_4 = \text{COR}(\Delta_x, \Delta_y) = \frac{[\sum_{i,j} (i \times j \times p(i, j, \Delta_x, \Delta_y)) - \mu_x \mu_y]}{\sigma_x \sigma_y}, \quad (8)$$

where,  $\mu_x, \mu_y$  and  $\sigma_x, \sigma_y$  are the mean value and standard deviation of  $p_x (p_x = \sum_i p(i, j, \Delta_x, \Delta_y))$  and  $p_y (p_y = \sum_j p(i, j, \Delta_x, \Delta_y))$ .

- (5) Variance (VAR) of sum of squares is

$$m_5 = \text{VAR}(\Delta_x, \Delta_y) = \sum_{i,j} (i - \mu)^2 p(i, j, \Delta_x, \Delta_y), \quad (9)$$

where  $\mu$  is the mean value of  $p(i, j, \Delta_x, \Delta_y)$ .

- (6) Entropy (ENT) shows the clutter degree of image texture. The higher the image texture consistency, the greater the entropy; otherwise, the higher the image texture disorderly degree, the smaller the entropy

$$\text{ENT}(\Delta_x, \Delta_y) = \sum_{i,j} -p(i, j, \Delta_x, \Delta_y) \times \log(p(i, j, \Delta_x, \Delta_y)). \quad (10)$$

### 4. Linear Support Higher-Order Tensor Machine for Multiclassification

Tensor presentation has the advantage of preserving intrinsic structure of dataset, such as the relationships between dimensions within the same order and the relationships of dimensions in the different orders. Due to the so-called curse of dimensionality and the small sample size problem, the SVM model based on vector space cannot directly deal with tensor patterns. So the SHTM based on the SVM and tensor rank-order decomposition TVM is applied to classify the multidimensional features in rotor fault states. The SHTM overcomes the disadvantages of local minimal problem and nonconvex optimization problem in conventional supervised tensor learning framework.

Given a training set of  $M$  pairs of samples  $\{X_m, y_m\}_{m=1}^M$ , where  $X_m = \mathfrak{R}^{I_1 \times I_2 \times \dots \times I_N}$  is the input data and  $y_m \in \{-1, 1\}$

is the corresponding class labels of  $X_m$ , the SHTM model for binary classification is in the following:

$$\begin{aligned} \min_{\mathbf{W}, b, \xi} \quad & J(\mathbf{W}, b, \xi) = \frac{1}{2} \|\mathbf{W}\|_F^2 + C \sum_{m=1}^M \xi_m \\ \text{s.t.} \quad & y_m (\langle \mathbf{W}, X_m \rangle + b) \geq 1 - \xi_m, \quad m = 1, \dots, M \\ & \xi_m \geq 0, \\ & m = 1, \dots, M, \end{aligned} \quad (11)$$

where  $\mathbf{W}$  is the weight tensor of the hyperplane,  $b$  is the bias,  $\xi_m$  is the error of the  $m$ th training sample, and  $C$  is the tradeoff between the classification margin and misclassification error. For the Lagrangian function of the optimization problem (11), noted as  $L(W, b, a, \beta, \xi)$ , let the partial derivative operations on  $L(W, b, a, \beta, \xi)$  with respect to  $W$ ,  $b$ , and  $\xi_m$  be zeroes, respectively; we have the optimization problem of (11) as follows:

$$\min_{\alpha} \quad \frac{1}{2} \sum_{i,j=1}^M \alpha_i \alpha_j y_i y_j \langle X_i, X_j \rangle - \sum_{m=1}^M \alpha_m \quad (12)$$

$$\text{Subject to} \quad \sum_{m=1}^M \alpha_m y_m = 0 \quad (13)$$

$$0 \leq \alpha_m \leq C, \quad m = 1, \dots, M,$$

where  $\alpha_m$  are the Lagrange multipliers and  $\langle X_i, X_j \rangle$  are the inner products of  $X_i$  and  $X_j$ .

Let the rank-one decomposition of  $X_i$  and  $X_j$  be  $X_i \approx \sum_{r=1}^R \mathbf{x}_{ir}^{(1)} \circ \mathbf{x}_{ir}^{(2)} \circ \dots \circ \mathbf{x}_{ir}^{(N)}$  and  $X_j \approx \sum_{r=1}^R \mathbf{x}_{jr}^{(1)} \circ \mathbf{x}_{jr}^{(2)} \circ \dots \circ \mathbf{x}_{jr}^{(N)}$ , respectively; then the inner product of  $X_i$  and  $X_j$  is calculated as follows:

$$\begin{aligned} \langle X_i, X_j \rangle \\ \approx \sum_{p=1}^R \sum_{q=1}^R \langle \mathbf{x}_{ip}^{(1)}, \mathbf{x}_{jq}^{(1)} \rangle \langle \mathbf{x}_{ip}^{(2)}, \mathbf{x}_{jq}^{(2)} \rangle \dots \langle \mathbf{x}_{ip}^{(N)}, \mathbf{x}_{jq}^{(N)} \rangle. \end{aligned} \quad (14)$$

Substituting (14) into (12), then the class label of a testing example  $X$  is predicted as follows:

$$y(X) = \text{sign} \left( \sum_{m=1}^M \sum_{p=1}^R \sum_{q=1}^R \alpha_m y_m \prod_{n=1}^N \langle \mathbf{x}_{mp}^{(n)}, \mathbf{x}_q^{(n)} \rangle + b \right), \quad (15)$$

where  $\mathbf{x}_{mp}^{(n)}$  and  $\mathbf{x}_q^{(n)}$  are the elements of the rank-one decomposition of  $X_m$  and  $X$ , respectively. So the normal hyperplane can be expressed as a linear combination of training samples in tensor space.

Like the  $L$ -class classification problem of SVM, the one-against-one support tensor machine needs to construct  $L(L-1)/2$  binary classification SHTM models where each one is trained on data points from two classes. The class label of a testing example  $X$  can be predicted by applying majority voting strategy; that is, the vote counting takes into account the outputs of all binary classifiers. If  $X$  belongs to the  $i$ th

class, then the  $i$ th class gets one vote; otherwise the  $j$ th class gets one vote;  $X$  is labeled by the class with the most votes. The differences of SHTM versus SVM are as follows:

- (1) SVM forces a tensor into vectors as input, while SHTM adopts a more compact tensor representations, that is,  $R$  rank-one tensor as input, which not only has the capability for capturing structural information of features, but also avoids the so-called curse of dimensionality and small size sample problems in vector classification of SVM.
- (2) The decision function of vector-based SVM algorithm is in the linear form and determined by weight vector and the bias in hyperplane of vector space, while the decision function of SHTM algorithm is in the multilinear form and determined by weight tensor  $\mathbf{W}$  and the bias in the hyperplane of tensor space. It is more convenient to construct a maximal separable classifier between two classes or transform tensor data into the separable feature space with the tensor decomposition and transform.
- (3) When the number of training points is relatively small, it is easy to show the overfitting phenomenon in the processing of SVM learning, because it is difficult to reduce the parameter vectors in vector-based machine learning methods. But, for the SHTM, the number of parameters can be reduced by the decomposition of the parameter tensor and the low rank replacement techniques, so as to avoid the overfitting phenomenon in high dimension and small size sample.
- (4) For a set of tensor samples  $\{X_m \in R^{I_1 \times I_2 \times \dots \times I_N}, y_m\}_{m=1}^M$ , SVM requires  $O((M+1) \prod_{n=1}^N I_n + 1)$  memory space, while SHTM only requires  $O((M+1)R \sum_{n=1}^N I_n + 1)$  memory space, where  $R$  is the rank of tensor input. The computational complexity of SVM is  $O(M^2 \prod_{n=1}^N I_n)$ ; the computational complexity of SHTM is  $O(M^2 R^2 \sum_{n=1}^N I_n)$ . It is clear that that SHTM is more efficient than SVM.

## 5. Proposed Method

As mentioned previously, some useful characteristic information about rotor fault might be lost in the uniform calculation of global TFT texture features. The texture features are extracted in each subregion of TFI by segmenting frequency band. These features in the different frequency band region form a multidimensional array. The multidimensional features in machine learning are generally are firstly transformed to a vector representation and then processed by the classical learning algorithms operating with vectors. However, such multi-to-one-dimensional transformations usually lead to loss of important information. So the features are formed to a tensor preserving data dimensionality complex structure. The feature tensor can capture structural information relations among the texture feature values in different frequency bands. It has been clarified in Section 3 that the SHTM is the

generalization of the standard linear SVM to tensor patterns into tensor space and efficient for the classification of feature tensors. Therefore, the tensor rank-one decomposition is performed on the feature tensors which are processed by the SHTM for the classification of rotor fault states. The proposed method is explained with the following steps.

*Step 1.* Collect the vibration signal of the rotor-bearing system in normal and fault conditions.

*Step 2.* Perform the time-frequency transform for each vibration signal sample, and their time-frequency distributions can be obtained and expressed as the corresponding TFIs.

*Step 3.* Optimally segment each TFI is into  $I$  frequency band zones which are taken as  $I$  subimages  $R_i(t, f)$ ,  $i = 1, 2, \dots, I$ .

*Step 4.* Process TFI zone  $R_i(t, f)$  with gray level, and its GLCM is calculated as  $GLCM_{R_i}$ ,  $i = 1, 2, \dots, I$ . The texture features are calculated in each GLCM, which forms the feature vector  $\mathbf{x}_{R_i} = [x_1^{R_i}, x_2^{R_i}, \dots, x_j^{R_i}]$ ,  $j = 1, 2, \dots, J$ .  $x_j^{R_i}$  represents the  $j$ th texture feature of  $GLCM_{R_i}$ .

*Step 5.* In order to preserve data dimensionality and allow for processing of complex structures, the texture features are represented as a synthetic feature tensor shown in (16) according to the sequence of frequency band blocks.

$$X^{I \times J} = \begin{bmatrix} \mathbf{x}_{R_1} \\ \vdots \\ \mathbf{x}_{R_i} \\ \vdots \\ \mathbf{x}_{R_I} \end{bmatrix} = \begin{bmatrix} x_1^{R_1} & \cdots & x_j^{R_1} & \cdots & x_J^{R_1} \\ \vdots & \ddots & \vdots & \ddots & \vdots \\ x_1^{R_i} & & x_j^{R_i} & & x_J^{R_i} \\ \vdots & & \vdots & \ddots & \vdots \\ x_1^{R_I} & & x_j^{R_I} & & x_J^{R_I} \end{bmatrix}, \quad (16)$$

$i = 1, 2, \dots, I, \quad j = 1, 2, \dots, J.$

Here  $X^{I \times J}$  is the second-order tensor for the SHTM input.

*Step 6.* In view of the spatial distribution characteristics of frequency components, the absolute values of texture feature cannot reflect effectively the differences between the TFI blocks. To facilitate a fair comparison, each column value of  $X^{I \times J}$  is normalized; that is,  $x_j^{R_i} = x_j^{R_i} / \sum_{i=1}^I x_j^{R_i}$ ; then the normalized feature tensor  $\widehat{X}^{I \times J}$  is gotten.

*Step 7.* The normalized feature tensor  $\widehat{X}^{I \times J}$  (noted as is  $X_p$ ) is decomposed into  $R$  rank-1 tensor. The  $R$  rank-1 decomposition for  $X_p$  is to find the output vector  $\mathbf{u}_r$  and  $\mathbf{v}_r$  ( $1 \leq r \leq R$ ) make  $X_p \approx \sum_{r=1}^R \mathbf{u}_r \circ \mathbf{v}_r$ .  $\mathbf{u}_r$  and  $\mathbf{v}_r$  ( $1 \leq r \leq R$ ) make  $X_p \approx \sum_{r=1}^R \mathbf{u}_r \circ \mathbf{v}_r$ . With the initial values of  $r$ ,  $\mathbf{u}_r^0$ , and  $\mathbf{v}_r^0$ , set  $\mathbf{u}_r^{t+1} = X_p \times_2 \mathbf{v}_r^t$ ,  $\mathbf{v}_r^{t+1} = X_p \times_2 \mathbf{u}_r^t$  and normalize  $\mathbf{u}_r^{t+1}$ ,  $\mathbf{v}_r^{t+1}$ . Supposing

$$\|(\mathbf{u}_r^{t+1}, \mathbf{v}_r^{t+1}) - (\mathbf{u}_r^t, \mathbf{v}_r^t)\|_F^2 \leq \varepsilon, \quad (17)$$

where  $\varepsilon$  is the decomposing control threshold,  $\mathbf{u}_r$  and  $\mathbf{v}_r$  would be the outputs of the  $R$  rank-1 decomposition. Otherwise,  $X_p = X_p - \mathbf{u}_r^{t+1} \circ \mathbf{v}_r^{t+1}$ ,  $r = r + 1$ , and repeat (17).

*Step 8.* In the same way, the  $R$  rank-1 tensor of training sample  $X_m$  is obtained  $X_m \approx \sum_{r=1}^R \mathbf{s}_r \circ \mathbf{t}_r$ . The inner product of  $X_p$  and  $X_m$  is calculated as

$$\begin{aligned} \langle X_p, X_m \rangle &= \left\langle \sum_{r=1}^R \mathbf{u}_r \circ \mathbf{v}_r, \sum_{r=1}^R \mathbf{s}_r \circ \mathbf{t}_r \right\rangle \\ &= \sum_{l=1}^R \sum_{n=1}^R \langle \mathbf{u}_l, \mathbf{s}_n \rangle \langle \mathbf{v}_l, \mathbf{t}_n \rangle. \end{aligned} \quad (18)$$

Substituting (18) into (12), the sequential minimal optimization algorithm is used to find the optimal tradeoff parameter in the SHTM.

*Step 9.* Based on the inner product in (18), the rotor states classification result is obtained according to (15) and its classification accuracy is evaluated and compared.

## 6. Applications in the Rotor System Fault Identification

Figure 1 shows the experiment set-up used in this work. The test rig consists of motor, shown on the right of the photograph, driving a rigid cylindrical shaft supported by two cylindrical journal bearings, with a supporting journal bearing on the right end near the driving motor and an oil film journal bearing at the left end for simulating oil film instability faults. Two discs are mounted on the shaft, with one at the mid-plane between the two bearings and the other near the left oil film bearing. The shaft is not of uniform diameter throughout but has two portions with different diameters. One short portion of diameter 24 mm rotates in the left oil film journal bearing and has a length of 40 mm, just slightly longer than the length of the bearing. The remainder of the shaft has a diameter of 12 mm and a length of 480 mm and has its other end rotating in the right supporting bearing. Two proximity eddy current sensors are mounted, as shown in the figure, just to the right of the center disc, to measure the horizontal and vertical vibrations of the rotor at that position. In the experiment, a small mass is attached in the rotating disc to simulate an unbalance condition. Using the test bench described, the experiments under different rotational speeds with various artificially simulated faults are conducted to verify the practical validity of the proposed method. The data sampling frequency is 2048 Hz. The experiment details are listed in Table 1.

Considering the different rotor-bearing states, there are totally 8 running states. Moreover, the data corresponding to each rotor state is equally divided into two parts: one for reference data and the other for test data. Furthermore, for each rotor state, the reference and test data are again partitioned into some equal time-interval subsignals with the time duration 0.8 s. There are totally 400 vibration data for 8 bearing train states, about 50 vibration signals for each state.

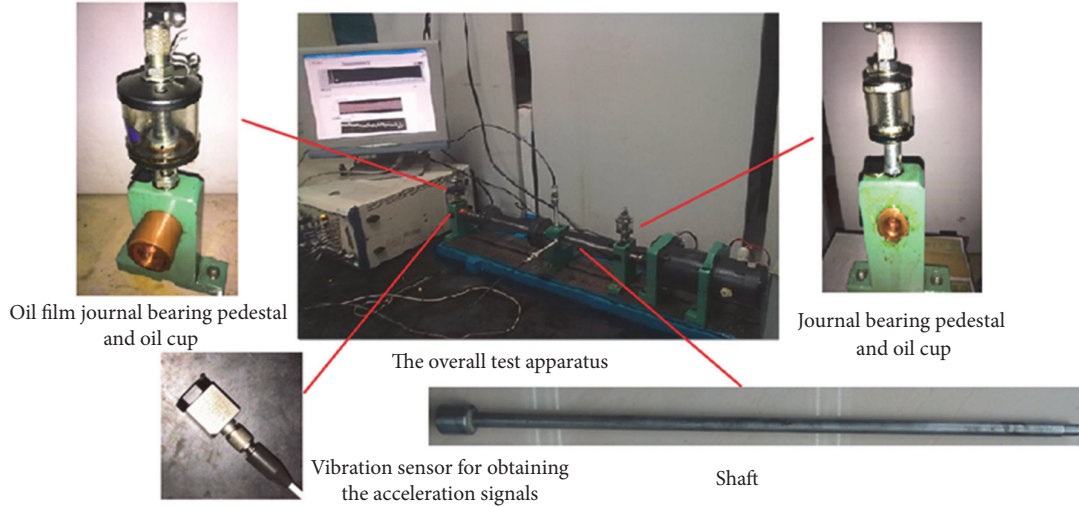


FIGURE 1: Test rig and its main components.

TABLE 1: System operation states at different operation speeds.

Experiment	1	2	3	4	5	6	7	8
Class code	(a)	(b)	(c)	(d)	(e)	(f)	(g)	(h)
Operating speed/rpm	2000	3000	5500	6200	2000	3000	5500	6200
Observed state of operation	Normal	Resonance at first critical frequency	Oil whirl	Oil whip	Unbalance	Resonance with unbalance mass	Oil whirl with unbalance mass	Oil whip with unbalance

After time-frequency analysis, about 50 TFIs for each state are obtained.

Firstly, AOK time-frequency transform is performed on every sample. Figure 2 depicts the AOK distributions of the rotor vibration signals in different states. The TFIs at 3000 rotating speed with and without unbalance mass are very similar, as shown in Figures 2(b) and 2(f) where the main frequency components are almost the same. The same case occurs in Figures 2(a), 2(e), 2(c), and 2(g). Therefore, it is not easy to identify the rotor states directly according to the TFIs. It is very important to perform a quantitative analysis for accurate TFI pattern classification.

Each TFI is partitioned into 5 regions ( $R_i(t, f)$ ,  $i = 1, 2, \dots, 5$ ) with equal frequency band 200 Hz. The GLCM is calculated for each region  $R_i$ . Based on  $R_i$  the corresponding texture feature vectors are obtained and noted as  $M_i = [m_1^{R_i}, m_2^{R_i}, \dots, m_6^{R_i}]$ , ( $i = 1, 2, \dots, 5$ ), where  $m_1^{R_i}, m_2^{R_i}, \dots, m_6^{R_i}$ , respectively, presents ASM, IDM, CON, COR, VAR, and ENT of TFI region  $R_i$  in the  $i$ th frequency band. To present the differences between the frequency components under each conditions,  $M_i$  is arranged in the sequence of frequency bands to construct the tensor  $M = [M_1, M_2, M_3, M_4, M_5]^T$ . To a fair comparison, the column vectors for each texture feature are normalized, respectively. In order to clearly display the difference of features in eight rotor states, the texture feature tensors are mapped into the color lattices. Figure 3 provides the feature tensors of four individual signals selected from each state sample set texture tensors. It is clear that the

feature tensors for the same type of rotor state are very similar, but for different fault types the obvious differences exist in the color lattices. Therefore, the feature tensors have good clustering and classifying, which can effectively represent rotor working conditions and be used to do fault states recognition.

The normalized feature tensors are put into the SHTM for classification. The classification results of the 8 rotor states are shown in Table 2. Table 2 illustrates that, when the feature tensors are used as input for the SHTM, 8 types of rotor state samples can be effectively distinguished. With the tensor features in the states “(b);” “(c);” “(g);” and “(h)” (noted as in Table 1) the SHTM exhibits the best results and the recognition rate reach 100%. The recognition rates of “(a),” “(b),” “(e),” and “(f)” state are 99.48%, 97.81, 99.73%, and 98.95%, respectively. The total recognition rate is 99.5%. The classification results indicate that the rotor condition can be effectively described using the texture tensors and accurately identified with the SHTM.

In order to investigate the robustness of the proposed method to the selection of TF transform, the classification accuracies based on short-time Fourier transform (STFT), S-transform (S-T), continuous wavelet transform (CWT), and AOK in the case of different segment number are compared in Figure 4. It is clear in Figure 4, whatever the segment number is, the recognition rates with different time-frequency distributions are very close with enough training samples. Comparatively speaking, AOK time-frequency transform has

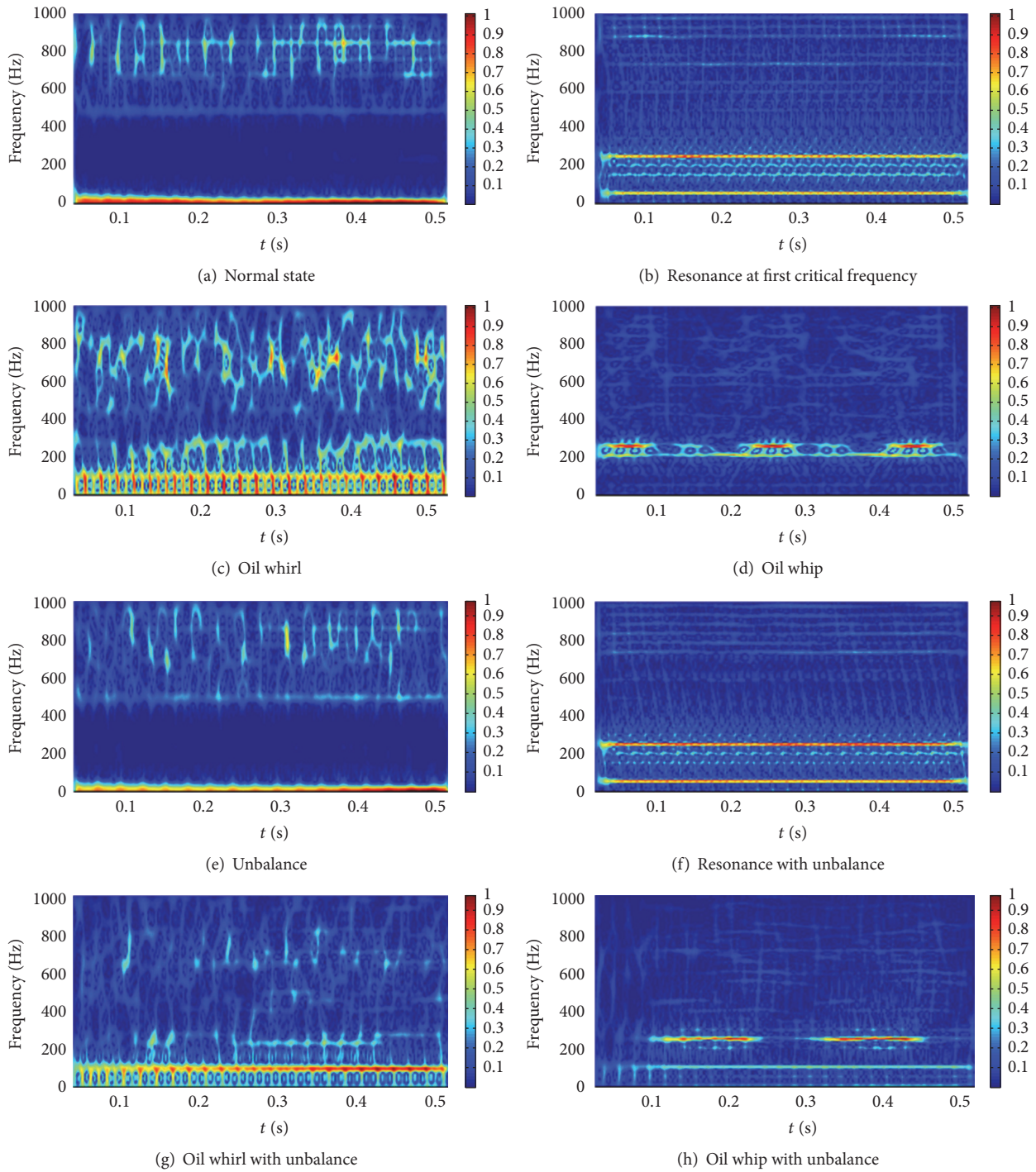


FIGURE 2: AOK time-frequency spectrogram for each sample vibration.

a good stability in the classification even with small sample data. That is, the proposed method has a good robustness to the selection of time-frequency distribution.

At the same time, in order to investigate the effect of segment number on the classification preciseness, the state recognition rates in the cases of different segmentations are compared with each other, as shown in Figure 5. According to Figure 5, with enough training samples, the recognition

rates are nearly approaches to the same value 100% in all the cases of segmentations. In the case of the big size sample, the proposed method is robust to the segment number of TFI. In the case of the small size sample below 60, the optimal segment number is 5, and the corresponding recognition rate reaches 99.96% with 30 training samples. In general, the segment number of TFI has a good robustness to the fault pattern recognition of rotor system.

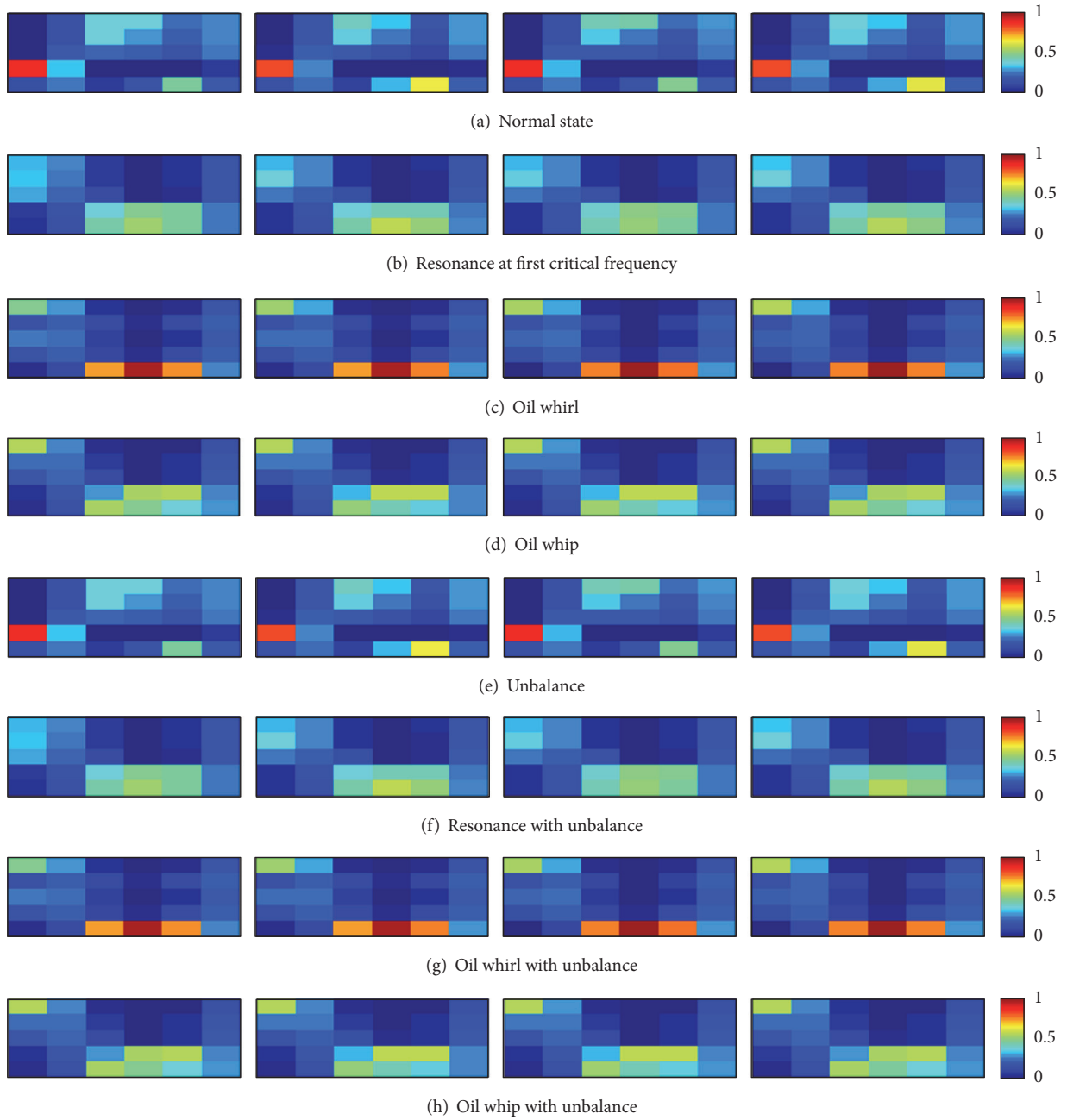


FIGURE 3: Texture feature tensors of TFI under 8 rotor states.

TABLE 2: Recognition results of rotor states.

State	Test sample number	Right recognized results	Wrong recognized results	Recognition rate
(a)	387	385	2	99.48%
(b)	382	374	8	97.91%
(c)	362	362	0	100%
(d)	375	375	0	100%
(e)	377	376	1	99.73%
(f)	381	377	4	98.95%
(g)	369	369	0	100%
(h)	367	367	0	100%
Total number	3000	2985	15	<b>99.50%</b>

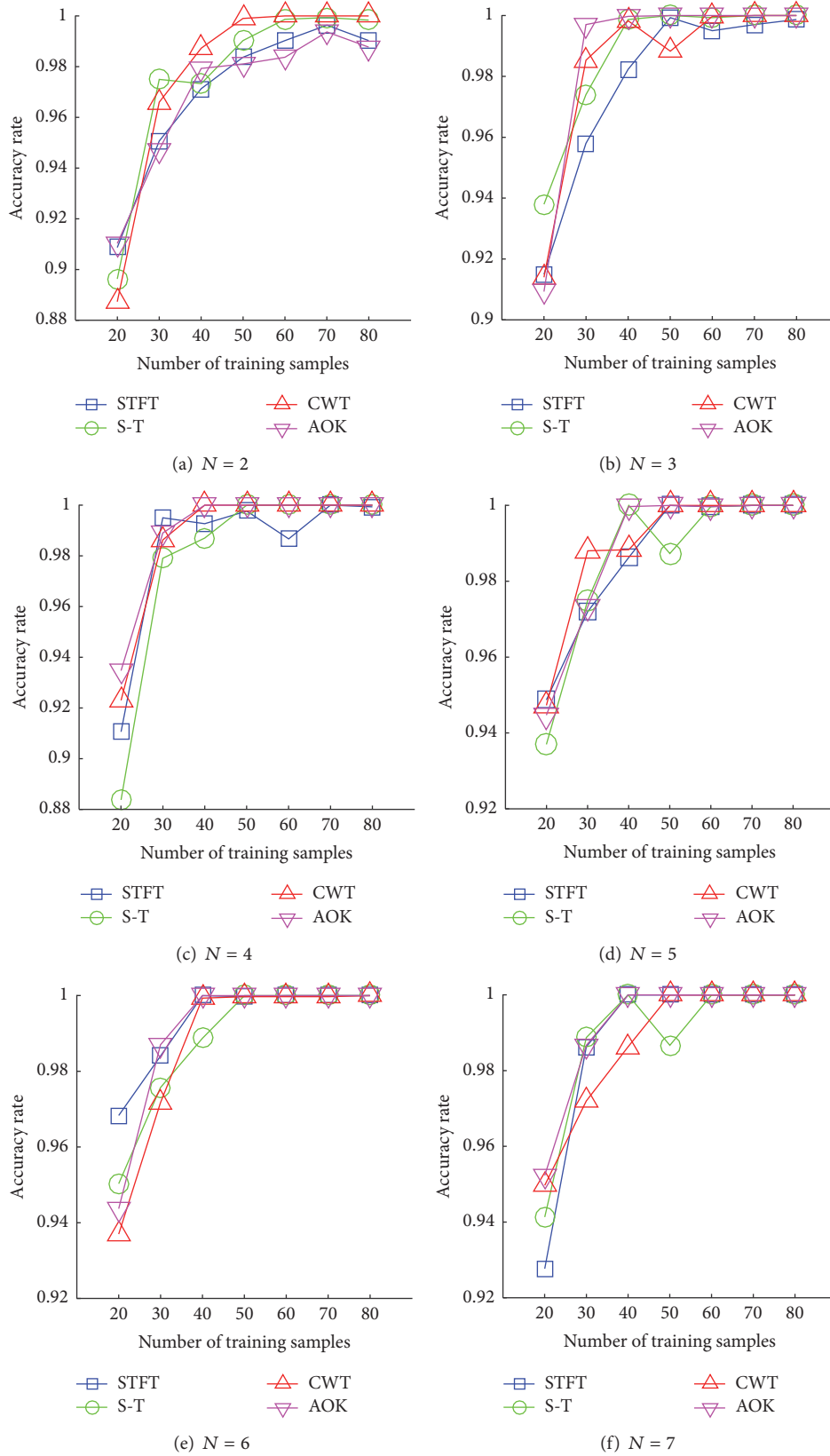


FIGURE 4: Recognition rate comparison between different time-frequency methods.

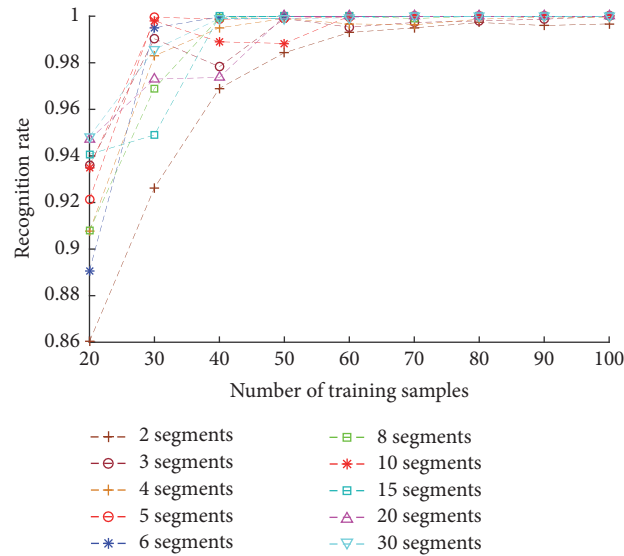


FIGURE 5: Comparison of recognition rates with different segment number.

To further evaluate the performance of proposed method, we also used the same training and test samples to carry out the SVM and BP neural network identification test in the case of different TF segmentation. For the classifiers SVM and BP under the multiple segments, the input feature vectors are constructed by stacking the texture features of each TFI subregion. The performances of each classifier are compared in Figure 6, where the number (1, 4, 5) denotes the number of segment and “Number & classifier” denotes the classifier in the case of the corresponding segment number. When the segment number is set as 1, the global texture features of TFI are extracted. From the Figure 6, the accuracy curve of “ $N = 5$  and STM” is completely above the other curves and very close to the curve of “ $N = 4$  and STM.” It is clear that the feature tensor-based SHTM performs better than the vectors-based BP or SVM. The curves of “ $N = 1$  and BP” and “1 and SVM” are totally below the other curves. It is verified that using the hierarchical texture tensor greatly enhances the classification accuracy compared to using the global features.

## 7. Conclusions

In this paper, a novel approach for rotor system fault pattern recognition is proposed based on the SHTM and the time-frequency hierarchical texture feature tensor. The contributions of this paper include the following:

- (1) In order to keep the correlation and interdependence between the TF characteristics in different frequency bands, hierarchical feature extraction is performed on the TFI fragment in different frequency bands. The features in each frequency band are extracted separately and treated differently. The hierarchical feature extraction can effectively decrease the negative interference effects from other harmonic components

or strong noises and make the fault characteristics be predominant.

- (2) To avoid the information loss and distortion in vectorizing the hierarchical texture features of TFI, the feature vectors from each TFI blocks are constructed into a feature tensor according the sequence of frequency band segmentation. The representation of feature tensor makes full use of abundant information on TFI and solves the “curse of dimensionality” problem in the stacking vector classification
- (3) The SHTM as a tensor classifier is introduced into the pattern recognition of bearing fault states, which can effectively exploit the characteristics of features among multiple modes and the redundancy from interband correlation. The experiment results showed that the tensor classifier performs greatly better than the conventional vector-based classifiers in the rotor fault pattern recognition, especially in the case of the small size sample.

In a word, for the state identification of rotor system the proposed method can obtain high fault pattern recognition rate, good robustness to the selection of time-frequency transform, and the number of TFI segments. This promising method will contribute to machine working conditions monitoring and fault diagnosis.

## Competing Interests

The authors declare that they have no competing interests.

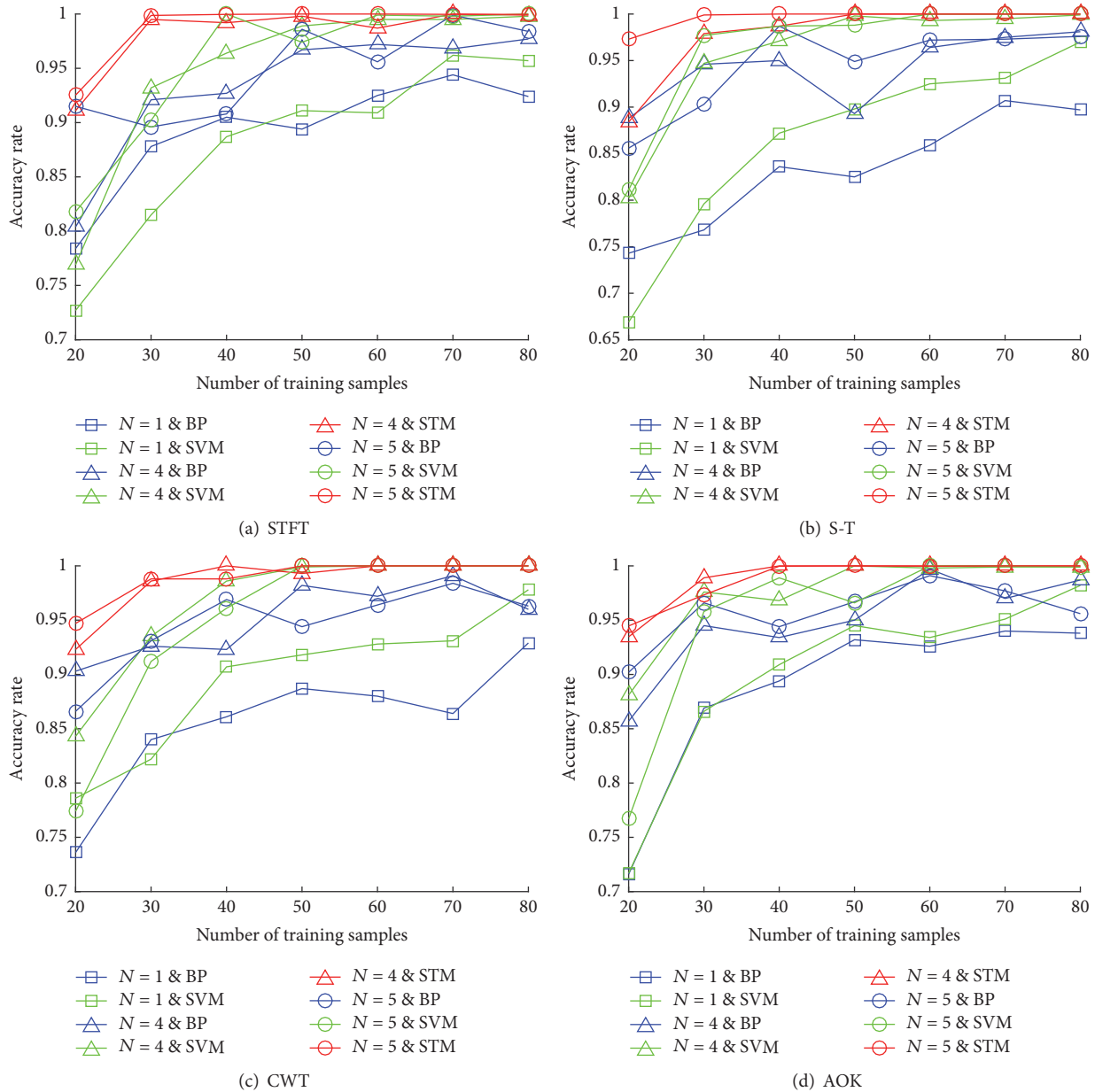


FIGURE 6: Comparison of recognition rate between hierarchical texture algorithms and traditional texture algorithms.

**Acknowledgments**

This work is supported by the National Natural Science Foundation Project (nos. 51475052 and 51675064), the Fundamental Research Funds for the Central Universities (no. 106112016CDJZR115502), and the China Postdoctoral Science Foundation (nos. 2016T90833 and 2015M582519).

**References**

[1] A. K. Jalan and A. R. Mohanty, “Model based fault diagnosis of a rotor-bearing system for misalignment and unbalance under steady-state condition,” *Journal of Sound and Vibration*, vol. 327, no. 3-5, pp. 604–622, 2009.

[2] X. Liu, L. Bo, and H. Luo, “Smoothing localized directional cyclic autocorrelation and application in oil-film instability analysis,” *Journal of Sound and Vibration*, vol. 368, pp. 191–201, 2016.

[3] X. Liu and L. Bo, “Identification of resonance states of rotor-bearing system using RQA and optimal binary tree SVM,” *Neurocomputing*, vol. 152, pp. 36–44, 2015.

[4] G. Badr and B. J. Oommen, “On optimizing syntactic pattern recognition using tries and AI-based heuristic-search strategies,” *IEEE Transactions on Systems, Man, and Cybernetics, Part B: Cybernetics*, vol. 36, no. 3, pp. 611–622, 2006.

[5] S. Omachi and M. Omachi, “Fast template matching with polynomials,” *IEEE Transactions on Image Processing*, vol. 16, no. 8, pp. 2139–2149, 2007.

- [6] M. Holden, "A review of geometric transformations for nonrigid body registration," *IEEE Transactions on Medical Imaging*, vol. 27, no. 1, pp. 111–128, 2008.
- [7] M.-K. Hu, "Visual pattern recognition by moment invariants," *IRE Transactions on Information Theory*, vol. 8, no. 2, pp. 179–187, 1962.
- [8] A. Baraldi and F. Parmiggiani, "Investigation of the textural characteristics associated with gray level cooccurrence matrix statistical parameters," *IEEE Transactions on Geoscience and Remote Sensing*, vol. 33, no. 2, pp. 293–304, 1995.
- [9] N. Sarkar and B. B. Chaudhuri, "An efficient differential box-counting approach to compute fractal dimension of image," *IEEE Transactions on Systems, Man and Cybernetics*, vol. 24, no. 1, pp. 115–120, 1994.
- [10] B. Li, P.-L. Zhang, D.-S. Liu, S.-S. Mi, G.-Q. Ren, and H. Tian, "Feature extraction for rolling element bearing fault diagnosis utilizing generalized S transform and two-dimensional non-negative matrix factorization," *Journal of Sound and Vibration*, vol. 330, no. 10, pp. 2388–2399, 2011.
- [11] B. Li, S.-S. Mi, P.-Y. Liu, and Z.-J. Wang, "Classification of time-frequency representations using improved morphological pattern spectrum for engine fault diagnosis," *Journal of Sound and Vibration*, vol. 332, no. 13, pp. 3329–3337, 2013.
- [12] C. Wang, Y. Zhang, and Z. Zhong, "Fault diagnosis for diesel valve trains based on time-frequency images," *Mechanical Systems and Signal Processing*, vol. 22, no. 8, pp. 1981–1993, 2008.
- [13] Q. Wang, Y. Zhang, Y. Zhu, and J. Yang, "Fault diagnosis of time-frequency images based on non-negative factorization and neural network ensemble," in *Proceedings of the International Joint Conference on Neural Networks (IJCNN '08)*, pp. 607–614, Hong Kong, China, June 2008.
- [14] T. Guo, L. Han, L. He, and X. Yang, "A GA-based feature selection and parameter optimization for linear support higher-order tensor machine," *Neurocomputing*, vol. 144, pp. 408–416, 2014.
- [15] Z. Hao, L. He, B. Chen, and X. Yang, "A linear support higher-order tensor machine for classification," *IEEE Transactions on Image Processing*, vol. 22, no. 7, pp. 2911–2920, 2013.
- [16] H. Tamura, S. Mori, and T. Yamawaki, "Textural features corresponding to visual perception," *IEEE Transactions on Systems, Man and Cybernetics*, vol. 8, no. 6, pp. 460–473, 1978.
- [17] H. Lategahn, S. Gross, T. Stehle, and T. Aach, "Texture classification by modeling joint distributions of local patterns with Gaussian mixtures," *IEEE Transactions on Image Processing*, vol. 19, no. 6, pp. 1548–1557, 2010.